Title

Recoil Range Studies of Heavy Products of Multinucleon Transfer from 18O to 245Cm and 249Cf

Author

McFarland, Rose Marie

Publication Date

1982-09-01

LBL-15027

Lawrence Berkeley Laboratory
UNIVERSITY OF CALIFORNIA

RECOIL RANGE STUDIES OF HEAVY PRODUCTS OF MULTINUCLEON TRANSFER FROM ^{18}O TO ^{245}Cm AND ^{249}Cf

Rose Marie McFarland
(Ph. D. thesis)

September 1982

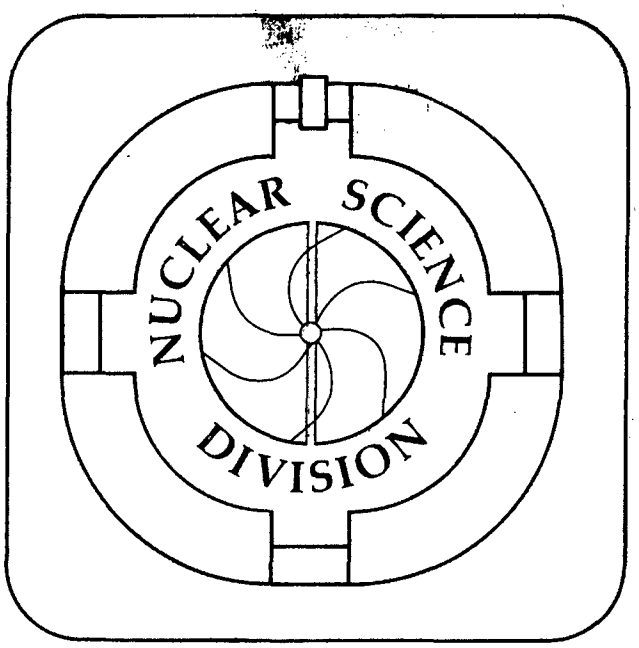

Prepared for the U.S. Department of Energy under Contract DE-AC03-76SF00098

LBL-15027

DISCLAIMER

LBL-15027

Recoil Range Studies of Heavy Products of Multinucleon Transfer from ^{18}O to ^{245}Cm and ^{249}Cf

Rose Marie McFarland

Ph. D. Thesis

September 1982

Nuclear Sciences Division
Lawrence Berkeley Laboratory
University of California
Berkeley, CA 94720

This work was supported by the Director, Office of Energy Research, Division of Nuclear Physics of the Office of High Energy and Nuclear Physics of the U. S. Department of Energy under Contract DE-AC03-76SF00098.

Recoil Range Studies of Heavy Products of Multinucleon Transfer from ^{18}O to ^{245}Cm and ^{249}Cf

by

Rose Marie McFarland

ABSTRACT

Recoil range distributions were measured for alpha and spontaneous fission activities made in the bombardment of ^{245}Cm and ^{249}Cf with ^{18}O from 6.20 MeV/nucleon down to the interaction barrier. The shape of the distributions indicates that transfers of up to four protons take place via a combination of quasi-elastic (QET) and deep inelastic (DIT) mechanisms, rather than complete fusion-de-excitation (CF) or massive transfer (MT). Angular distributions constructed from recoil range distributions, assuming QET/DIT, indicate that the QET component contributes more significantly to the heavy product residue cross section than the DIT, even though primary cross sections are expected to be higher for DIT than for QET. This may be explained qualitatively as a result of the high excitation energies associated with DIT; the very negative Q_{gg} of projectile stripping for these systems combined with the lower expected optimal Q_{rxn} of QET compared to DIT can give QET products comparatively low excitation.

DEDICATION

This work is dedicated with gratitude to my husband Jimmie Lee McFarland for his presence and support. What with pumping gas, washing cars, frying hamburgers, cleaning house, cooking, even adding up numbers for me, and providing so much psychological support, especially via foot rubs, he worked harder for this than I did. His presence made owl shifts nearly impossible to endure, but a lot more fun to come home from.

ACKNOWLEDGEMENTS

I would like to thank:

Dr. Glenn T. Seaborg and Dr. Albert Ghiorso for their help, guidance, and support,

The SHEIKs group,

Dr. Kim Williams, Dr. Patricia Baisden, Dr. Isadore Perlman, Dr. Frank Asaro, Dr. Darleane Hoffman, Diana Lee, and Dr. Hans R. von Gunten for helping me learn the art of chemical separation,

The scientists and staff of the Nuclear Science Division for providing such a stimulating environment in which to work, and especially for allowing me to give all those grad student seminars,

The environmental health and safety crew, especially Harry Harrington and "Cal" Calhoun, for preventing me from catching fire, becoming radioactive, tripping over lead bricks, or otherwise hurting myself,

Dr. Ralph C. Applebee, who introduced me to logical reasoning and Dr. William A. Adams, who insisted upon equal time for intuition,

Charles Henry, my first chemistry teacher and the best basketball coach in the SIC,

Martin Schulman, Dana Dunlavey, and Gary Shen, who gave me their valuable assistance,

Henry Weinhard of Oregon and Yukon Jack of Canada,

The citizens of Stanley, Idaho for their support and friendship.

TABLE OF CONTENTS

I. PURPOSE AND INTRODUCTION

The purpose of this study is to investigate multinucleon transfer from ^{18}O projectiles to ^{245}Cm and ^{249}Cf targets by measuring the recoil range distributions of target-like products. Four bombardments were done with ^{249}Cf, at 83., 89.2, 99.8, and 111.6 MeV, and are labelled OCf-I, -II, -III, and -IV, respectively. Three ^{245}Cm bombardments were done, at 93., 99.6, and 111.6 MeV, labelled OCm-I, -II, and -III, respectively. This work is intended to supplement the excitation functions measured for heavy ion reactions with actinides, particularly for light heavy ion ($4 < A \leq 40$) projectiles[1,2,3], abbreviated LHI. While excitation functions provide some information on the likelihood of producing certain nuclides and on mechanisms, the recoil range distribution provides more direct information on the exit channel separation energies and angles.

The actinide region is of particular interest to our group. These nuclides represent the known extremes of Z and A in nuclear matter, and accordingly have special properties. Fission barriers are roughly equal to nucleon binding energies, and can be "double-humped", which allows nuclei with a higher second hump to have fission isomers. The height and shape of both humps must be considered, which complicates statistical calculations of de-excitation of an actinide formed in a nuclear reaction. In heavy ion reactions the Coulomb barriers are high. and correspondingly high bombardment energies must be used. Actinide targets must be

used for superheavy element searches and also for studies of other actinides requiring the addition or subtraction of a few nucleons. However, although this is an "island" of relative stability, there are relatively few actinides stable enough and available in sufficient quantities to be used as target material. This sets practical limitations on the ways in which a given actinide may be formed, and conversely, on the number of nuclear species which can be made via a given specific reaction.

The many kinds of reaction that can occur between two colliding nuclei are sorted into mechanisms which are classified according to incoming angular momentum into complete fusion, various nucleon transfer processes, and elastic scattering (for example, see Figure 1). Complete fusion (CF) is the amalgamation of the two nuclei into one. Three transfer mechanisms will be discussed here, quasi-elastic tramsfer (QET), deep-inelastic transfer (DIT), and massive transfer (MT). QET is the most peripheral, involving minimal nuclear interaction. DIT occurs with more intimate internuclear contact, and is sometimes grouped with CF in what are called "close" collisons. Deep inelastic collisions involve significant overlap of nuclear surfaces and dissipation of entrance channel kinetic energy. MT is proposed to occur via the breakup of the projectile followed by the fusion of one of the pieces with the target. The Background section below contains a more detailed description of various transfer experiments and models.

Complete fusion, where it can be attained, has many advantages over transfer in LHI + heavy target reactions. A large fraction of

the total reaction cross section goes to fusion[4,5] for energies such that the closest distance of approach is greater than the internuclear half-density distance. Bass[5,6] calls this energy E_1 and with his fusion model E_1 is calculated to be 158 MeV in the center of mass frame for $^{18}O + ^{249}Cf$. Fusion results in the addition of several protons to the target at good primary yields, that is, before losses through fission during the de-excitation of the compound nucleus. Because of the peripheral nature of transfer, for a given mass transfer to the target more orbital angular momentum is imparted to the heavy product than would be imparted by complete fusion of a projectile of the same mass. Increasing angular momentum increases the fission width exponentially (see Eqn. 24).

One disadvantage of complete fusion is the high excitation energy the products must have. The Coulomb barrier must be overcome; for some heavier ions extra kinetic energy[7-10] must be supplied over the Coulomb barrier to attain fusion. Conservation of energy and momentum requires that, upon fusion, all the relative kinetic energy, less $-Q_{gg}$ for the reaction, be converted to internal and collective excitation of the compound nucleus. Another disadvantage in complete fusion is that the N/Z of the compound nucleus, even before it loses neutrons in de-excitation, will be further toward the neutron-deficient side of beta stability than the target or projectile.

Early heavy ion reactions using actinide targets had the aim of producing a compound nucleus. Elements 102-107 were first made via

complete fusion of an LHI with an actinide nucleus[11-16]. Bombardments in our laboratory to search for superheavy elements, including the interlaboratory effort now in progress[17], have been planned with complete fusion as the mechanism. Such experimental objectives have been complemented by theoretical investigations of formation[7,18] and survival[19] of compound nuclei under these extreme conditions.

While for bombardments of heavy targets with ions lighter than argon at energies not too high above the interaction barrier CF accounts for most of the reaction cross section[4], it was found that for heavier ions[20] σ_{fu}/σ_R drops. Mass distributions have been measured for the products of bombardments of thick ^{238}U targets with ^{40}Ar at 7.20 MeV/nucleon[21], ^{56}Fe at 9.61 MeV/nucleon[22], ^{84}Kr at 7.20 MeV/nucleon[23], and ^{136}Xe at 8.46 MeV/nucleon[24]. These distributions were resolved according to mechanism and showed σ_{fu}/σ_R = .6, .14, .04, and < .02, respectively. The ratio also decreases for a given system as the bombardment energy increases[25], and, for a given compound nucleus, as the projectile-target asymmetry decreases[26]. For example, ^{84}Kr+ ^{209}Bi would lead to essentially the same compound nucleus as ^{56}Fe + ^{238}U, but no fusion-fission products were detected in the former bombardment at 6.25 MeV/nucleon to a limit of $\sigma_{fu}/\sigma_R \leq .03$[27]. In a bombardment of a thick ^{197}Au target with 8.38 MeV/nucleon ^{84}Kr, σ_{fu} was found to be effectively zero[28]. A rough guide is, if the system Z_pZ_T exceeds 2000, where Z_p and Z_T are the atomic number of the projectile and target, σ_{fu} will

be low or negligible[29]. Swiatecki[7,18] has investigated theoretically the dynamics of heavy ion collisions and limits to fusion in these heaviest regions. The "missing" cross section for such heavy ions, that of the close collisions that do not lead to fusion, goes to deep inelastic transfer[4,22-24,27].

Williams[30] discovered that compound nucleus evaporation residue cross sections from the bombardment of ^{232}Th with ^{14}N, ^{235}U with ^{11}B and ^{15}N, and ^{238}U with ^{10}B were anomalously low. In this case, the missing cross section was found to be going to formation of products of $Z = Z_P + Z_T - 1$ or $Z_P + Z_T - 2$. Earlier, Hahn, et. al.[31] reported the measurement of Cf isotope excitation functions, recoil range distributions, and angular distributions from transfer and from fusion in the reactions $^{238}(^{12}C,xn)^{245,246}Cf$ and $^{239}Pu(^{12}C,\alpha xn)^{245,246}Cf$. These results generated interest in our group in the systematics of actinide production from LHI transfer reactions for comparison with the heavy ion data and to explore the LHI results of Williams and Hahn.

Very heavy ions, up to ^{238}U, are now available at energies above the interaction barrier for all available targets, the heaviest of which is ^{254}Es. The systematics of actinide production via transfer for projectiles which do not form compound nuclei have been studied with ^{40}Ar, ^{84}Kr, ^{136}Xe[32], and ^{238}U[33] ions on thick ^{238}U targets. Excitation functions for the production of actinides from heavy ions of A > 40 on thin actinide targets have been reported, for example, ^{238}U on ^{248}Cm

at bombardment energy between 1.18 and .96 times the interaction barrier[34], and ^{86}Kr and ^{136}Xe on ^{248}Cm at several energies near and below the spherical Coulomb barrier[35]. Further impetus for studies of LHI + actinides was provided by the production of a fission activity that resembled ^{259}Fm in the bombardment of ^{248}Cm with ^{18}O[1]. This would require the net transfer of four protons and seven neutrons, which would be a very neutron-rich net transfer of eleven nucleons, without significant excitation of the heavy fragment. Fermium-259 is to the right of the beta-stability line so the neutron-binding energy B_n would be low. The mass table of Moller and Nix[36] predicts B_n for ^{259}Fm to be 5.09 MeV.

Virtually all the excitation energy produced in a LHI + actinide projectile stripping reaction may be assumed to go to the heavy fragment because of its much higher level density. More than a few MeV of internal excitation energy generated in the production of a ^{259}Fm primary fragment would lead to the evaporation of a neutron or fission, either of which would destroy ^{259}Fm. A search for another "^{11}Be" transfer from ^{18}O, using a thick ^{232}Th target, failed to detect any of the analogous product, ^{243}Pu, to a limit of 15 ± 7 nanobarns[37]. Excitation functions for the production of actinides from ^{16}O, ^{18}O, and ^{22}Ne on ^{248}Cm[2] and from ^{18}O, ^{22}Ne, and ^{136}Xe on ^{254}Es[38] have been measured with the intent of exploring the systematics of producing neutron-rich actinides and transactinides and the likelihood of neutron-rich transfers such as $^{18}O + ^{248}Cm = ^{259}Fm$. These data can be used to guide the planning of future bombardments.

Also, until particle detectors can be made with sufficient resolution to identify the Z of fission fragments, the assignment of spontaneous fission activities inaccessible from compound nuclei must be done with the aid of these systematics. These neutron-rich nuclei are of interest particularly in testing theories of nuclear structure and spontaneous fission[38].

In QET, an appreciable fraction of the initial kinetic energy is left in the exit channel. Even in the most inelastic of DIT collisions, kinetic energy equal to the exit Coulomb separation energy is removed from the system. Also, final energies have broad distributions for given nuclides, so that it is possible in an individual reaction to have a rather large transfer associated with a rather low excitation energy, and neutron- or proton-rich transfers are possible. This feature of transfer has been exploited by Artukh, et. al.[39], who used it in planning the experiments which led to the discovery of the neutron-rich isotopes ^{22}O, ^{20}N, and ^{18}C from $^{18}O + ^{232}Th$. The heavy product of <u>massive</u> transfer, however, would be predicted to be have E* very close to that for complete fusion of the equivalent projectile and high orbital angular momentum as well. Therefore, in terms of evaporation residue production cross section, CF might be preferred over MT for a given product.

Present knowledge of multinucleon transfer between light heavy ions and targets of $A \geq 140$ has been used extensively in the interpretation of these range distribution and cross section data. This knowledge is summarized in the following section.

II. BACKGROUND

A. CLASSICAL KINEMATICS

For a collision between projectile P and target T with relative initial kinetic energy E:

$$E - V(r) = \hbar^2 l(l+1)/2J \qquad (1)$$

r = center-to-center separation distance between P and T

$V(r)$ = Coulomb + nuclear radial potential energy

$l\hbar$ = relative orbital angular momentum

J = moment of inertia of the center of mass. For two rigid spheres of mass A_p and A_T, $J = A_{12}r^2$, where $A_{12} = A_pA_T/(A_p+A_T)$ is the reduced mass

Convenient units are: E and V in MeV, r in fm, A in amu, and $\hbar = h/2\pi = 6.46557$ (MeV amu $fm^2)^{1/2}$

If the ratio of the wavelength of relative motion of colliding nuclei to the relevant system dimension is small, the reaction trajectory may be described by classical mechanics. One measure of this ratio is the Sommerfeld parameter, η, half the ratio of the distance of closest approach, D, for two point charges of Z_p and Z_T in a head-on collision to the wavelength of relative motion:

$$\eta = Z_P Z_T e^2/\hbar v \qquad (2)$$

e = the charge of an electron

v = the relative velocity

$\eta \gg 1$ corresponds to classical motion.

All the reactions considered in this work have η well over 1, as shown in Table 1.

At distances such that each nucleus is outside the finite range of the nuclear force of the other, only Coulomb interactions are possible. Coulomb excitation of the nucleus may occur; otherwise the nuclei scatter elastically along a Rutherford trajectory. The Coulomb barrier E_C is defined as the initial relative kinetic energy necessary to induce nuclear reaction and R_C as the distance between point charges Z_P and Z_T at which the Coulomb potential equals E_C:

$$R_C = Z_P Z_T e^2/E_C \qquad (3)$$

The interaction distance R_{int} is defined as the actual distance of closest approach for a head-on collision between P and T at initial energy E_C. At large impact parameters, for Rutherford scattering, the distance of closest approach D will exceed R_C. At smaller impact parameters nuclear attraction will deflect the trajectory so that $D < R_C$. A grazing collision may be considered

Table I. Classical kinematic quantites

EXPT	ϵ	η	θ_{gr}(deg) (heavy frag)	$l_{gr}(\hbar)$	R_{int} (fm)	θ_{gr} (corr) (b)	l_{gr} (corr) (b)
OCf-IV	6.20	50.	80.	41	12.46	107.	67
OCf-III	5.54	52.	39.	18		89.	50
OCf-II	4.96	56.	0.	(a)		59.	31
OCf-I	4.61	58.	0.	(a)		0.	(c)
OCm-III	6.20	49.	83.	43	12.44	117.5	80
OCm-II	5.53	51.	46.	21		103.	64
OCm-I	5.17	53.	0.	(a)		92.	54

a) Initial kinetic energy below calculated spherical Coulomb barrier.

b) Use Coulomb barrier = .86 (calculated) for OCf, or
= .80 (calculated) for OCm experiments.

c) Initial kinetic energy below corrected Coulomb barrier.

to be the trajectory for which $D = R_C$.

Properties of the classical grazing trajectory are of particular interest in the study of transfer reactions. The grazing angle, θ_{gr}, is calculated as the Coulomb scattering angle:

$$\sin(\theta_{gr}/2) = \epsilon_C/(2\epsilon - \epsilon_C) \tag{4}$$

$\epsilon_C = E_C/A_{12}$

$\epsilon = E/A_{12}$

The classical grazing angular momentum l_{gr} is:

$$l_{gr}^2 = 2\eta\epsilon/\epsilon_C \tag{5}$$

Also of interest is R_i, the nuclear radius, measured from the center to the point at which the nuclear matter density is half that at the center. $R_{12} = R_1 + R_2$ is the internuclear half-density distance. Based upon fitting electron scattering data, Bass[5] uses the formulae:

$$R_{12} = R_P + R_T \tag{6}$$

$$R_i = 1.12A_i^{1/3} - .94A_i^{-1/3}$$

$$R_C \approx R_{int} = R_P + R_T + 3 \text{ fm} \tag{7}$$

For trajectories such that the approach distance D is just below R_{int}, the internuclear potential is still dominated by Coulomb repulsion, but the nuclear force is significant and, by definition of R_{int}, nuclear reactions may occur. Nucleons may be transferred from one nucleus to the other as their surfaces graze one another. At higher bombardment energies and/or lower impact parameters, D approaches R_{12}. If entrance channel conditions for complete fusion are met and the resulting compound nucleus is stable, it will form. Otherwise the nuclei will come in close contact, collide inelastically as relative motion is stopped at R_{12}, exchange nucleons, and reseparate.

Studies of fusion excitation functions led to the concept of a critical entrance channel angular momentum, l_{fu}, above which fusion could not occur[6,40-44]. The more fundamental dimension was shown to be r_{fu}, the critical distance of approach[45]:

$$E - V(r_{fu}) = \hbar^2 l_{fu}(l_{fu} + 1)/2A_{12}r_{fu} \qquad (8)$$

$$r \geq R_{12}$$

One assumes a formula for V(r)[46,47] to find r_{fu} ($\geq R_{12}$), which is that value of r which minimizes the quantity $r^2[E - V(r)]$, and uses Eqn. (6) to deduce l_{fu}. Ref. 45 gives r_{fu} as $r_o(A_1^{1/3} + A_2^{1/3})$, where r_o = 1.0 or 1.4 fm.

The region of r-space that this work is concerned with is that between r_{fu} and R_{int}. In this space, nuclear reaction may occur, but complete fusion may not.

B. OVERVIEW OF TRANSFER MECHANISMS

Multinucleon transfer was first observed[48-52] in the mid- and late 1950's. Transfers of one or two nucleons or a cluster such as an alpha particle were well described by a model assuming the transferred entity tunnels through the interaction barrier as the colliding nuclei approach on a Rutherford trajectory[53,54]. Several suggestions[55-57] were made as to what the mechanism for more complex transfers might be. In 1959, they were proposed[50] to occur via a grazing collision. This suggestion was subsequently given support by measurements[58] of angular distributions and excitation functions of recoiling projectile-like fragments from ^{16}O projectiles on Al, Cu, and Sn targets. During the next decade, the analysis of transfer was based upon the classical kinematical requirements of grazing collisions. As heavier ions became available at higher energies and on-line detection devices became more sophisticated, it became clear that there were two distinct transfer mechanisms, which have come to be called quasi-elastic transfer and deep-inelastic transfer. Recently a third mechanism called massive transfer has been described, and it is reviewed in Ref. 59.

Quasi-elastic transfer (QET) and deep-inelastic transfer (DIT) are distinguished experimentally on the basis of the angle and energy of separation of the product fragments. QET, the old tunneling process, is associated with fast peripheral collisions where trajectories are governed chiefly by the Coulomb field. The

angular distribution is peaked at or near θ_{gr}. Transfer of a nucleon or cluster is accomplished in one step. Entrance and exit channel trajectory matching conditions dictate the optimal energy of separation of products E^f_{opt}, which, by conservation of energy, determines the excitation energy of the products (e. g. see Eqn. 18 below).

DIT is associated with closer approach distances, near R_{12}, multistep transfer processes, and longer-lived intermediate dinuclear complexes. The larger the number of steps involved in the transfer, the more statistical the transaction is, and the longer lived and more intimate the dinuclear complex must be. From the perspective of the approach distance, as r nears R_{12} the nuclear repulsion stops the relative radial motion and radial kinetic energy is dissipated into internal and collective modes. While the nuclei are thus joined nucleons are exchanged. The exit channel Coulomb and centrifugal forces overcome the nuclear attractive forces, for $r > r_{fu}$, and the products separate. The separation energy is found to fall between the Coulomb barrier of two touching spheres and that of two touching spheroids at equilibrium deformation[60]. Forward-peaked products, which result from faster reactions, separate at the touching-spheres energy, while products emitted at a large angle, from longer-lived complexes, separate at the energy of touching spheroids.

DIT has been sorted into two classes[61,62]. Class I is associated with dinuclear complexes with lifetimes of an appreciable fraction of a rotational period, with angular distributions which

peak near 0° relative to the beam axis and decrease exponentially with increasing angle, with separation energies near the exit channel Coulomb barrier, and with product (Z,A) distributions spread broadly around (Z_p,A_p) and (Z_T,A_T). Class I systems are fusile, that is, a large fraction of the total cross section is taken up by complete fusion.

Class II reactions are associated with interaction times short compared to the rotational period; angular distributions are peaked at a side angle and decrease at larger and smaller angles and mass and charge distributions of the projectile- and target-like products are narrow. Class II systems' cross sections for close collisions are dominated by DIT, with little or no compound nucleus formation. The LHI + heavy target systems at bombardment energies not too much above E_C appear to be well described by Class I DIT assumptions and QET. Both QET and DIT may contribute to a given net transfer. However, as the number of transferred nucleons increases, so does the relative contribution of DIT.

At higher energies massive transfer may be observed. It is recognized experimentally by particles of Z = 1 or 2 moving at or above the beam velocity at forward angles in coincidence with a heavy product which is the target plus the remainder of the projectile minus some neutrons. In 1961, Britt and Quinton[63] reported that high-energy α particles are emitted in the forward direction in reactions of light heavy ions on various targets. Galin, et. al.[64] observed fast α particles from ^{14}N + ^{103}Rh. Inamura, et. al.[65] observed fast α particles in coincidence with

gamma rays from isotopes of Yb in the reaction of 6.78 MeV/nucleon $^{14}N + ^{159}Tb$. Zolnowski, et. al.[66] observed similar transfers associated with fast α particles for a series of LHI on rare earth targets. The concept of "massive transfer" has been introduced to describe such reactions in which a light heavy ion projectile loses a large fraction of its mass to a heavy target, and the remaining light fragment is left with the beam velocity. The kinematics are reminiscent of complete fusion; this process has also been called "incomplete fusion". A model distinct from QET and DIT has been formulated to describe MT. It is called "breakup-fusion"[67] and is a refinement of the old "buckshot" hypothesis once proposed[55,56] for multinucleon transfer. The reaction begins with the elastic breakup of the projectile in the field of the target. One of the projectile-like fragments has a chance to subsequently fuse with the target. The remaining fragment proceeds at its original velocity. This mechanism is thought to be restricted to peripheral collisions.[68,69]. Sugihara[59] has written a summary of experiments and theories treating massive transfer. It has been argued[70] that there is no experimental evidence that the "massive transfer" reactions, presumed to occur via a two-step three-body process, are qualitatively different from DIT.

C. EXPERIMENTAL OVERVIEW OF TRANSFER

Analysis of the results of this study requires background knowledge of the energies and angles of separation associated with transfer from LHI to a heavy target. The projected recoil range does not uniquely determine either value. In 1970, Galin, et. al.[71] measured energy and angular distributions of projectile-like multinucleon transfer products of ^{12}C (ε = 7.17 MeV/nucleon) and ^{14}N (ε = 5.57, 8.07 MeV/nucleon) projectiles on Ag targets. Their results showed unambiguously that two mechanisms were contributing, one with low Q_{rxn} and angular distribution peaked at or just below the classical θ_{gr} which was more prominent for few-nucleon transfer, and the other with high Q_{rxn} and an angular distribution peaked near 0° which dominated greater-mass transfers.

In Ref. 72, Artyukh, et. al. reported measurements of the energy spectra and angular distributions of light fragments from 7.91 MeV/nucleon ^{22}Ne + ^{232}Th. This system is close to the systems of this study in projectile and target mass and bombardment energy per nucleon. In stripping reactions the angular distributions display the two components, one peaking at θ_{p-like}=0° and exponentially decreasing and the other a broad distribution centered at a side-angle. A measurement of separation energy, E^f_{sepn}, versus angle for stripping reactions showed that near the side-angle the E^f_{sepn} corresponds to a Q_{rxn} of roughly .9 of the optimum Q-value. Away from the centroid angle, E^f_{sepn} declines gradually, until it reaches the exit channel

Coulomb barrier. This correlaton of separation energy with angle confirms that for this system the DIT and QET are both contributing to these stripping reactions and supports the use of this mechanism to describe transfer from ^{18}O to ^{245}Cm and ^{249}Cf.

The system ^{40}Ar + ^{232}Th has been explored in detail in two complementary studies. Artukh, et. al.[73] measured the cross sections, energy spectra, and angular distributions of projectile-like products from boron to calcium for 7.43 and 9.70 MeV/nucleon ^{40}Ar. For Mg, Al, Si, and P isotopes produced at the lower energy and detected at angles between 20° and 50° in the lab frame the energy spectra were bell-shaped and centered just below the Coulomb barrier for touching spheres. For S and Cl, and for Ca and K, the energy spectra show a high-energy asymmetry which is maximal at θ_{lab} = 50-55°. Similarly, for the 9.70 MeV/nucleon bombardment, fragments more than four Z removed from the projectile show the bell-shaped angle-invariant energy spectra. As the fragment Z approaches that of the projectile the spectra develop high energy components which are most significant at θ_{lab} around 30-35°. The angular distributions clearly show two components, as indicated by the energy spectra, one an exponentially decreasing function peaked at $\theta < 20°$ and corresponding to the fully damped DIT energy spectra, and the other a roughly bell-shaped distribution centered at a side-angle, near 50° for the 7.43 MeV/nucleon bombardment and near 30° for the 9.70 MeV/nucleon bombardment. These peaks are near the Rutherford grazing angle and this component corresponds to the high-energy part of the asymmetric energy spectra

and the QET part of the reaction.

Jacmart, et. al.[74] bombarded ^{232}Th with 7.38 MeV/nucleon ^{40}Ar ions and compared the isotope and kinetic energy distributions at 18° and 40° in the lab frame, on the assumption that DIT predominates at the former angle and QET at the latter. The most probable final kinetic energy at 18° increased stepwise, each step representing an element, with increasing A. At 40°, the total kinetic energy decreased with A on either side of the maximum at ^{40}Ar, but more sharply with decreasing A, with little or no Z-dependence. The envelope of the isotope distributions at 18° for elements from Mg to Sc is fairly flat; at 40° the cross section drops sharply with increasing number of transferred charges. These results support the idea that for ^{40}Ar + ^{232}Th both QET and DIT contribute to multinucleon transfer and confirm both that QET is strongest near the grazing angle for the fewest transferred charges and that DIT predominates at the most forward angles and at all angles for the more massive transfers.

Many other studies have been done with multinucleon transfer from boron, carbon, nitrogen, oxygen, fluorine, and neon ions[75-79]. In each case, the angular distributions and exit channel kinetic energies and the dependence of each upon the number of transferred nucleons can be explained in terms of QET and DIT competition.

All these are empirically Class I systems. Inspection of the absolute and relative mass and charge of the projectile and target and of the bombardment energies would lead one to expect Class I

behavior from ^{18}O + ^{245}Cm and ^{249}Cf for transfers of $\Delta Z \leq 4$, that is, a DIT component with E^f_{sepn} equal to the spherical exit Coulomb barrier and θ_{max} near 0° and a QET component with E^f_{sepn} equal to E^f_{opt} and θ_{max} near the classical grazing angle. A semiquantitative criterion has been provided by Galin, et. al.[62]: the "Sommerfeld-like" parameter, η':

$$\eta' = Z_p Z_T e^2/\hbar v_B \approx l_{gr}/(2(E/B_{int} - 1)) \quad (9)$$

v_B = the velocity at the distance of closest approach

B_{int} = the interaction barrier

Class I characteristics are expected for $\eta' < 200$ and Class II properties for $\eta' > 250$. For all the bombardments of this study η' is well under 200.

Deep inelastic transfer products for Class I systems have been observed which have a significant 1/sinθ component to the angular distribution, consistent with an interaction time comparable to the rotational period of the dinuclear complex (e. g. see Ref. 60). These are most prominent for very large $\Delta Z, \Delta A$ and for heavier ions, e. g. ^{40}Ar. This component is neglected in this analysis.

Finally, expectations for primary cross sections for transfer have been treated to some extent in the literature. Any analysis of cross section must incorporate the chance that a precursor is formed and the probability that it decays in the course of de-excitation to

the nuclide of interest.

De-excitation of actinides is complicated by low fission barriers, comparable in magnitude to nucleon binding energies, and which decrease with increasing rotation. In experiments that measure only the actinide residue, primary cross sections as well as widths for subsequent particle evaporation, photon emission, and fission must be estimated with model predictions. Primary yield predictions will be discussed first, followed by an outline of theory of de-excitation of actinide fragments.

In Ref. 80, Artukh, et. al. present cross sections of light products, measured at 40° (lab), from bombardments of ^{197}Au and ^{232}Th targets with 8.56 MeV/nucleon ^{16}O ions. Several isotopes of elements of Z from 4 to 10 were resolved. The logarithm of the cross section of products of projectile stripping DIT reactions was found to be linearly dependent upon the reaction Q_{gg}. The slopes are the same for the same light product for ^{197}Au and ^{232}Th target. This relation and the combination of the direct and statistical empirical properties of the process was explained by Bondorf, et. al.[81] as being a consequence of the partial statistical equilibrium attained by the colliding system. They assumed that those nucleons allowed by their single particle wave functions to move along the internuclear axis would equilibrate first. Another explanation was proposed by Toepffer[82] who used a molecular wave function method assuming a deep inelastic mechanism in which an excited "neck" state is formed. Lee and Braun-Munzinger[83] explained the relation using a direct reaction model

which contests the partial equilibrium assumption. This picture assumes that transfer occurs by multiple sequential transfers which are kinematically matched. Karp, et. al.[84] have proposed a mechanism specifically designed for and tested on $^{16}O + ^{232}Th$, $^{15}N + ^{232}Th$, ^{181}Ta, and $^{35}Cl + ^{181}Ta$ at bombarding energies up to $1.4(E_C)$. The cross section was found to be dependent upon an effective optimal Q-value, Q_{opt}^{eff}, equal to the difference between the relative kinetic energy immediately before and after the transfer. Velocity matching conditions gave the formula:

$$Q_{opt}^{eff} = -(\Delta N/\mu_i)e_i \qquad (10)$$

ΔN = number of nucleons transferred

e_i = entrance channel kinetic energy at point of transfer

μ_i = entrance channel reduced mass

As ΔN increases, Q_{opt}^{eff} approaches the fully damped limit. Transfer is presumed to occur via a velocity-dependent frictional force. It should be noted that the relation in Ref. 80 becomes progressively worse at fitting the data, which are taken at a side angle $\theta_{lab} = 40^{\circ}$, as the bombardment energy decreases toward E_C and for light products closer to the projectile. This is understandable if it truly is a consequence of statistical processes as the realm where it is least applicable is that in which QET is most favored.

D. QUANTITATIVE TRANSFER THEORY

The attempts of workers to explain all aspects of all transfer channels in semi-classical collisions above the Coulomb barrier with one unifying model is of interest in the study of transfer. Kammuri and Matsuoka[85,86] have presented one of the most recent formulations; other earlier presentations are also of interest[53,87-89].

On a less complex and more useful level, the similarity of the massive transfer mechanism with complete fusion has inspired the proposal of a generalized limiting angular momentum sum rule model for these reactions[90,91]. For $l \leq l_{fu}$ complete fusion occurs. "Incomplete fusion" of a given cluster may occur at or below l_{lim}, which is the l of the projectile giving the cluster an angular momentum at or below the l_{fu} for the cluster plus target reaction system. The fraction of $l_{projectile}$ carried by the cluster is taken to be equal to its fractional mass. The lower bound of the l-window for a given transfer is the next-lowest l_{lim} for any other transfer.

The reaction probability for a given channel, assuming it is l-allowed, is taken from Bondorf, et. al. [81] to be

$$p(i) \sim \exp\left[(Q_{gg}(i) - Q_c(i))/T\right] \qquad (11)$$

where

Q_{gg} is the ground-state Q-value of the reaction in MeV;
$Q_c = q_c (Z_1^f Z_2^f - Z_1^i Z_2^i)e^2$, the change in
Coulomb energy during the reaction scaled by the parameter q_c; e = 1.44 MeV fm, q_c is in fm, and Q_c is in MeV.
T is the effective temperature, in MeV, another variable parameter.

$$l_{lim}(i) = \text{mass(projectile)/mass(cluster)} \times l_{fu} \tag{12}$$

is the limiting angular momentum for transfer of a given cluster, i.e., for the exit channel i.

$$T_l(i) = (1 + \exp(l - l_{lim}(i))/\Delta_l)^{-1} \tag{13}$$

is a "transmission coefficient", and Δ_l is a parameter controlling the cutoff sharpness;

$$N_l \sum_i T_l(i)\exp[(Q_{gg}(i) - Q_c(i))/T] = 1 \tag{14}$$

is the sum rule. For each l there must be found the normalization constant N_l such that the overall probability of a given transfer occuring, summed over all possible transfer channels at l, equals unity.

$$\sigma(i) = \pi\lambda^2 \sum_{l=0}^{l_m} (2l+1)N_l T_l(i)\exp[(Q_{gg}(i) - Q_c(i))/T] \tag{15}$$

is the cross section for a given channel and is obtained by summing the normalized reaction probablities over all l-waves. l_m is the highest l-value for which the total nucleus-nucleus potential is attractive, or which corresponds to the sum of the half-density radii of the colliding nuclei. Although this model was devised with the massive transfer mechanism in mind, it carries the requirement that all possible exit channels be included in the sum rule, and it has been used with some success in predicting cross sections for transfer channels[90,91]. This may be a result of using DIT-type reaction probabilities and three free parameters, but may reflect true l-limitations on each type of transfer and the fact that MT is seen at bombardment energies well above the Coulomb barrier. Massive transfer studies of 9.56 MeV/nucleon $^{16}O + ^{154}Sm$[69] and of 8.88 MeV/nucleon $^{16}O + ^{146}Nd$[68] showed that the average l of heavy products was proportional to the transferred mass, consistent with the l_{lim} hypothesis of this model.

E. OBSERVED CROSS SECTIONS AND DE-EXCITATION

Cross sections for sub-target actinides from LHI bombardments are well below those for trans-target products[92]. This is paralleled by the observation that yields of projectile-like products of stripping exceed those for pickup. One possible reason for this is that massive transfer, which, by the breakup-fusion assumptions, can only contribute to stripping, makes up a significant fraction of the transfer cross sections. Another consideration is that liquid drop properties of such an asymmetric system favor mass flow toward further asymmetry. This difference for the heavy product may be partly due to higher excitation of the sub-target fragment for which Q_{gg} will be positive, whereas for trans-target nuclides Q_{gg} is negative. This difference may not be offset by the Q_{rxn} differences for each process.

In transfer reactions heavy fragments with a range of Z and A are formed, each with an indeterminate amount of excitation energy and a narrow range of angular momentum centered near l_{gr}. In contrast, complete fusion produces a nucleus with a determinate Z and A and E* which may have an orbital angular momentum between 0 and l_{fu}. The statistical theories devised for compound nucleus de-excitation should apply to transfer products, with the proper initial conditions.

The excitation energy E* produced in transfer is expected to be completely absorbed by the heavy fragment. This is confirmed by the observation of weakly bound projectile-like products of

stripping[80,93].

$$E^* = Q_{gg} - Q_{rxn} \tag{16}$$

$$Q_{rxn} = E^f - E^i \tag{17}$$

$E^{(f,i)}$ equals the asymptotic (exit, entrance) channel center of mass kinetic energy

For DIT $E^f \simeq E^f_C$. For QET $E^f \simeq E^f_{opt}$, as calculated from an appropriate trajectory matching condition. One formula, by Toepffer[94], which is appropriate for semi-classical collisions and includes the "recoil" effects of mass exchange, is:

$$E^f_{opt} = E^i(Z_p, Z_T, / Z_p Z_T) \times ([1 - (m_x R_{p'} / m_p R_{min})] / [(m_T / m_{T'}) + (m_x R_{p'} / m_{T'} R_{min})]) \tag{18}$$

De-excitation of a primary nucleus may occur via particle evaporation, photon emission, or fission. In the actinide region, the fission barrier is comparable to the nucleon binding energy. Also, α evaporation is more favored energetically than in lighter nuclei. A further consideration is that at high angular momenta, as (E*, J) nears the yrast line, the fission and gamma emission widths increase at the expense of particle evaporation channels which carry away less angular momentum per MeV of excitation energy.

The width Γ_i for a de-excitation mode, i, is proportional to the level spacing times the sum of transmission coefficients taken over all channels for that mode. After Bohr and Wheeler[95]:

$$\Gamma_n = (S/2\pi)(2mR^2g/\hbar^2)\int_0^{E^*-B_n} \epsilon\rho(E^*-B_n-\epsilon)d\epsilon \qquad (19)$$

S = level spacing

ϵ = neutron kinetic energy

g = neutron intrinsic spin degeneracy

m = neutron mass

ρ = level density

This neutron evaporation width assumes a maximum neutron l corresponding to evaporation tangential to the surface.

$$\Gamma_f = (S/2\pi) \int_0^{E^*-E_f} \rho(E^*-E_f-K)dK \qquad (20)$$

ρ = energy level density at the saddle point

K = kinetic energy in the fission degree of freedom

E_f = fission barrier

This formula neglects penetration of the fission barrier.

$$\Gamma_n/\Gamma_f = (2mr_0^2gA^{(2/3)}/\hbar^2)(\int \epsilon\rho(E^*-B_n-\epsilon)d\epsilon)/ \int \rho(E^*-E_f-K)dK) \qquad (21)$$

For a constant temperature level density ρ = const x exp(E*/T)

$$\Gamma_n/\ \Gamma_f = (2TA^{(2/3)}/K_o)\exp[(E_f-B_n)/T] \qquad (22)$$

$K_o = \hbar^2/(2mr_o^2) \cong 10$ MeV

This formula is suitable for nuclides for which E_f and B_n are comparable and over a limited range of E*.

The Fermi gas level density, ρ = const x $\exp[2(aE)^{(1/2)}]$, may be used to incorporate excitation energy dependence.

$$\Gamma_n/\ \Gamma_f = 4A^{(2/3)}a_f(E^*-B_n)/(K_o a_n[2a_f^{1/2}(E^*-E_f)^{1/2}-1]) \times \exp[2a_n^{1/2}(E^*-B_n)^{1/2}-2a_f^{1/2}(E^*-E_f)^{1/2}] \qquad (23)$$

$a_{f,n}$ is the level density parameter for fission, neutron levels.

Experimental data is used to fit $\Gamma_n/\ \Gamma_f$ to find values for a_f/a_n and E_f-B_n; see Ref. 96, for example. Eqns. 19-23 are taken from Ref. 97.

The constant-temperature effective-barrier model of compound-nucleus decay presented by Sikkeland[98] uses a level density which takes into account the effect of angular momentum on relative decay channel widths.:

$$(\ \Gamma_n/\ \Gamma_f)_{l=0}\exp[-Bl(l+1)] \qquad (24)$$

$$B = (\hbar^2/2T) \times (1/I - 1/I_s) \qquad (25)$$

$T = 1.3$ MeV

$I^o_{rig} = (2/5) \times r_o^2 A^{5/3}$ amu/fm^2, $r_o = 1.22$ fm

$I^{sad}_{rig} = (1/4) r_o^2 A^{5/3}$ amu/fm^2

$I/I_{rig} = 1.5$

T is a level density temperature parameter, with units of energy, and I/I_{rig} is an adjustable moment of inertia parameter. Both are determined by fits of compound nucleus residue cross sections in the actinide region. I^o_{rig} and I^{sad}_{rig} are rigid body moments of inertia for spherical and saddle shapes, respectively.

Ideally, the statistical model could be used to exactly calculate Γ_n / Γ_f. However, the heights and shapes of the fission barriers must be accurately known. They have been measured for isotopes of Th through Fm which are formed as two-, one-, or zero-net nucleon transfer products from $^{1,2,3}H$, or ^3He bombardments of available targets[99-104], and for Pu isotopes formed in the fusion of ^4He with ^{238}U and subsequent neutron evaporation[105]. These measurements were done by fitting the probability of fission as a function of excitation with a statistical model for which the fission barrier properties are adjustable parameters. Present knowledge of fission in the actinide region is insufficient for use, without adjustable parameters, to predict Γ_n / Γ_f for a nuclide formed in a heavy ion reaction, if only N, Z, E*, and l are known.

III. EXPERIMENTAL

A. BEAM AND TARGET

All bombardments were done with $^{18}O^{+4}$ accelerated at the 88-inch cyclotron at Lawrence Berkeley Laboratory.

The ^{245}Cm and ^{249}Cf targets were supplied by Ron Lougheed of Lawrence Livermore Laboratory. They were made by vacuum deposition of the actinide trifluoride onto Be foil as a 6 mm diameter disk. The curium target contained .240 mg/cm^2 ^{245}Cm and was on a 3.2 mg/cm^2 Be foil, and the californium target .520 mg/cm^2 ^{249}Cf on a 2.13 mg/cm^2 Be backing.

B. APPARATUS

The target was mounted in a water cooled copper block and was itself cooled on its back face by a stream of N_2 gas at 50 SCFM. A Havar foil 1.8 mg/cm^2 thick, the "beam window", separated the N_2 chamber from the vacuum of the beam line. In some bombardments either a 1.92 mg/cm^2 Havar foil or a 2.3 mg/cm^2 Be foil or both were placed upstream of the target apparatus to function as beam energy degraders.

Products recoiling out of the target were caught in a stack of ten .1 mg/cm^2 aluminum "catcher" foils 2.54 cm in diameter. The stack was mounted in a chamber through which He cooling gas flowed at a pressure of 4 mm Hg, oriented parallel to and coaxial with the target and the closest foil was .3 cm from the target face. Each catcher foil was mounted on a flat brass ring, also 2.54 cm in inner diameter. The rings were indented so that, when stacked, they held one another apart and permitted the flow of He to pass among the foils The entire assembled stack was between 1.7 and 1.8 cm thick.

Figure 2 illustrates the target assembly and catcher chamber. Figure 3 is a schematic of the bombardment apparatus.

Bombardment energies were calculated using Northcliffe and Schilling stopping power tables[106] (NS) to estimate the beam energy loss through the various foils and gas to the center of the target. The Ni tables were used for Havar and the values for Cm and Cf were obtained via linear extrapolation by atomic number from the values given for Au and U. The thickness of the N_2 gas was

C. ACCUMULATION OF DATA

Immediately after the end of a bombardment the catcher foil stack was removed from the He chamber and disassembled. Each foil was sprayed on one side with Krylon clear paint and dried under a heat lamp. This coat of paint added mechanical strength, which was needed because of the frequent handling of samples from different experiments as they were cycled through the detectors over several months. Each foil was then placed over one of ten 2.54 cm diameter Ortec Si(Au) surface barrier detectors. The signals from each detector were routed through a pulse-height analyzer. A PDP-15 computer tagged each event with time and channel coordinates and entered the record into a memory buffer and onto magnetic tape for later analysis.

Accumulation of alpha spectra and fission events began about 7 minutes after the end of bombardment.

D. RESOLUTION AND EFFICIENCY

The aluminum catcher foils were thick enough so that the stack of ten was sufficient to stop recoiling target-like fragments, yet thin enough that the alpha spectra were degraded less than .02 MeV and were not excessively broadened. The FWHM of the ^{248}Cf peak, for example, was less than .04 MeV, and .98 of the total peak was contained within .26 MeV. A typical alpha spectrum is shown in Figure 4.

In some of the ^{249}Cf experiments the extremely high yield of ^{252}Fm led to contamination of the detectors with its daughter ^{248}Cf recoiling out of the foil. To correct for this, following every ^{249}Cf experiment, no other samples were rotated into the detectors until all ^{252}Fm had decayed. Background counts were then made and used to correct ^{248}Cf peaks in subsequent spectra.

The efficiency of the Si(Au) detectors was measured with a standard alpha emitting ^{241}Am source and found to be .26 ± .013. In OCf-III and OCf-II, the mounted foils were placed in the detector with the frame side down, and the indentations held the foil further away from the detector surface. For this configuration the efficiency was measured to be .22 ± .012. The detector efficiency for fission was taken to be twice the alpha efficiency.

IV. ANALYSIS OF DATA

A. TOTAL STACK SPECTRA

The decay curve of each observed peak in each total-stack alpha spectrum was constructed and fit via an error-weighted least-squares analysis, using the code FUTILE[107]. Nuclides were identified by E_α and by the half-lives found by the least-squares fit. When the components of a decay curve were identified, the curve was refit, with the half-lives of the known components held fixed at the values given in the Table of Isotopes[108]. Table II gives the decay properties of measured nuclides.

B. FOIL SPECTRA

It was assumed that the components of the decay curves of the spectra; of the individual foils were the same as those of the total spectra. For some peaks, the shortest component of the total-stack decay curve could not be identified. In this case, the half-life that best fit the total-stack decay curve was used, and held fixed, for the fit of the individual foil decay curves.

Table II. Decay Properties of Observed Nuclides (Ref. 108).

NUCLIDE	decay mode (abundance)	half-life	principal E_α (MeV)
^{250}Fm	α (1.0)	30 min.	7.42
^{251}Fm	α (.018)	5.3 hr.	6.834
^{252}Fm	α (1.0)	25.4 hr.	7.04
^{253}Fm	α (.12)	3.0 days	6.943,6.674
^{254}Fm	α (1.0)	3.240 hr.	7.187
^{256}Fm	SF (.919)	2.63 hr.	
^{251}Es	α (.005)	33 hr.	6.492
^{252}Es	α (.78)	472 days	6.632
^{253}Es	α (1.0)	20.47 days	6.633
^{254m}Es	β, to ^{254}Fm (.9959)	39.3 hr.	7.187
^{245}Cf	α (.3)	44 min.	7.137
^{246}Cf	α (1.0)	35.7 hr.	6.758,6.719
^{248}Cf	α (1.0)	333 days	6.26
^{250}Cf	α (1.0)	13.1 yr	6.031.5.989
^{242}Cm	α (1.0)	162.8 days	6.113,6.070

C. CROSS SECTION AND RECOIL RANGE DISTRIBUTION

If no parents were observed for a nuclide, its recoil range distribution was calculated from the individual foil A∘'s. Otherwise, the cross section of the parent for each foil was calculated and used with the daughter A∘ to calculate each of the ten individual-foil cross sections. These were used to obtain the recoil range distribution. Figures 5 through 22 show the observed recoil range distributions.

The cross section of a given nuclide was calculated from the sum of the A∘'s from the decay curve of every interval of the total-stack spectrum in which it was observed. If a parent of the nuclide was observed, the daughter cross-section was corrected for feeding during the bombardment. Table III lists the cross sections for the OCf experiments, and Table IV lists those for the OCm experiments. Figures 23-25 show the excitation functions for OCf and Figures 26-28 show those for OCm.

Error bars are standard deviations and include the statistical uncertainties from count rates and least-squares fits and the detector efficiency uncertainty.

There was a significant amount of activity in the alpha spectra from products of ^{18}O reaction with Pb impurity in the target. In some cases, this led to difficulties and possible errors in the decay curve analyses and cross section measurements. Cross sections reported in Ref. 3, a radiochemical study of cross sections from these systems, should be more accurate. It is encouraging to note

TABLE III. Cross sections in microbarns for products of ^{18}O + ^{249}Cf

	BOMBARDMENT ENERGY (LAB) (MeV)			
PRODUCT	111.6	99.8	89.2	83.
^{250}Fm	74. ± 3.6	15.4 ± .75	.22 ± .012	.05 ± .18
^{251}Fm	1080. ± 57.	790. ± 40.	28. ± 1.5	.3 ± .12
^{252}Fm	870. ± 43.	1530. ± 74.	530. ± 28.	.069 ± .0062
^{253}Fm	250. ± 13.	430. ± 21.	260. ± 14.	.01 ± .20
^{254}Fm	43. ± 2.1	61. ± 3.0	10.9 ± .58	.008 ± .0022
^{256}Fm	0. ± .038	.07 ± .033	.047 ± .0080	.0004 ± .00018
^{251}Es	5000. ± 250.	4000. ± 200.	390. ± 23.	12. ± .1.3
^{252}Es	660. ± 35.	1270. ± 62.	650. ± 42.	.6 ± .25
^{253}Es	300. ± 17.	580. ± 29.	90. ± 5.1	.08 ± .021
^{254m}Es	.38 ± .028	.40 ± .021	.22 ± .014	.037 ± .0050
^{246}Cf	146. ± 8.2	53. ± 3.1	1.8 ± .13	.36 ± .173
^{248}Cf	14300. ± 700.	15200. ± 740.	2500. ± 130.	540. ± 31.
^{250}Cf	23000. ± 1200.	27000. ± 1300.	9900. ± 580.	0. ± 33.

TABLE IV. Cross sections in microbarns for products of ^{18}O + ^{245}Cm

	BOMBARDMENT ENERGY (LAB) (MeV)		
PRODUCT	111.6	99.6	93.
^{252}Fm	1.71 ± .088	2.3 ± .12	2.6 ± .13
^{252}Es	0. ± 24.	6.3 ± 2.7	6.9 ± 2.5
^{253}Es	1.1 ± .24	.57 ± .22	.25 ± .17
^{245}Cf	2.7 ± .16		.02 ± .140
^{246}Cf	154. ± 7.5	85. ± 4.1	37. ± 1.8
^{248}Cf	1650. ± 81.	2020. ± 99.	2500. ± 120.
^{242}Cm	280. ± 14.	153. ± 7.8	

that the cross sections presented here agree with most of those presented in Ref. 3. One outstanding exception is ^{253}Es; my cross sections are about an order of magnitude too high. This casts in doubt all the recoil range distributions presented for ^{253}Es.

D. RECOIL RANGE TECHNIQUE

A fragment's recoil range is a measurement of the projection of its velocity, i.e., E/m, in the laboratory frame along the beam axis. In these analyses, the conversion of range to velocity was made using the NS range tables. In these experiments, the fragment velocity was around .02 to .03 MeV/nucleon. At this speed, nuclear stopping becomes as important as electronic stopping[109-111]. Estimates using the nuclear stopping power curve in Ref. 112 and the electronic stopping power calculated with Eqn. 26 below predict that from .2 to .8 of the total stopping power at the velocities typical of these experiments will be due to nuclear stopping. Electronic stopping at low velocity is described by a simple function:

$$-(dE/dx) = \text{const} \times E^{1/2} \qquad (26)$$

There were two ways to independently check the accuracy of the range tables in these experiments. One was to examine the range distribution of target nuclei which it may be assumed have been elastically scattered and therefore have a very definite upper limit on their lab axial velocity. The other was to check the recoil range of products of a bombardment of ^{238}U with ^{12}C[31]. In this reaction, Cf isotopes were observed, which are produced via compound nucleus formation, and therefore also have a definite upper limit on their recoil energy. In OCf-II, the recoil range of a ^{249}Cf nucleus scattered elastically in a head-on collision, is

calculated to be 1.00 mg Al/cm^2. Subtraction of half the target thickness gives the maximum range as .96 mg Al/cm^2, corresponding to the 10th foil. The statistics are poor, but the recoil range distribution (Figure 13c.) indicates that the range of ^{249}Cf extends to foil 10. Using the recoil range distributions for Cf isotopes formed via compound nucleus and recoiling into a stack of .040 mg/cm^2 carbon foils, conservation of momentum and the NS tables predict a range for Cf of .203 mg C/cm^2. Taking into account the target thickness, this would predict a peak in the distribution to be in the fourth foil, where it is observed.

Therefore, at these low energies, it seems that the NS tables describe the ranges of these heavy fragments accurately enough for this investigation, and they were used in all conversions of range to energy.

Range straggling is expected to be significant for such heavy nuclei at such low velocities[109]; however, it was neglected in this analysis.

E. CONVERSION OF RANGE TO ANGULAR DISTRIBUTION

The range of a recoiling fragment in a stack of foils coaxial with and normal to the incident beam depends upon the speed of the fragment parallel to the beam axis, and thus upon the magnitude and direction of its velocity in the laboratory frame of reference. Those are determined by the velocity of the center of mass, which is a function of the initial mass and velocity of the projectile and target, and by the speed and angle of separation of the exit channel fragments in the center of mass frame. These latter properties are measurements of the Q_{rxn} and the angular distribution, respectively, of the reaction, given the mass of the exit fragments. One may work backward from the recoil range of an identified fragment to deduce the Q_{rxn} or the separation angle θ, providing the other is known. Recoil range, as a measure of the fragment's axial lab velocity, is insufficient.

Consider a projectile of mass A_p and lab velocity v_p colliding with a target of mass A_T. In the center of mass frame of reference, the projectile has velocity $V_p = A_T v_p/(A_p + A_T)$ and the target $V_T = V_p - v_p$. In the lab frame the velocity of the center of mass is $v_{cm} = -V_T$. In the collision, mass may be transferred, and energy Q_{rxn} is released. Products of mass $A_{p'}$ and $A_{T'}$ separate with asymptotic relative kinetic energy $E^f = E^i + Q_{rxn}$, each at an angle θ with respect to its initial c.m.s. velocity. The heavy fragment has c.m.s. velocity $V_{T'}$ determined by E^i, Q_{rxn}, $A_{p'}$, $A_{T'}$, and conservation of

energy and momentum. The conversion of V_T, to lab velocity v_T, of the heavy fragment is:

$$v_T,\cos\phi_T, = V_T,\cos\theta_H + v_{cm} \qquad (27)$$

where ϕ_T is the lab angle of the heavy fragment and θ_H is the c.m.s. scattering angle of the heavy fragment T'.

$v_T,\cos\phi_T,$ is a direct measure of the recoil range. If Q_{rxn} is known, the recoil range distribution directly gives the angular distribution. Conversely, if the angular distribution is known, it can be combined with the recoil range distribution to give the Q_{rxn}. Neither Q_{rxn} nor the angular distribution are known in these measurements. However, if it is assumed that only QET and DIT contribute, that QET is associated with $Q_{rxn} = Q_{opt}$ and an angular distribution peaked at $\theta > 0^\circ$, and that DIT has Q_{rxn} corresponding to Coulomb separation and an angular distribution peaked at 0° and decreasing exponentially, one may iteratively extract angular distributions from recoil range distributions, as described below.

F. USE OF THE CODE RECOILS

The NS range tables[106] were used for all velocity calculations, in the form of an algorithm[113] fit to the tabulated values for aluminum.

The thickness, Th, of any other medium, M, in mg/cm^2 was converted to thickness in mg Al(equivalent)/cm^2 by the equation:

$$Th_{Al\ (equivalent)} = Th_M\ [(dE/dx)_M/(dE/dx)_{Al}] \qquad (28)$$

Stopping powers at .025 MeV/nucleon from NS electronic stopping power tables were used in this equation.

The code RECOILS, described in Ref. 113, was used to analyze recoil range distributions. This code uses the range algorithm and the center-of-mass to lab transformation equations to explicitly calculate the axial range of a target-like fragment from entrance channel conditions and an angular distribution provided by the user, at one degree intervals of c.m.s. angle through 180 degrees. It constructs a predicted range distribution by integrating this information. Originally, the final kinetic energy was calculated to be the exit channel Coulomb barrier. A modification was made so that the final kinetic energy at each angle is an average of the optimum and the Coulomb separation energies, weighted in proportion to the contribution of the QET and DIT mechanisms, respectively, to the angular distribution at that angle:

$$P(\theta) = PG\ ((\theta_{graz}-\theta)^2/(2(\sigma^2)) + PE\ (.693\ \theta/\theta_{half}) \quad (29)$$

$$= PRGAUS + PREX$$

$$E^f_{sepn} = (PRGAUS \times E^f_{opt} + PREX \times E^f_C)/P(\theta) \quad (30)$$

$P(\theta)$ = fraction of reactions with separation angle θ

PG = relative contribution of QET (approximated by gaussian distribution centered at θ_{gr})

PE = relative contribution of DIT (approximated by distribution peaked at 0° and decreasing exponentially with a slope defined by θ_{half})

The axial range values calculated at each angle increment may also be used in reverse, to transform a range interval, as in a catcher foil, to a range of c.m.s. angles, again, provided the mechanism is known.

Following is a detailed description of the use of this assumption and a recoil range distribution to deduce an angular distribution. An experimental angular distribution requires only that the interval of center-of-mass angles represented by each catcher foil is known. Because the exit channel kinetic energy is angle-dependent, the angular distribution must be known. This difficulty is overcome by first approximating the E^f_{sepn} as E^f_C at all angles, explicitly calculating the axial range at each angle under this condition. Table V contains these values for fermium products of OCf-IV. (Half of the target thickness in mg Al/cm^2 has been subtracted from the tabulated values of the axial

Table V. Axial ranges of Fm as functions of c.m.s. angle e for fully damped collision as calculated by RECOILS.

CMS ANGLE (DEG)	AXIAL RANGE (MG AL/CM^2)	CMS ANGLE (DEG)	AXIAL RANGE (MG AL/CM^2)
0.	1.02	41.	.86
1.	1.02	42.	.85
2.	1.02	43.	.84
3.	1.01	44.	.84
4.	1.01	45.	.83
5.	1.01	46.	.82
6.	1.01	47.	.81
7.	1.01	48.	.81
8.	1.01	49.	.80
9.	1.01	50.	.79
10.	1.01	51.	.78
11.	1.00	52.	.77
12.	1.00	53.	.76
13.	1.00	54.	.76
14.	1.00	55.	.75
15.	.99	56.	.74
16.	.99	57.	.73
17.	.99	58.	.72
18.	.98	59.	.71
19.	.98	60.	.70
20.	.98	61.	.69
21.	.97	62.	.68
22.	.97	63.	.67
23.	.96	64.	.67
24.	.96	65.	.66
25.	.96	66.	.65
26.	.95	67.	.64
27.	.95	68.	.63
28.	.94	69.	.62
29.	.94	70.	.61
30.	.93	71.	.60
31.	.92	72.	.59
32.	.92	73.	.58
33.	.91	74.	.57
34.	.91	75.	.56
35.	.90	76.	.55
36.	.89	77.	.54
37.	.89	78.	.53
38.	.88	79.	.52
39.	.87	80.	.51
40.	.87		

Table V. Continued.

CMS ANGLE (DEG)	AXIAL RANGE (MG AL/CM^2)	CMS ANGLE (DEG)	AXIAL RANGE (MG AL/CM^2)
81.	.50	121.	.16
82.	.49	122.	.15
83.	.48	123.	.15
84.	.47	124.	.14
85.	.46	125.	.14
86.	.45	126.	.13
87.	.44	127.	.12
88.	.43	128.	.12
89.	.42	129.	.11
90.	.42	130.	.11
91.	.41	131.	.10
92.	.40	132.	.096
93.	.39	133.	.091
94.	.38	134.	.086
95.	.37	135.	.081
96.	.36	136.	.076
97.	.35	137.	.071
98.	.34	138.	.067
99.	.33	139.	.063
100.	.32	140.	.058
101.	.31	141.	.054
102.	.31	142.	.050
103.	.30	143.	.046
104.	.29	144.	.043
105.	.28	145.	.039
106.	.27	146.	.036
107.	.26	147.	.032
108.	.26	148.	.029
109.	.25	149.	.026
110.	.24	150.	.023
111.	.23	151.	.020
112.	.22	152.	.017
113.	.22	153.	.014
114.	.21	154.	.012
115.	.20	155.	.009
116.	.19	156.	.007
117.	.19	157.	.004
118.	.18	158.	.002
119.	.17	159.	.000
120.	.17	160.	-.002

Table V. Concluded.

CMS ANGLE (DEG)	AXIAL RANGE (MG AL/CM^2)	CMS ANGLE (DEG)	AXIAL RANGE (MG AL/CM^2)
161.	-.004	171.	-.018
162.	-.006	172.	-.019
163.	-.007	173.	-.020
164.	-.009	174.	-.020
165.	-.010	175.	-.021
166.	-.012	176.	-.021
167.	-.013	177.	-.022
168.	-.015	178.	-.022
169.	-.016	179.	-.022
170.	-.017	180.	-.022

range.) The interval of angles corresponding to foil 10 is accordingly found to be 12° to 34°, that corresponding to foil 9 is 34° to 48° and so forth. The yield in each foil, divided by $\Delta\theta$, and plotted at the midpoint of the angle interval, gives a first approximation of the angular distribution. This first approximation was graphically resolved into exponential and gaussian components, and estimates of the five paramters of Eqn. 29 were made. This angular distribution was used to recalculate the axial range versus angle, with the angular dependence of kinetic energy turned on.

Table VI shows axial range versus c.m.s. angle for the recalculation. If the recoil range distribution predicted in this calculation was close to the observed distribution, no further refinements of the angular distribution were made. It was found that the interval of angles corresponding to each foil was resistant to further adjustments in these parameters and it is that conversion that allows the construction of experimental angular distributions from recoil ranges.

Figures 29 through 40 show the experimental relative angular distributions for OCf-II, -III, -IV and OCm-I, -II, -III. The absolute differential cross section $d\sigma/d\theta$ may be recovered from the relative value by multiplication by the total cross section for that nuclide. Tables VII through X show the predicted recoil ranges versus those observed for OCf-IV. The other experiments showed similar quality of range distribution prediction.

Table VI. Axial ranges of Fm as functions of c.m.s. angle θ for angle-dependent E^f_{sepn} as calculated by RECOILS.

CMS ANGLE (DEG)	AXIAL RANGE (MG AL/CM^2)	CMS ANGLE (DEG)	AXIAL RANGE (MG AL/CM^2)
0.	.97	41.	.83
1.	.97	42.	.82
2.	.97	43.	.81
3.	.97	44.	.81
4.	.97	45.	.80
5.	.97	46.	.79
6.	.97	47.	.79
7.	.97	48.	.78
8.	.97	49.	.77
9.	.97	50.	.76
10.	.96	51.	.75
11.	.96	52.	.75
12.	.96	53.	.74
13.	.96	54.	.73
14.	.96	55.	.72
15.	.95	56.	.72
16.	.95	57.	.71
17.	.95	58.	.70
18.	.94	59.	.69
19.	.94	60.	.68
20.	.94	61.	.67
21.	.93	62.	.67
22.	.93	63.	.66
23.	.93	64.	.65
24.	.92	65.	.64
25.	.92	66.	.63
26.	.91	67.	.62
27.	.91	68.	.61
28.	.90	69.	.60
29.	.90	70.	.59
30.	.89	71.	.59
31.	.89	72.	.58
32.	.88	73.	.57
33.	.88	74.	.56
34.	.87	75.	.55
35.	.87	76.	.54
36.	.86	77.	.53
37.	.85	78.	.52
38.	.85	79.	.51
39.	.84	80.	.50
40.	.83		

Table VI. Continued.

CMS ANGLE (DEG)	AXIAL RANGE (MG AL/CM^2)	CMS ANGLE (DEG)	AXIAL RANGE (MG AL/CM^2)
81.	.49	121.	.17
82.	.48	122.	.16
83.	.48	123.	.15
84.	.47	124.	.15
85.	.46	125.	.14
86.	.45	126.	.14
87.	.44	127.	.13
88.	.43	128.	.13
89.	.42	129.	.12
90.	.41	130.	.11
91.	.40	131.	.10
92.	.39	132.	.10
93.	.38	133.	.099
94.	.38	134.	.094
95.	.37	135.	.090
96.	.36	136.	.085
97.	.35	137.	.080
98.	.34	138.	.076
99.	.33	139.	.072
100.	.32	140.	.068
101.	.32	141.	.064
102.	.31	142.	.060
103.	.30	143.	.056
104.	.29	144.	.053
105.	.28	145.	.049
106.	.27	146.	.046
107.	.27	147.	.042
108.	.26	148.	.039
109.	.25	149.	.036
110.	.24	150.	.033
111.	.24	151.	.030
112.	.23	152.	.027
113.	.22	153.	.024
114.	.21	154.	.022
115.	.21	155.	.019
116.	.20	156.	.017
117.	.19	157.	.015
118.	.19	158.	.012
119.	.18	159.	.010
120.	.17	160.	.008

Table VI. Concluded.

CMS ANGLE (DEG)	AXIAL RANGE (MG AL/CM^2)	CMS ANGLE (DEG)	AXIAL RANGE (MG AL/CM^2)
161.	.006	171.	-.008
162.	.004	172.	-.009
163.	.003	173.	-.010
164.	.001	174.	-.010
165.	-.001	175.	-.011
166.	-.002	176.	-.012
167.	-.003	177.	-.012
168.	-.005	178.	-.012
169.	-.006	179.	-.012
170.	-.007	180.	-.012

Table VII. Predicted and Observed Recoil Range Distribution.
OCf-IV. Fm. $\theta_{max}=70^{\circ}$, FWHM=46°, PG=.578, $\theta_{1/2}=30^{\circ}$, PE=1.0

PREDICTED		OBSERVED				
FOIL	Fm	^{250}Fm	^{251}Fm	^{252}Fm	^{253}Fm	^{254}Fm
1	.21	.11 ± .062	.19 ± .013	.18 ± .010	.18 ± .011	.163 ± .0088
2	.22	.159 ± .0088	.20 ± .013	.23 ± .012	.20 ± .012	.21 ± .011
3	.21	.21 ± .011	.21 ± .014	.23 ± .012	.2 ± .14	.22 ± .012
4	.16	.18 ± .010	.17 ± .011	.158 ± .0083	.17 ± .010	.161 ± .0087
5	.096	.122 ± .0068	.082 ± .0072	.087 ± .0046	.091 ± .0059	.101 ± .0055
6	.051	.097 ± .0055	.073 ± .0065	.058 ± .0031	.065 ± .0046	.068 ± .0038
7	.025	.060 ± .0035	.042 ± .0048	.033 ± .0018	.033 ± .0029	.044 ± .0025
8	.014	.034 ± .0022	.023 ± .0034	.0168± .00090	.018 ± .0019	.022 ± .0014
9	.0085	.018 ± .0013	.012 ± .0053	.0090± .00084	.009 ± .0011	.0125± .00084
10	.0039	.0093± .00080	.006 ± .0019	.0041± .00022	.0057± .00085	.0051± .00043

Table VIII. Predicted and Observed Recoil Range Distribution.
OCf-IV. Es. $\theta_{max}=72^{\circ}$, FWHM=46°, PG=.81, $\theta_{1/2}=30^{\circ}$, PE=1.0

PREDICTED		OBSERVED			
FOIL	Es	^{251}Es	^{252}Es	^{253}Es	^{254m}Es
1	.19	.3 ± .14	.15 ± .012	.17 ± .016	.13 ± .026
2	.21	.23 ± .013	.17 ± .013	.23 ± .019	.20 ± .032
3	.21	.18 ± .010	.22 ± .016	.23 ± .020	.16 ± .029
4	.16	.135 ± .0078	.17 ± .013	.14 ± .015	.13 ± .026
5	.11	.078 ± .0047	.110 ± .0093	.09 ± .011	.11 ± .023
6	.061	.056 ± .0034	.080 ± .0074	.063 ± .0089	.12 ± .024
7	.031	.035 ± .0023	.052 ± .0057	.043 ± .0071	.08 ± .021
8	.016	.017 ± .0012	.024 ± .0035	.015 ± .0043	.03 ± .012
9	.0087	.0084± .00074	.012 ± .0024	.012 ± .0033	.04 ± .013
10	.0053	.0044± .00047	.006 ± .0017	.007 ± .0025	.01 ± .010

Table IX. Predicted and Observed Recoil Range Distribution. OCf-IV. $^{246,248}Cf$. $\theta_{max}=81°$, FWHM=40°, PG=.3, $\theta_{1/2}=22°$, PE=1.0

	PREDICTED	OBSERVED	
FOIL	$^{246,248}Cf$	^{246}Cf	^{248}Cf
1	.22	.160 ± .0094	.135 ± .0072
2	.15	.148 ± .0091	.154 ± .0082
3	.16	.17 ± .0106	.20 ± .011
4	.15	.156 ± .0097	.179 ± .0094
5	.12	.110 ± .0068	.123 ± .0065
6	.087	.098 ± .0060	.097 ± .0051
7	.053	.068 ± .0041	.060 ± .0032
8	.028	.044 ± .0027	.031 ± .0017
9	.014	.029 ± .0017	.0159 ± .00093
10	.0069	.017 ± .0011	.0075 ± .00049

Table X. Predicted and Observed Recoil Range Distribution OCf-IV. $^{249,250}Cf$. $\theta_{max}=60°$, FWHM=54°, PG=.0001, $\theta_{1/2}=30°$, PE=1.0

	PREDICTED	OBSERVED	
FOIL	$^{249,250}Cf$	^{249}Cf	^{250}Cf
2	.28	.44 ± .068	.28 ± .059
3	.19	.24 ± .037	.25 ± .054
4	.14	.14 ± .022	.20 ± .042
5	.11	.08 ± .012	.12 ± .025
6	.085	.046 ± .0073	.08 ± .017
7	.068	.027 ± .0044	.042 ± .0091
8	.054	.014 ± .0024	.024 ± .0052
9	.044	.007 ± .0013	.011 ± .0026
10	.034	.0027 ± .00064	.005 ± .0013

Least-squares fitting of the experimental angular distributions was attempted, but convergence was possible in only the cases with the best counting statistics. The number of values (10) versus the number of parameters (5) was just too large; even neglecting the considerable uncertainty in θ, the standard deviation in the parameters was around .5. The fitted parameters were no better at predicting the recoil range distributions than those estimated by inspection and the angle-to-foil transformation was the same.

V. DISCUSSION

A. RECOIL RANGE DISTRIBUTIONS.

The shape of the recoil range distributions for heavy transfer products can be related to the kinematics of the mechanism responsible for its production. The kinetic energy and angle of products of CF and MT are restricted to a narrow range of values by the kinematics of the mechanism. The recoil ranges are therefore narrow and drop off sharply at the high-range end. For QET and DIT any of a wide range of separation energies and angles are allowed and are observed. The recoil range distribution of the heavy fragment is peaked at a projected range corresponding to θ_{max}, the separation angle at which the angular distribution reaches a maximum, and drops off gradually at higher ranges. It is a matter of inspection to distinguish QET/DIT from CF or MT on the basis of the shape of the recoil range distribution.

The limitations on the kinetic energy and angle of the compound nucleus make the recoil range distribution for a product formed from a compound nucleus easily distinguishable from that from a transfer mechanism. The conservation of momentum requires that the lab kinetic energy of the compound nucleus be $E^{i}_{lab}(A_1)/(A_1 + A_2)$ and that the lab angle be 0°. Accordingly, the peak of the recoil range distribution gradually increases in a linear fashion with increasing bombardment energy. Any spread in the distribution is due to range straggling and to the influences of recoil from

particle evaporation on the trajectory of the compound nucleus. As a result the bulk of the cross section is contained within a much smaller range window than that required to stop recoiling transfer products.

In MT, the light particle is emitted at a forward angle with velocity distributed about the beam velocity. For a transfer of cluster X, one would expect a recoil range distribution peaked at a value corresponding to:

$$E_X = A_X^2 E_P / [A_P(A_X + A_T)]$$

which would be lower than the CN peak range, and which drops off sharply at higher ranges, like the CN distribution.

QET would be expected to display a peak corresponding to the grazing angle with a high range tail corresponding to lower angles. DIT would be expected to give recoil range distributions that peak at an extremely low range, from backward recoil of the heavy fragment for $\theta=0^\circ$, and also show a high range tail.

It is interesting to note that the study of Hahn, et. al.[31] of angular distributions, recoil range distributions, and cross sections of $^{238}U(^{12}C, xn)Cf$ and $^{239}Pu(^{12}C,\alpha xn)Cf$, that is, via compound nucleus and transfer, respectively, gave examples of all three shapes. Clearly, the ^{238}U-generated Cf must be from a compound nucleus. The experiment was designed to elucidate the mechanism by which ^{239}Pu-generated Cf was formed from ^{12}C bombardment. The range distributions of the compound nucleus

products were narrow; the relative activity fell to less than .1 of that of the peak in the second or third foil past the peak. Over the range of bombardment energies, the peak stayed in the same foil. The recoil range and angular distributions of the ^{239}Pu products showed that these were not formed from α particle evaporation from a compound nucleus.

Certain features of the recoil range distributions are especially interesting. At the two lowest bombardment energies, which were between the Coulomb barrier and about 7 MeV per nucleon, the distribution was broad; over the ten 40 $\mu g/cm^2$ carbon foils, the relative activity in each foil was within a factor of ten of that in any other. Also, the peak of the distribution was at a shorter range for the higher energy bombardment. The angular distribution of these products peaked near the grazing angle[114], and also had a forward-peaked component. At higher bombardment energies, a change in mechanism was noticed as the angular distribution became more forward-peaked, with θ_{lab}^{max} less than 5°, and lost its side-peak. The range distributions became narrow, and peaked at a range shorter than those for the low energy transfer or compound nucleus products. The distribution dropped sharply past the peak and the peak was insensitive to increasing bombardment energy.

This latter distribution looks like a compound nucleus range distribution, and the peak position is consistent with break-up of the ^{12}C into a spectator ^{4}He and a ^{8}Be which fuses with the target. For example, for the 90.0 MeV ^{12}C, if one assumes the

reaction is essentially a complete fusion between ^{8}Be at the beam velocity and ^{239}Pu, with the remaining ^{4}He acting as a non-participant, a range of .09 mg C/cm^2 is predicted from conservation of momentum and the NS tables, which matches the observed peak in the range distribution. This mechanism for multinucleon transfer appears to be massive transfer, and was recognized at the time to be distinct from the mechanism operating at lower bombardment energies on the basis of both recoil range and angular distributions.

The distributions observed in this study for products of these transfer reactions show several features that can be related to features of the QET/DIT mechanism. There is usually one peak, which moves to shorter ranges with increasing bombardment energy. At higher ranges, the yield falls off quite gradually. In some cases, another very short range peak might be observed in the first foils. The longer range peak is a projection of the side angle peak in the angular distribution. It moves to shorter ranges with increasing projectile energy because, although the center-of-mass separation energy and the lab velocity of the center of mass are increasing, the c.m.s. grazing angle is decreasing. Therefore, the heavy fragment is recoiling at an increasingly backward c.m.s. angle. Eqn. 27 shows that this results in an overall decrease in the axial velocity in the laboratory frame.

The very short range peak originates in the exponential (DIT) part of the angular distribution. For these reactions, the maximum of this component is expected to be at or near 0° (c.m.s), which

translates to 180° for the heavy fragment, and, in the lab frame, to a very short axial range. At a lower bombardment energy a heavy fragment emitted at 180° may not escape the target, and may even recoil into the target backing.

The long high-range tail of the range distribution reflects the wide range of separation energy and angle allowed by the two-body nature of the QET/DIT exit channel. The tail consists of heavy partners of light products scattered at angles greater than θ_{gr}. The breadth of the gaussian (QET) component and the size of the half-angle of the exponential (DIT) component of the angular distribution both contribute to the slope of the range tail.

The recoil range distributions of products of the reaction of 98.7 MeV ^{15}N on ^{244}Pu are shown in Figures 41-42. Americium-242 and ^{246}Cf show the long-tailed distribution, typical of transfer, which extends over all ten foils. In contrast, the ^{252}Fm and ^{254}Fm activity is concentrated in the first few foils, with the bulk of the activity contained in three foils. These appear to be formed via CF, or possibly massive transfer, as the ranges are somewhat shorter than predicted for the CN. If it is assumed that these products are made by massive transfer of ^{14}C, without correcting for the (unknown) target thickness, the range of the product is predicted to be .257 mg Al/cm^2, somewhat longer than the observed peak range, which is in the second foil, i. e., between .1 and .2 mg Al/cm^2.

B. ANGULAR DISTRIBUTIONS

Angular distributions obtained in the method described in Section IV E are shown in figures 23-34. Except for ^{252}Fm produced in the bombardments of ^{245}Cm, these are all for projectile stripping reactions of one or two protons and some neutrons. Light particle data shows that the side peak of the angular distribution for such reactions is still visible, although the forward peaked component is comparable in importance. The angular distributions in Ref. 72 show that for stripping of four or more protons from ^{22}Ne to ^{232}Th the side peak is gone. In only one distribution, that of ^{252}Fm made in the highest energy OCm bombardment, OCm-III (Figure 32), can the case be made for the existence of a forward-peaked DIT component.

This can be interpreted as an effect of looking at the target residues. These products will be depleted by fission, to an extent dependent upon the excitation energy and the fission barriers, particularly at the higher l-values possible in transfer reactions (see Eqn. 24). The deep inelastic mechanism assumes that all the initial relative kinetic energy except the exit Coulomb repulsion energy is damped into excitation and so is accompanied by much higher excitation than the quasi-elastic mechanism. Therefore, it is reasonable that the QET mechanism is the predominant contributor to the formation of target-like residues.

The peaks of the derived angular distributions can be compared to the calculated classical grazing angles in Table I. It is seen

that the peaks are at larger angles than the grazing angle. One interpretation of this discrepancy is that the calculated Coulomb barrier is too high (Eqn. 4). If one takes for OCf the energy of OCf-I, the lowest energy bombardment, to be the Coulomb barrier, the grazing angles of the heavy fragment become, for OCf-IV, -III, and -II, respectively, 107, 89, and 59 degrees. These agree much better with the observed derived maxima. This ϵ_c corresponds to .86 of the calculated spherical Coulomb barrier. In the case of the ^{245}Cm experiments, we do not have a lower limit of interaction energy. Instead, the grazing angle of the heavy partner was taken to be 117.5, from the angular distribution of Cf-248 from OCm-III (Figure 34) and used in Eqn. 4 to obtain ϵ_c equal to 4.235, or .80 of the calculated spherical value. This value of ϵ_c yields values of θ_{gr} for OCm-II and -I that agree with the maxima in the angular distributions.

The hypothesis that the calculated Coulomb barrier is too high is supported by the observation[38] that if one uses the formula $R_C = r_o(A_P^{1/3} + A_T^{1/3})$ to calculate the barrier, the usual value of r_o = 1.41 fm is too low, and 1.51 fm gives better agreement with experimental barriers. This formula gives higher values of R_{int} than Eqn. 6, and thus a lower ϵ_C.

C. CROSS SECTIONS

The probability that a given nuclide will be formed in a reaction from a given primary progenitor is equal to the probability that the primary will be formed times the probability that it will decay via de-excitation to the particular residual nucleus under consideration. The cross-section for formation of that nuclide is found by summing the probabilities for all possible progenitors forming and decaying to that residue.

Some crude cross section predictions can be made for these reactions. The plot of $\log(\sigma)$ versus Q_{gg} for isotopes of projectile-like products of a given charge transfer from ^{16}O to ^{197}Au and ^{232}Th fall on a straight line:

$$\log_{10}\sigma = a(-Q_{gg}) + b \qquad (31)$$

The slope, a, was the same for the same ΔZ for both targets[80]. This slope and the intercept found by linear extrapolation with Z from Au and Th to Cm and Cf were used to estimate primary cross sections for the corresponding products. The excitation energy from the deep inelastic transfer component, E^*_{dit}, was taken to be the initial kinetic energy minus the Coulomb separation energy and that from the quasi-elastic component was taken to be equal to E^*_{opt} (Eqn. 18). All the excitation energy was assumed to go to the heavy fragment. The cross section of the residual nucleus was obtained separately for each of the two mechanisms.

The excitation energy distribution of every heavy primary product was taken to be centered at E^*_{opt} or E^*_{dit} with FWHM estimated to be 19 MeV, based upon light particle energy spectra from $^{40}Ar + ^{232}Th$[73]. Only neutron emission and fission were considered in the de-excitation. Evaporated neutrons were assumed to remove B_n + 3 MeV from E*. The probability of evaporating a neutron was calculated from the semiempirical relation of Sikkeland, et. al.[115]. The calculation was truncated when E* dropped below B_n. This assumption would be a source of inaccuracy, overestimating the final cross section for nuclei for which B_n exceeds the fission barrier. At E* between B_n and the fission barrier, the probability of fission can approach unity[102].

The total cross section would then be the sum of the DIT and QET contributions. The relative contribution to the primary yields from each would not be expected to be the same as those used in the fits of the residue recoil range distributions; even if these were not rather artificial parameters, they are appropriate for the surviving nuclei, not the primaries. The extracted angular distributions strongly suggest that the DIT contribution is heavily depleted relative to that from QET. Instead the measured cross sections were compared with estimates of relative QET/DIT survival probabilities to get an idea of the ratio of the $\sigma_{DIT}/\sigma_{QET}$. This ratio was around 10 for Fm isotopes from OCf-IV. Table XI lists estimated primary cross sections from Eqn. 31 and excitation energies and relative yields, from Eqn. 24, for QET and DIT Fm products of OCf-IV.

TABLE XI. Predicted cross sections in millibarns for ^{18}O (111.6 MeV) + $^{249}Cf \rightarrow Fm$

FERMIUM ISOTOPE	primary yield	excitation (MeV) DIT	QET	residual yield DIT	QET
248	.001037	35.1	-5.13	.00280	.00176
249	.04519	34.8	.45	.0243	.0389
250	.3007	34.5	2.34	.492	.423
251	4.721	34.2	5.95	3.68	4.19
252	21.55	33.9	10.1	30.1	38.1
253	193.2	33.5	15.5	12.6	55.2
254	83.41	33.1	14.9	7.77	37.1
255	93.76	32.7	16.1	1.19	17.6
256	.1810	32.3	4.76	.00322	.100

D. PREDICTION OF RECOIL CATCHER EFFICIENCY

Experiments that use the recoil catcher technique depend for their success upon the bulk of the product escaping the target. The analysis used for the recoil range distributions in this paper can also be used to predict the likelihood of a satisfactory recoil efficiency for a reaction.

In the following discussion all energies are in MeV, all velocities are in $(\text{MeV/amu})^{1/2}$, and the frame of reference is that of the center of mass unless otherwise specified.

Consider the reaction $^{249}Cf(^{18}O,^{14}C)^{253}Fm$. This is a reasonable channel for Fm production in OCf. First, let us look at QET, the mechanism that appears to be responsible for the main part of the heavy product of transfer in the bombardments reported here. The most probable range may be estimated using an exit channel separation energy equal to E^f_{opt} (Eqn. 18) and a center of mass angle equal to the grazing angle, calculated with Eqn. 4 and with $R_C = 1.51(A_P^{1/3} + A_T^{1/3})$. At any c.m.s. bombardment energy E^i, $E^f_{opt} = .755E^i$. For OCf-IV, $E^i_{lab} = 111.6$ MeV, and $\theta_{gr} = 101°$, so $E^f_{opt} = 78.4$ MeV and $\theta_H = 79°$. The velocity of the center of mass, v_{cm}, is .2372 $(\text{MeV/amu})^{1/2}$. With E^f, A_P, and A_T, fixed, conservation of energy and momentum determines the center of mass velocity of the heavy fragment V_T, to be .1813. From Eqn. 27 the axial lab frame velocity is .2214. This translates to a recoil range in aluminum of .32 mg/cm^2, which corresponds to the third foil in OCf-IV, allowing for the target

thickness. Figure 5 shows that the most probable range is in the third foil. The RECOILS run that fit the recoil range distributions also predicted that less that .05 of the heavy products would stay in the target.

At a higher energy energy, 139.3 MeV, v_{cm} = .2752, E^f_{opt} = 106.6, θ_{gr} = 50.7°, and θ_H = 129.3. This gives an axial velocity in the lab frame of .1421, which corresponds to a recoil range of less than .132 mg Al/cm^2, less than .1 mg Al/cm^2 longer than half the target thickness. This is a dangerously low range, particularly in view of the breadth of the range distributions. The higher v_{cm} does not compensate for the increasing θ_H.

If the mechanism at this higher energy is MT, an α particle at the beam velocity fuses with the target, imparting a velocity to the composite system sufficient to give it a range of about .12 mg Al/cm^2. The MT range distribution, however, is expected to be narrow and concentrated around this value.

The DIT product would have a lower center of mass separation energy, opposing its center of mass recoil angle of 0°. If the separation energy is equal to the exit channel E_C, again calculated with r_o = 1.51, the heavy fragment center of mass velocity would be .1345, its lab velocity would be .1407, and its axial range would be .13 mg Al/cm^2. This is a lower limit; depending upon the slope of the angular distribution, a significant fraction of the product nuclei will have a longer range. It would also be carrying up to 96 MeV of excitation and would be unlikely to survive de-excitation.

CONCLUSIONS

This study illustrates that recoil range distribution shapes can be used to distinguish between complete fusion, massive transfer, and quasi-elastic plus deep inelastic transfer. The angular distributions derived from the recoil range distributions assuming QET/DIT mechanism imply that while the DIT contribution is expected to be significant, it is strongly depleted relative to the QET contribution. This is confirmed by de-excitation estimates compared with measured cross sections. Massive transfer does not appear to be an important process in these low-energy bombardments.

Further study of angular and energy distributions of both light and heavy products of LHI + actinide is necessary to confirm or refute these conclusions. The yields of these products is high enough that recoil ranges at several angles could be measured, which is the only technique presently available to measure $d\sigma/d(\text{omega})$ and lab energy of such heavy products. Extrapolation of theory and experiment with non-fissile targets is not sufficient. Also, it would be interesting to know at what energy massive transfer becomes important for these systems. A simple recoil range distribution measurement would be the first step in such an investigation.

This work was supported by the Director, Office of Energy Research, Division of Nuclear Physics of the Office of High Energy and Nuclear Physics of the U. S. Department of Energy under Contract DE-AC03-76SF00098.

REFERENCES

1. Hoffman, D. C., Diana Lee, Albert Ghiorso, M. J. Nurmia, Kjell Aleklett, and Matti Leino. Fission properties of the 1.5-s spontaneous fission activity produced in bombardment of ^{248}Cm with ^{18}O. Phys. Rev. C 24 (1981) 495-499.

2. Lee, Diana, Hans von Gunten, Barbara Jacak, Matti Nurmia, Yuan-fang Liu, Cheng Luo, Glenn T. Seaborg, and Darleane Hoffman. Production of heavy actinides from interactions of ^{16}O, ^{18}O, ^{20}Ne, and ^{22}Ne with ^{248}Cm. Phys. Rev. C 25 (1982) 286-292.

3. Lee, Diana, Kenton Moody, Matti Nurmia, Glenn T. Seaborg, Hans R. von Gunten, and Darleane Hoffman. Excitation functions for production of heavy actinides from interactions of ^{18}O with ^{248}Cm and ^{249}Cf. To be published.

4. Wolf, K. L., J. P. Unik, J. R. Huizenga, J. Birkelund, H. Freiesleben, and V. E. Viola. Study of strongly damped collisions in the reaction of 600-MeV ^{84}Kr on a ^{209}Bi target. Phys. Rev. Lett. 33 (1974) 1105-1112.

5. Bass, Reiner. Nuclear Reactions with Heavy Ions. Springer-Verlag (New York 1980).

6. Bass, R. Fusion of heavy nuclei in a classical model. Nucl. Phys. A231 (1974) 45-63.

7. Swiatecki, W. J. The dynamics of nuclear coalescence or reseparation. Phys. Scripta. 24 (1981) 113-122.

8. Wong, C. Y. Fusion threshold energy in heavy-ion reactions. Phys. Lett. 42B (1972) 186-190.

9. Colombani, P., J. C. Jacmart, N. Poffe, M. Riou, C. Stephan, and J. Tys. Elastic scattering of ^{84}Kr by heavy nuclei. Phys. Lett. 42B (1972) 197-200.

10. Gauvin, H., Y. Le Beyec, M. Lefort, and C. Deprun. Complete fusion nuclear reactions induced by krypton ions. Effective threshold and minimum distance of approach for the reactions ^{119}Cd + ^{84}Kr and ^{72}Ge + ^{84}Kr. Phys. Rev. Lett. 28 (1972) 697-699.

11. Ghiorso, A., T. Sikkeland, J. R. Walton, and G. T. Seaborg. Element 102. Phys. Rev. Lett. 1 (1958) 18-20.

12. Ghiorso, A., T. Sikkeland, A. E. Larsh, and R. M. Latimer. New element, Lawrencium, atomic number 103. Phys. Rev. Lett. 6 (1961) 473-475.

13. Ghiorso, A., M. Nurmia, J. Harris, K. Eskola, and P. Eskola. Positive identification of two alpha-particle-emitting isotopes of element 104. Phys. Rev. Lett. 22 (1969) 1317-1320.

14. Ghiorso, A., M. Nurmia, K. Eskola, J. Harris, and P. Eskola. New element Hahnium, atomic number 105. Phys. Rev. Lett. 24 (1970) 1498-1503.

15. Ghiorso, A., J. M. Nitschke, J. R. Alonso, C. T. Alonso, M. Nurmia, G. T. Seaborg, E. K. Hulet, and R. W. Lougheed. Element 106. Phys. Rev. Lett. 33 (1974) 1490-1493.

16. Munzenberg, G., S. Hofmann, F. P. Hessberger, W. Reisdorf, K. H. Schmidt, J. H. R. Schneider, p. Armbruster, C. C. Sahm, and B. Thuma. Identification of element 107 by α correlation chains. Z. Phys. A300 (1981) 107-108.

17. Ghiorso, A. and G. T. Seaborg. Private communication (1982).

18. Swiatecki, W. J. The dynamics of the fusion of two nuclei. LBL-12642 (1981).

19. Cohen, S., F. Plasil, and W. J. Swiatecki. Equilibrium configurations of rotating charged or gravitating liquid masses with surface tension. II. Annals of Physics 82 (1974) 557-596.

20. Sikkeland, Torbjorn. Evidence for the production of compound nuclei with atomic number 110. Phys. Lett. 27B (1968) 277-279.

21. Kratz, J. V., J. O. Liljenzin, A. E. Norris, and G. T. Seaborg. Charge and mass distributions in the reaction of ^{40}Ar ions with ^{238}U. Phys. Rev. C 13 (1976) 2347-2365.

22. Reus, U., A. M. Habbestad Watzig, R. A. Esterlund, P. Patzelt, and I. S. Grant. Mass-yield distributions in the reaction of ^{56}Fe ions with ^{238}U. Phys. Rev. Lett. 39 (1977) 171-174.

23. Kratz, J. V., A. E. Norris, G. T. Seaborg. Mass-yield distributions in the reaction of ^{84}Kr ions with ^{238}U. Phys. Rev. Lett. 33 (1974) 502-505.

24. Otto, R. J., M. M. Fowler, D. Lee, and G. T. Seaborg. Mass yield distributions in the reaction of ^{136}Xe ions with ^{238}U. Phys. Rev. Lett. 36 (1976) 135-138.

25. Kowalski, L., J. C. Jodogne, and J. M. Miller. Complete-fusion in heavy-ion reactions. Phys. Rev. 169 (1968) 894-898.

26. Lefort, Marc. Recent results on the fusion reactions between very heavy ions and nuclei. J. Phys. A: Math., Nucl., Gen. 7 (1974) 107-119.

27. Peter, J., C. Ngo, and B. Tamain. Complete fusion and quasi-fission reactions induced by ^{84}Kr ions on heavy targets. Nucl. Phys. A250 (1975) 351-363.

28. Binder, Irwin. A radiochemical study of the reactions of heavy ions with gold. Ph.D. Thesis. LBL Report-6526 (1977).

29. Lefort, M. and Ch. Ngo. Deep inelastic reactions with heavy ions. A probe for nuclear macroscopic studies. Ch. II. Ann. Phys. 3 (1978)

30. Williams. Kim. Radiochemical studies of neutron deficient actinide isotopes. Ph.D. Thesis. LBL Report-7714 (1978).

31. Hahn, R. L., P. F. Dittner, K. S. Toth, and O. L. Keller. Transfer and compound-nucleus reactions that lead to the nuclei ^{245}Cf and ^{244}Cf: Interactions of ^{12}C with ^{239}Pu and ^{238}U. Phys. Rev. C 10 (1974) 1889-1903.

32. Thomas, K. Transfer products from the reactions of heavy ions with heavy nuclei. Ph. D. Thesis. LBL-9886 (1979).

33. Schadel, M., J. V. Kratz, H. Ahrens, W. Bruchle, G. Franz, H. Gaggeler, I. Warnecke, G. Wirth, G. Herrmann, N. Trautmann, and M. Weis. Isotope distributions in the reaction of ^{238}U with ^{238}U. Phys. Rev. Lett. 41 (1978) 469-472.

34. Schadel, M., W. Bruchle, H. Gaggeler, J. V. Kratz, K. Summerer, G. Wirth, G. Herrmann, R. Stakemann, G. Tittel, N. Trautmann, J. M. Nitschke, E. K. Hulet, R. W. Lougheed, R. L. Hahn, and R. L. Ferguson. Actinide production in collisions of ^{238}U with ^{248}Cm. Phys. Rev. Lett. 48 (1982) 852-855.

35. Moody, K. J. Private communication (1981).

36. Moller, Peter and J. Rayford Nix. Nuclear mass formula with a Yukawa plus exponential macroscopic model and a folded Yukawa single particle potential. LA-UR-80-1996 (1980).

37. McFarland, R. M. and M. Schulman. Unpublished data (1980).

38. Schadel, M., R. W. Lougheed, J. H. Landrum, J. F. Wild, R. J. Dougan, A. D. Hoover, E. K. Hulet, G. R. Bethune, A. Ghiorso, M. J. Nurmia, L. P. Somerville, K. J. Moody, and G. T. Seaborg. Distributions of heavy actinide products from reactions of ^{18}O, ^{22}Ne, and ^{136}Xe with ^{254}Es: Observance of a new spontaneous fission isotope and possible assignment. (1982) To be published.

39. Artukh, A. G., G. F. Gridnev, V. L. Mikheev, and V. V. Volkov. New isotopes ^{22}O, ^{20}N and ^{18}C produced in transfer reactions with heavy ions. Nucl. Phys. A137 (1969) 348-352.

40. Wilczynski, J. Calculations of the critical angular momentum in the entrance reaction channel. Nucl Phys. A216 (1973) 386-394.

41. Galin, J., D. Guerreau, M. Lefort, and X. Tarrago. Limitation to complete fusion between two complex nuclei. Phys. Rev. C 9 (1974) 1018-1024.

42. Glas, D. and U. Mosel. Limitations on complete fusion during heavy ion collisions. Phys. Rev. C 10 (1974) 2620-2622.

43. Bass, R. Threshold and angular momentum limit in the complete fusion of heavy ions. Phys. Lett. 47B (1973) 139-142.

44. Zebelman, A. M. and J. M. Miller. Role of angular momentum in complete fusion reactions: $^{11}B + ^{159}Tb$, $^{12}C + ^{158}Gd$, $^{16}O + ^{154}Sm$. Phys. Rev. Lett. 30 (1973) 27-30.

45. Glas, D. and U. Mosel. On the critical distance in fusion reactions. Nucl. Phys. A237 (1975) 429-440.

46. Blocki, J., J. Randrup, W. J. Swiatecki, and C. F. Tsang. Proximity forces. Annals of Physics 105 (1977) 427-462.

47. Bass, R. Nucleus-nucleus potential deduced from experimental fusion cross sections. Phys. Rev. Lett. 39 (1977) 265-268.

48. Karnaukhov, V. A., G. M. Ter-Akop'yan, and V. I. Khalizev. Two-neutron capture reaction in the interaction between ^{14}N and nuclei of some elements. Sov. Phys. JETP 9 (1959) 748-750.

49. Pinajian, J. J. The exchange transfer reaction $^{27}Al(^{14}N,^{27}Mg)^{14}O$. Nucl. Phys. 17 (1960) 44-53.

50. Kaufman, Richard and Richard Wolfgang. Complex nucleon transfer reactions of heavy ions. Phys. Rev. Lett. 3 (1959) 232-234.

51. Reynolds, H. L., D. W. Scott, and A. Zucker. Nuclear reactions produced by nitrogen on boron and oxygen. Phys. Rev. 102 (1956) 237-241.

52. Beydon, J., R. Chaminade, M. Crut, H. Faraggi, J. Olkowsky, and A. Papineau. Etude de la transmutation du cuivre par l'azote et l'oxygene. Nucl. Phys. 2 (1956/57) 593-618.

53. Breit, G. and M. E. Ebel. Nucleon tunneling in $^{14}N + ^{14}N$ reactions. Phys. Rev. 103 (1956) 679-701.

54. Breit, G. Transfer of nuclear particles. Phys. Rev. 102 (1956) 549-556.

55. Chackett, K. F., J. H. Fremlin, and D. Walker. Nuclear reactions produced by nitrogen and oxygen ions. Phil. Mag. 45 (1954) 173-189.

56. Chackett, G. A., K. F. Chackett, and J. H. Fremlin. The distribution of the products of heavy ion reactions with aluminum. Phil. Mag. 46 (1955) 1.

57. Breit, G. and M. E. Ebel. Nucleon transfer and virtual coulomb excitation. Phys. Rev. 104 (1956) 1030-1046.

58. Kaufmann, R. and R. Wolfgang. Nuclear transfer reactions in grazing collisions of heavy ions. Phys. Rev. 121 (January 1961) 192-205.

59. Sugihara, T. T. Massive transfer in heavy-ion reactions: possible applications in nuclear structure studies. Phys. Scripta. 24 (1981) 108-112.

60. Thompson, S. G., L. G. Moretto, R. C. Jared, R. P. Babinet, J. Galin, M. M. Fowler, R. C. Gatti, and J. B. Hunter. Macroscopic aspects of heavy ion reactions. Phys. Scripta 10A (1974) 36-40.

61. Moretto, L. G., and R. Schmitt. Experimental evidence and physical implications of the time evolution along the mass asymmetry mode in heavy ion reactions. J. de Phys. (Paris) C5 (1976) 109-140.

62. Galin, Joel. Experimental situation in deep inelastic reactions with respect to the rapidly relaxed modes. J. de Phys. (Paris) C5 (1976) 83-105.

63. Britt, Harold C. and Arthur Quinton. Alpha particles and protons emitted in the bombardment of ^{197}Au and ^{209}Bi by ^{12}C, ^{14}N, and ^{16}O projectiles. Phys. Rev. 124 (1961) 877-887.

64. Galin, J., B. Gatty, D. Guerreau, C. Rousset, U. C. Schlotthauer-Voos, and X. Tarrago. Study of charged particles emitted from ^{117}Te compound nuclei. II. Comparison between ^{40}Ar + ^{77}Se and ^{14}N + ^{103}Rh reactions and determination of critical angular momenta. Phys. Rev C 9 (1974) 1126-1137.

65. Inamura, T., M. Ishihara, T. Fukuda, T. Shimoda, and H. Hiruta. Gamma-rays from an incomplete fusion reaction induced by 95 MeV ^{14}N. Phys. Lett. 68B (1977) 51-54.

66. Zolnowski, D. R., H. Yamada, S. E. Cala, A. C. Kahler, and T. T. Sugihara. Evidence for "massive transfer" in heavy-ion reactions on rare-earth targets. Phys. Rev. Lett. 41 (1978) 92-95.

67. Udagawa, T. and T. Tamura. Breakup-fusion description of massive transfer reactions with emission of fast light particles. Phys. Rev. Lett. 45 (1980) 1311-1314.

68. Barker, J. H., J. R. Beene, M. L. Halbert, D. C. Hensley, M. Jaaskelainen, D. G. Sarantites, and R. Woodward. Direct evidence for a narrow window at high angular momentum in incomplete-fusion reactions. Phys. Rev. Lett. 45 (1980) 424-427.

69. Geoffroy, K. A., D. G. Sarantites, M. L. Halbert, D. C. Hensley, R. A. Dayras, and J. H. Barker. Angular momentum transfer in incomplete-fusion reactions. Phys. Rev. Lett. 43 (1979) 1303-1306.

70. Nitschke, J. M. Synthesis and investigation of neutron-rich transuranium isotopes. LBL Report-11712 (1980).

71. Galin, J., D. Guerreau, M. Lefort, J. Peter, and X. Tarrago. Mechanism of single-nucleon and multi-nucleon transfer reactions in grazing collisions of heavy ions on silver. Nucl. Phys. A159 (1970) 461-480.

72. Artyukh, A. G., J. Wilczynski, V. V. Volkov, G. F. Gridnev, and V. L. Mikheev. Direct reactions in the interaction of ^{22}Ne with ^{232}Th. Yad. Fiz. 17 (1973) 1126-1133 (transl. Sov. J. Nucl. Phys. 17 586-589).

73. Artukh, A. G., G. F. Gridnev, V. L. Mikheev, V. V. Volkov, and J. Wilczynski. Transfer reactions in the interaction of ^{40}Ar with ^{232}Th. Nucl. Phys. A215 (1973) 91-108.

74. Jacmart, J. C., P. Colombani, H. Doubre, N. Frascaria, N. Poffe, M. Riou, J. C. Roynette, and C. Stephan. Isotope distribution of transfer products in the ^{40}Ar + ^{232}Th interaction at 295 MeV. Nucl. Phys A242 (1975) 175-188.

75. Oganesyan, Yu. Ts., Yu. E. Penionzhkevich, and A. O. Shamsutdinov. Regularities of isotope production in many-nucleus transfer reactions. Yad. Fiz. 14 (1971) 54-64 (Transl.: Sov. J. Nucl. Phys. 14 (1972) 31-36).

76. Gardes, D., R. Bimbot, J. Maison, M. F. Rivet, A. Fleury, F. Hubert, and Y. Llabador. Angular distributions and ranges of heavy products from quasi-elastic transfer reactions induced by heavy ions in ^{209}Bi. Phys. Rev. C 21 (1980) 2447-2466.

77. Hubert, F., H. Delagrange, and A. Fleury. Transfer reactions of B with Ta. Nucl. Phys. A228 (1974) 415-431.

78. Colombani, P., N. Frascaria, J. C. Jacmart, M. Riou, C. Stephan, H. Doubre, N. Poffe, and J. C. Roynette. Deep inelastic fragment production in the ^{40}Ca on ^{40}Ca interaction at 278 MeV. Phys. Lett. 55B (1975) 45-48.

79. Strudler, P. M., I. L. Preiss, and Richard Wolfgang. Systematics of some nucleon transfer reactions of complex nuclei. Phys. Rev. 154 (1967) 1126-1135.

80. Artukh, A. G., V. V. Avideichikov, J. Ero, G. F. Gridnev, V. L. Mikheev, V. V. Volkov, and J. Wilczynski. On some regularities in multinucleon transfer reactions with heavy ions. Nucl. Phys. A160 (1970) 511-516.

81. Bondorf, J. P., F. Dickmann, D. H. E. Gross, and P. J. Siemens. Statistical aspects of heavy ion reactions. J. Phys. (Paris) Colloq. 32 (1971) C6-145.

82. Toeppfer, Christian. Q-value dependence of multinucleon transfer reactions. Phys. Rev. Lett. 27 (1971) 872-874.

83. Lee, S. Y. and P. Braun-Munzinger. Statistical aspects of isotope production in heavy ion reactions. Phys. Rev. C 24 (1981) 1343-1345.

84. Karp, J. S., S. G. Steadman, S. B. Gazes, R. Ledoux, and F. Videbaek. Statistical behavior of nucleon transfer to highly excited states in heavy ion collisions. Phys. Rev. C 25 (1982) 1838-1864.

85. Kammuri, T. and K. Matsuoka. Gross properties of heavy-ion transfer reactions (I) Formulation. Nucl. Phys. A366 (1981) 171-188.

86. Matsuoka, K. and T. Kammuri. Gross properties of heavy-ion transfer reactions (II) Comparison with experiment. Nucl. Phys. A376 (1982) 341-366.

87. Brink, D. M. Kinematical effects in heavy-ion reactions. Phys. Lett. 40B (1972) 37-40.

88. Pougheon, F. and P. Roussel. Origin of j and Q dependence in heavy-ion transfer reactions. Phys. Rev. Lett. 30 (1973) 1223-1227.

89. Broglia, Ricardo and Aage Winther. Transfer reactions between heavy ions. Nucl. Phys. A182 (1972) 112-130.

90. Wilczynski, J., K. Wilczynska, J. van Driel, S. Gonggrijp, D. C. J. M. Hageman, R. V. F. Janssens, J. Lukasiak, and R. H. Siemssen. Incomplete-fusion reactions in the $^{14}N + ^{159}Tb$ system and a "Sum-Rule Model" for fusion and incomplete-fusion reactions. Phys. Rev. Lett. 45 (1980), 606-609.

91. Siwek-Wilczynska, K., E. H. du Marchie van Voorthuysen, J. van Popta, R. H. Siemssen, and J. Wilczynski. Incomplete fusion in $^{12}C + ^{160}Gd$ collisions interpreted in terms of a generalized concept of critical angular momentum. Phys. Rev. Lett. 42 (1979) 1599-1602.

92. Moody, K. J. Private communication. (1982).

93. Artukh, A. G., G. F. Gridnev, V. L. Mikheev, V. V. Volkov, and J. Wilczynski. Multinucleon transfer reactions in the $^{232}Th + ^{22}Ne$ system. Nucl. Phys. A211 (1973) 299-309.

94. Toepffer, C. Quasi-classical treatment of multinucleon transfer reactions. Z. Phys. 253 (1972) 78-88.

95. Bohr, Niels and John Archibald Wheeler. The mechanism of nuclear fission. Phys. Rev. 56 (1939) 426-450.

96. Sikkeland, Torbjorn. Fission-excitation functions in interactions of ^{12}C, ^{16}O, and ^{22}Ne with various targets. Phys. Rev. 135 (1964) 669-677.

97. Vandenbosch, Robert and John R. Huizenga. Nuclear Fission. Academic Press (New York 1973).

98. Sikkeland, Torbjorn. Synthesis of nuclei in the region of Z = 126 and N = 184. Ark. Fys. 36 (1967) 539-552.

99. Back, B. B., Ole Hansen, H. C. Britt, and J. D. Garrett. Fission of doubly even actinide nuclei induced by direct reactions. Phys. Rev. C 9 (1974) 1924-1947.

100. Back, B. B., H. C. Britt, Ole Hansen, B. Leroux, and J. D. Garrett. Fission of odd-A and doubly odd actinide nuclei induced by direct reactions. Phys. Rev. C 10 (1974) 1948-1965.

101. Britt, H. C., E. Cheifetz, D. C. Hoffman, J. B. Wilhelmy, R. J. Dupzyk, and R. W. Lougheed. Fission barriers for ^{255}Es, ^{256}Es, and ^{255}Fm. Phys. Rev. C 21 (1980) 761-763.

102. Gavron, A., H. C. Britt, E. Konecny, J. Weber, and J. B. Wilhelmy. Γ_n/Γ_f for actinide nuclei using (^3He,df) and (^3He,tf) reactions. Phys. Rev. C 13 (1976) 2374-2384.

103. Gavron, A., H. C. Britt, P. D. Goldstone, R. Schoenmackers, J. Weber, and J. B. Wilhelmy. $\Gamma_n/\ \Gamma_f$ in heavy actinides. Phys. Rev. C 15 (1977) 2238-2240.

104. Britt, H. C., A. Gavron, P. D. Goldstone, R. Schoenmackers, J. Weber, and J. B. Wilhelmy. Yet more complexity in fission: barriers for nuclei with N = 150-154. Phys. Rev. Lett. 40 (1978) 1010-1013.

105. Delagrange, Hugues, Alain Fleury, and John M. Alexander. Fission-evaporation competition in Pu isotopes of mass 235-239. Phys. Rev. C 17 (1978) 1706-1720.

106. Northcliffe, L. C. and R. F. Schilling. Range and stopping power tables for heavy ions. Nuclear Data Tables A7 (1970) 233-463.

107. Moody, K. J. Private communication. (1980)

108. Table of Isotopes, 7th ed. Edited by C. M. Lederer and V. S. Shirley. Wiley (New York 1978).

109. Armbruster, P. Private communication (1982).

110. Winsberg, Lester and John Alexander. Ranges and range straggling of ^{149}Tb, At, and Po. Phys. Rev. 121 (1961) 518-528.

111. Amana, G. E. and J. Ficks. Private communication (1982).

112. Lindhard, J., M. Scharff, and H. E. Schiott. Range concepts and heavy ion ranges. Danske. Videnskab. Selskab. Mat. Fys. Medd. 33 (1963).

113. Otto, R. J., G. T. Seaborg, and M. M. Fowler. Recoil range distributions of heavy mass products in deep inelastic reactions with gold and uranium targets. Phys. Rev. C 17 (1978) 1071-1085.

114. For example, if one assumes the reaction channel to be $^{239}Pu(^{12}C, ^{4}He)^{247}Cf$, takes the center of mass separation energy to be E^{f}_{opt} (Eqn. 18), and calculates θ_{gr} with Eqn. 4 and $R_C = 1.51(A_P^{1/3} + A_T^{1/3})$, the lab grazing angle for the 75.5 MeV bombardment in Ref. 31 is predicted to be 16.5°. This is in good agreement with the reported maximum in the angular distribution of 10-15°.

115. Sikkeland, Torbjorn, Albert Ghiorso, and Matti J. Nurmia. Analysis of excitation functions in Cm(C,xn)No reactions. Phys. Rev. 172 (1968) 1232-1238.

FIGURE CAPTIONS

Figure 1. Plot of reaction probability versus entrance channel orbital angular momentum l, schematically illustrating mechanism regimes.

Figure 2. Target and recoil catcher foil chamber.

Figure 3. Schematic of bombardment arrangement.

Figure 4. Representative alpha spectrum from ^{18}O (111.6 MeV) + ^{249}Cf. $E_{(ALPHA)}$ = channel (.02) + 5 MeV.

Figure 5a-e. Recoil range distribution of Fm isotopes from ^{18}O (111.6 MeV) + ^{249}Cf, or OCf-IV.

Figure 6a-d. Recoil range distribution of Es isotopes from OCf-IV.

Figure 7a-d. Recoil range distribution of Cf isotopes from OCf-IV.

Figure 8a-e. Recoil range distribution of Fm isotopes from ^{18}O (99.8 MeV) + ^{249}Cf, or OCf-III.

Figure 9a-d. Recoil range distribution of Es isotopes from OCf-III.

Figure 10a-d. Recoil range distribution of Cf isotopes from OCf-III.

Figure 11a-e. Recoil range distribution of Fm isotopes from ^{18}O (89.2 MeV) + ^{249}Cf, or OCf-II.

Figure 12a,b. Recoil range distribution of Es isotopes from OCf-II.

Figure 13a-d. Recoil range distribution of Cf isotopes from OCf-II.

Figure 29. Fm angular distributions for ^{18}O (111.6 MeV) + ^{249}Cf, or OCf-IV, extracted from recoil range data (see text).

Figure 30. Es angular distributions for OCf-IV extracted from recoil range data.

Figure 31. Cf angular distributions for OCf-IV extracted from recoil range data.

Figure 32. Fm angular distributions for ^{18}O (99.8 MeV) + ^{249}Cf, or OCf-III, extracted from recoil range data.

Figure 33. Es angular distributions for OCf-III extracted from recoil range data.

Figure 34. Cf angular distributions for OCf-III extracted from recoil range data.

Figure 35. Fm angular distributions for ^{18}O (99.8 MeV) + ^{249}Cf, or OCf-II, extracted from recoil range data.

Figure 36. Es angular distributions for OCf-II extracted from recoil range data.

Figure 37. Cf angular distributions for OCf-II extracted from recoil range data.

Figure 38. ^{252}Fm extracted angular distributions for ^{18}O (111.6, 99.6, and 93. MeV) + ^{245}Cm, or OCm-III, -II, -I, respectively.

Figure 39. ^{248}Cf extracted angular distributions for OCm-III, -II, -I.

Figure 40. ^{246}Cf extracted angular distributions for OCm-III, -II, -I.

Figure 41a. Recoil range distribution for ^{242}Am from ^{15}N (98.7 MeV) + ^{244}Pu.

Figure 41b. Recoil range distribution for ^{246}Cf from ^{15}N (98.7 MeV) + ^{244}Pu.

Figure 42a. Recoil range distribution for ^{252}Fm from ^{15}N (98.7 MeV) + ^{244}Pu.

Figure 42b. Recoil range distribution for ^{254}Fm from ^{15}N (98.7 MeV) + ^{244}Pu.

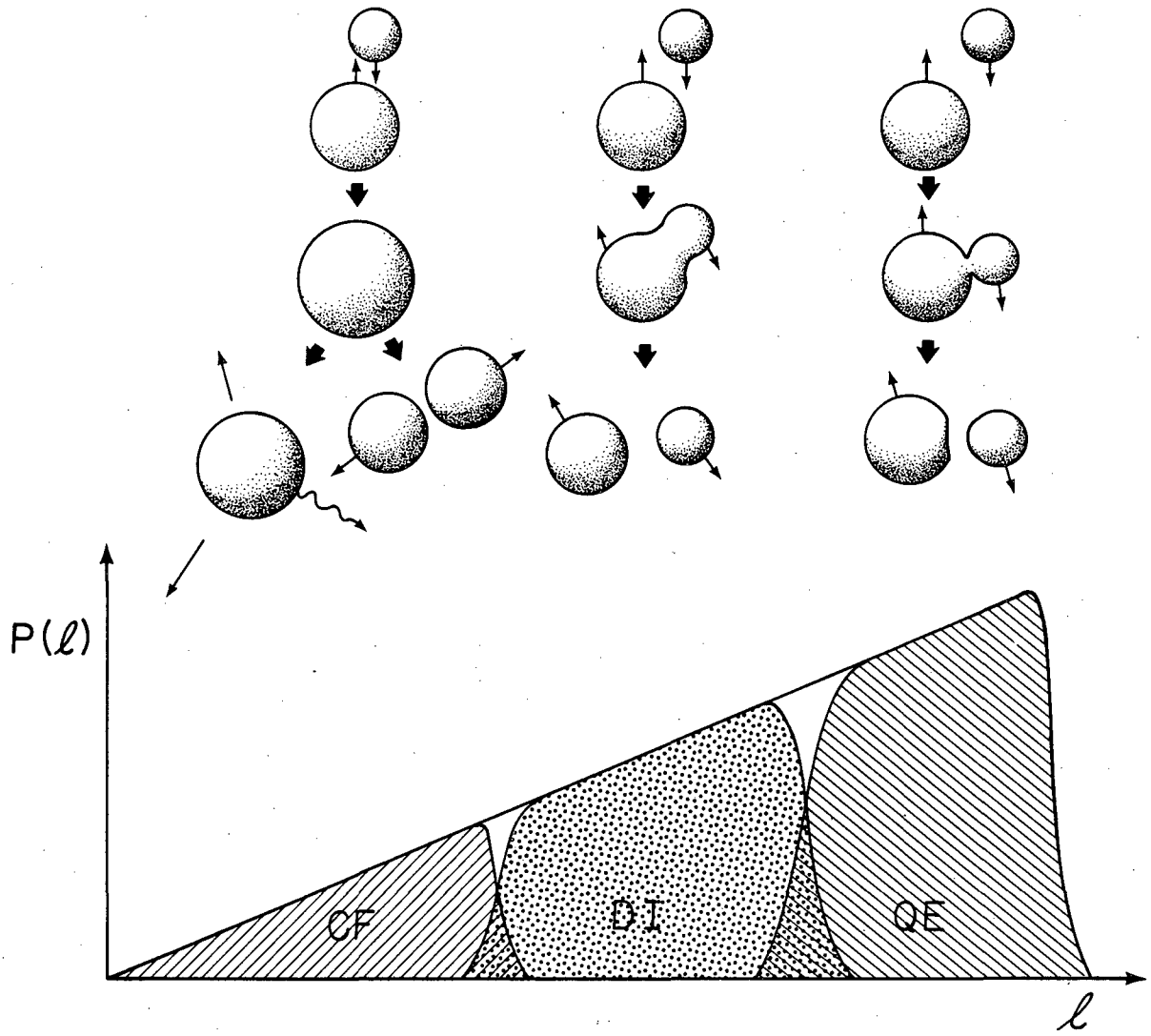

XBL 784-2482

Fig. 1

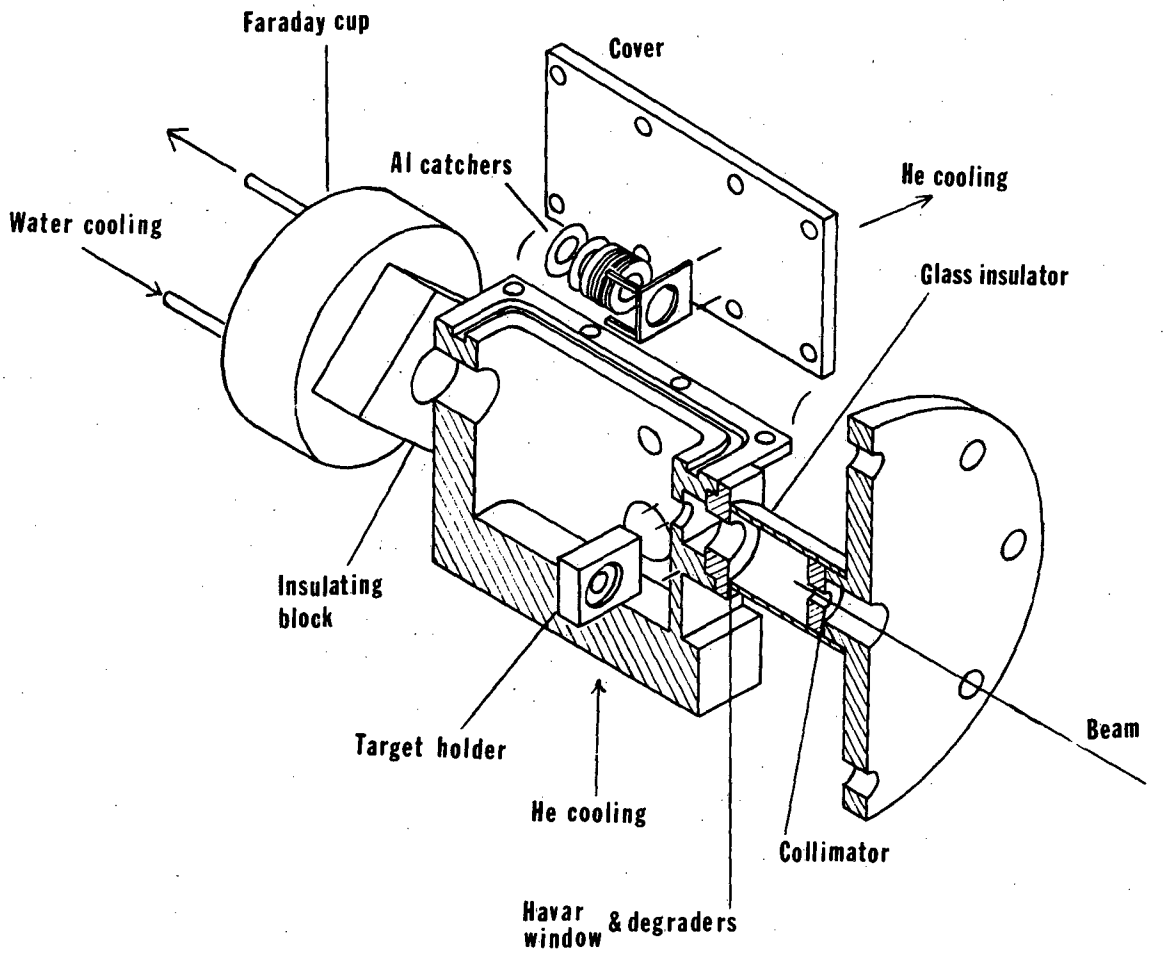
Faraday cup
Cover
Al catchers
He cooling
Water cooling
Glass insulator
Insulating block
Target holder
Beam
He cooling
Collimator
Havar window
& degraders
XBL 828-9568

Fig. 2

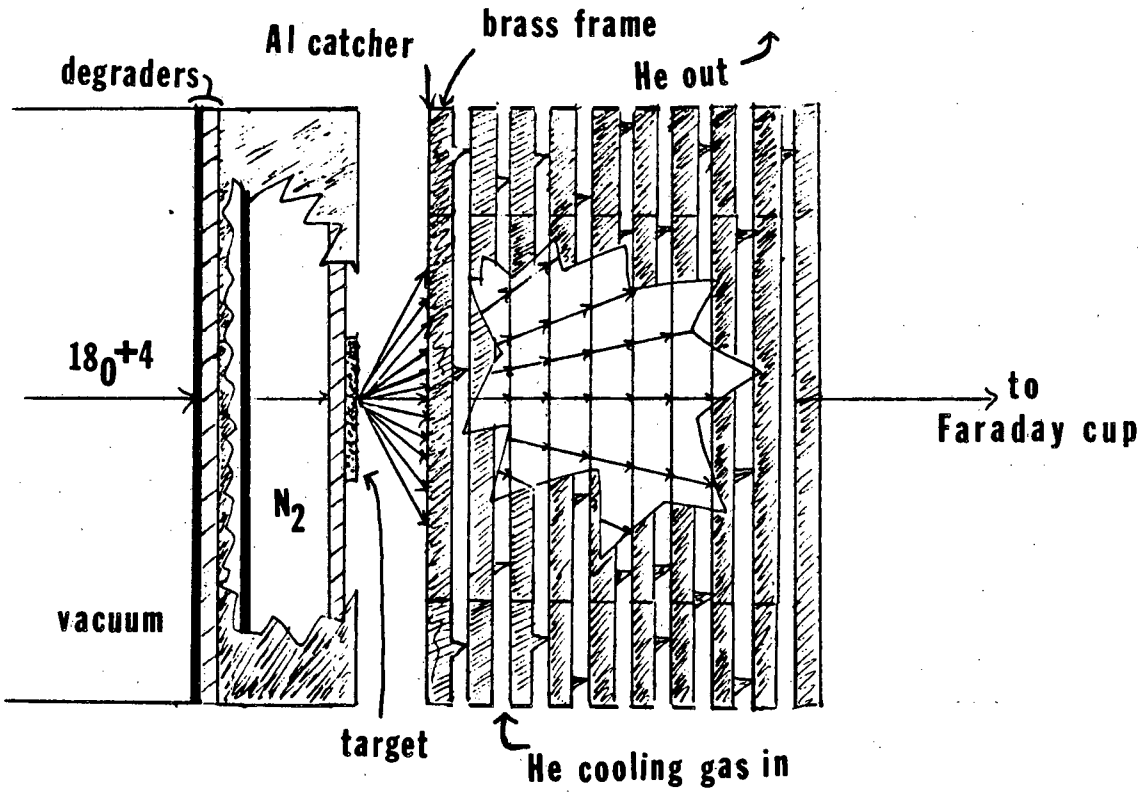
degraders
Al catcher
brass frame
He out
18_0+4
N_2
vacuum
to
Faraday cup
target
He cooling gas in
XBL 828-9549

Fig. 3

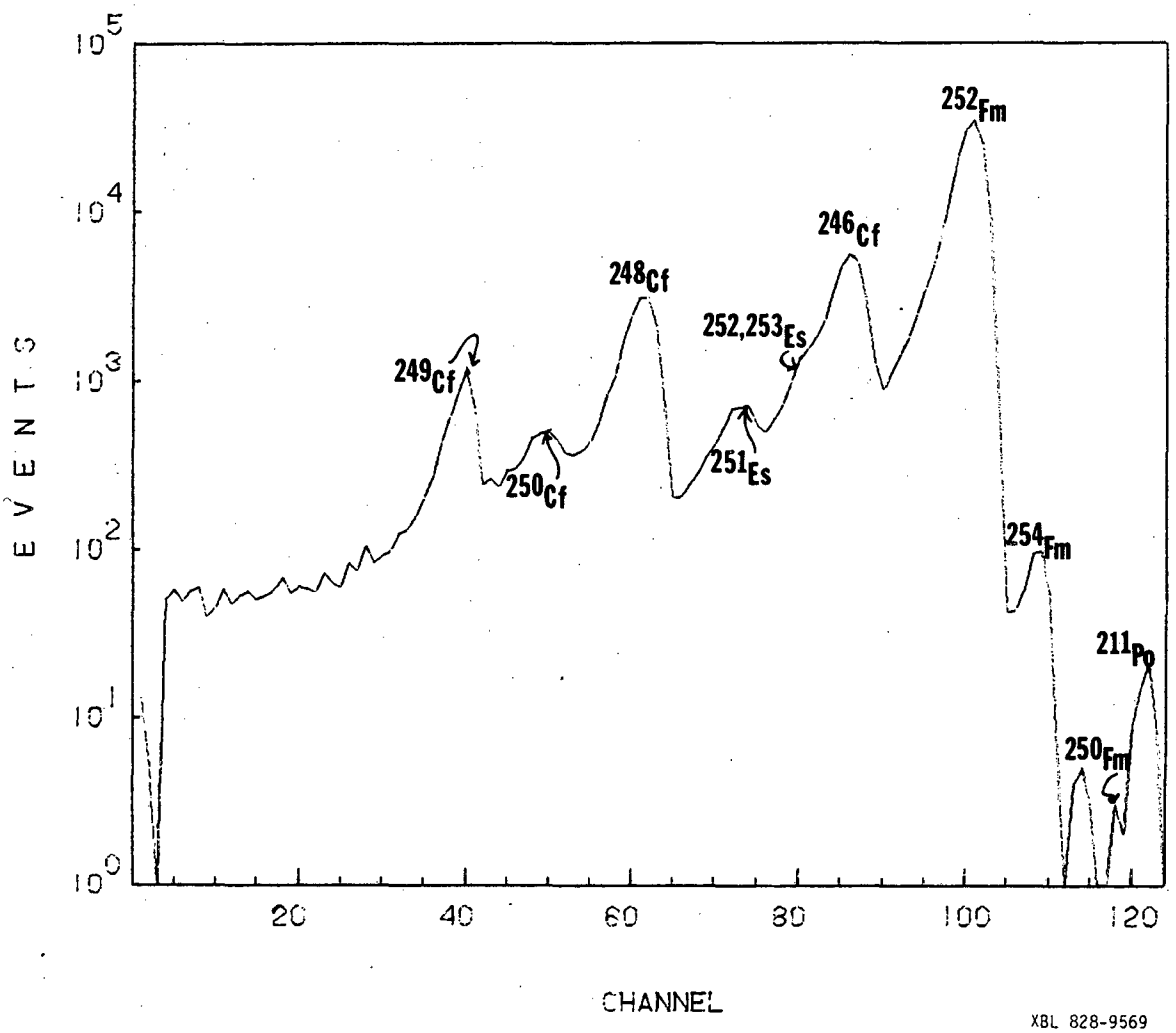
EVENTS
CHANNEL
10^5
10^4
10^3
10^2
10^1
10^0
20
40
60
80
100
120
^{249}Cf
^{250}Cf
^{248}Cf
^{252,253}Es
^{251}Es
^{246}Cf
^{252}Fm
^{254}Fm
^{211}Po
^{250}Fm
XBL 828-9569

Fig. 4

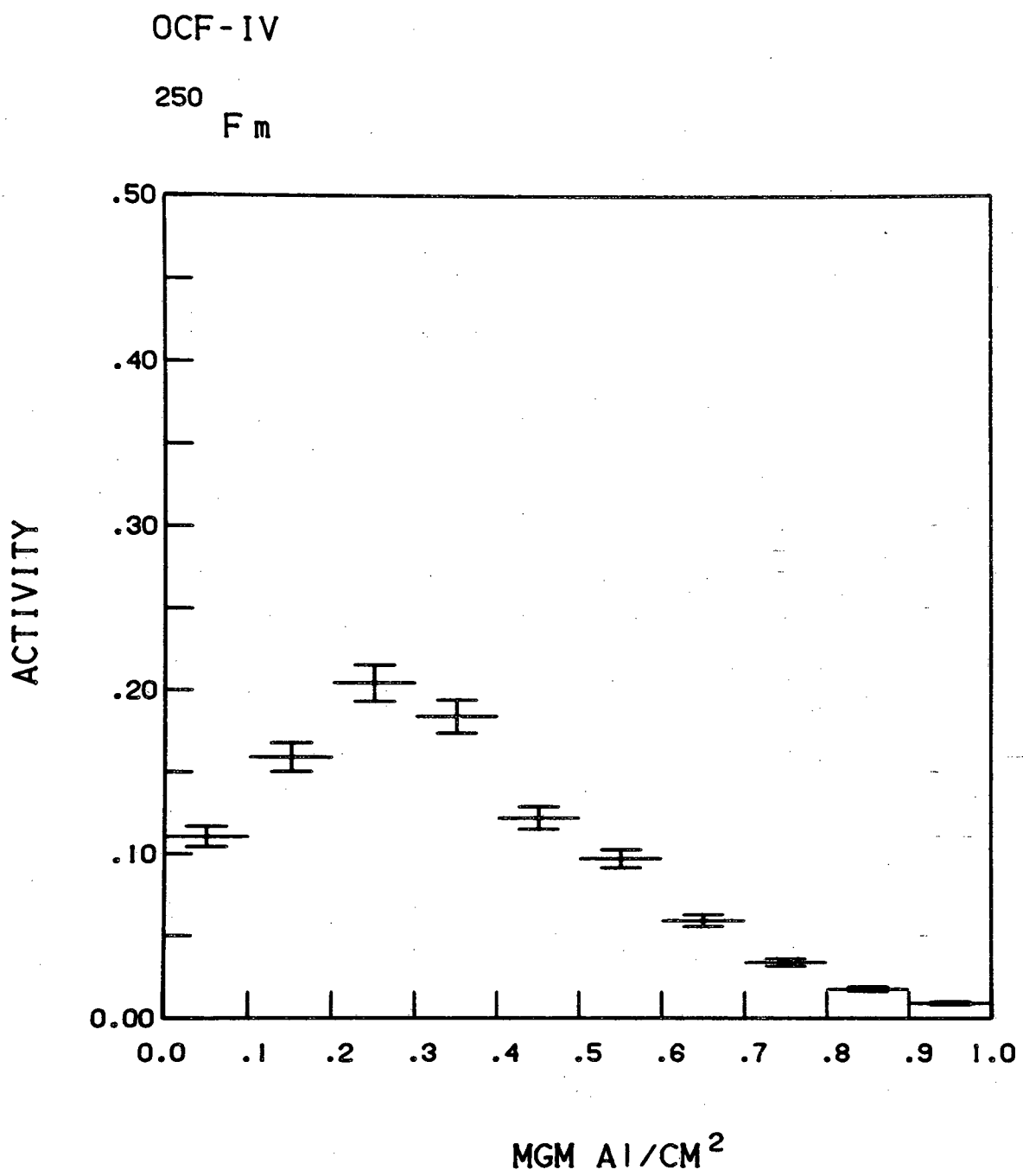
OCF-IV
250
Fm
.50
.40
.30
.20
.10
0.00
ACTIVITY
0.0
.1
.2
.3
.4
.5
.6
.7
.8
.9
1.0
MGM Al/CM2
XBL 823-9503

Fig. 5a

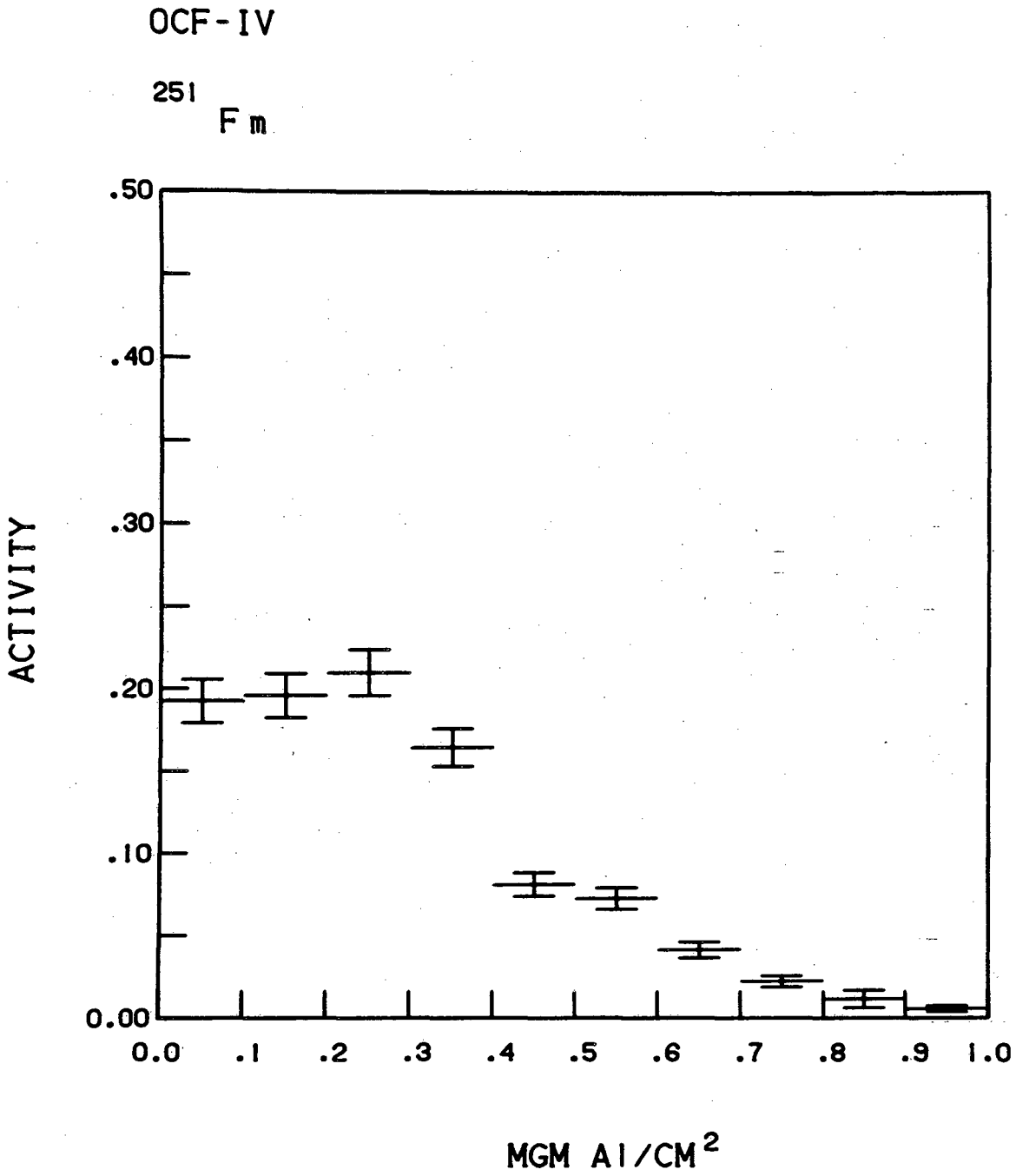
OCF-IV
251
Fm
.50
.40
.30
.20
.10
0.00
ACTIVITY
0.0
.1
.2
.3
.4
.5
.6
.7
.8
.9
1.0
MGM Al/CM 2
XBL 823-9509

Fig. 5b

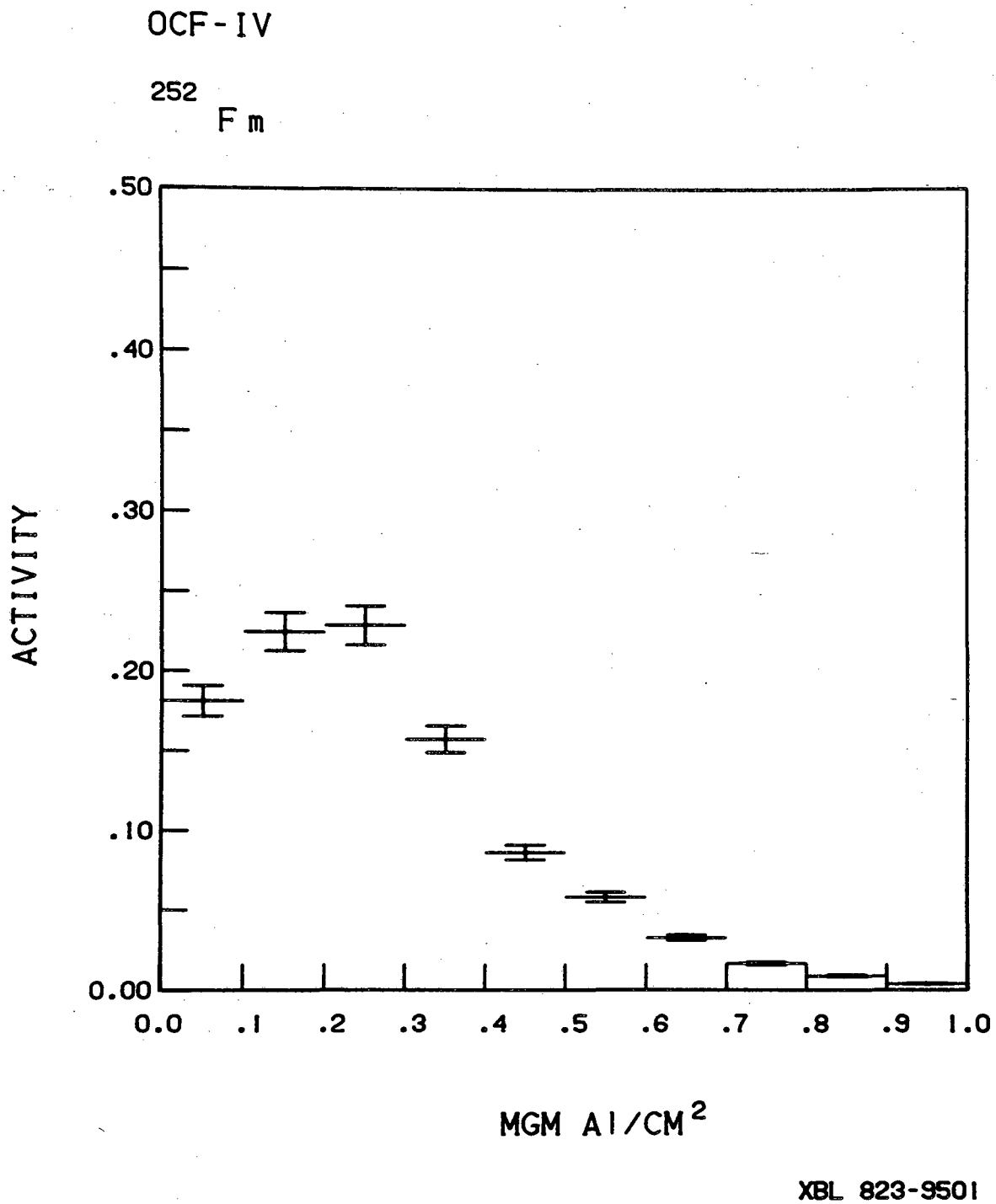
OCF-IV
252
Fm
.50
.40
.30
.20
.10
0.00
ACTIVITY
0.0
.1
.2
.3
.4
.5
.6
.7
.8
.9
1.0
MGM Al/CM 2
XBL 823-9501

Fig. 5c

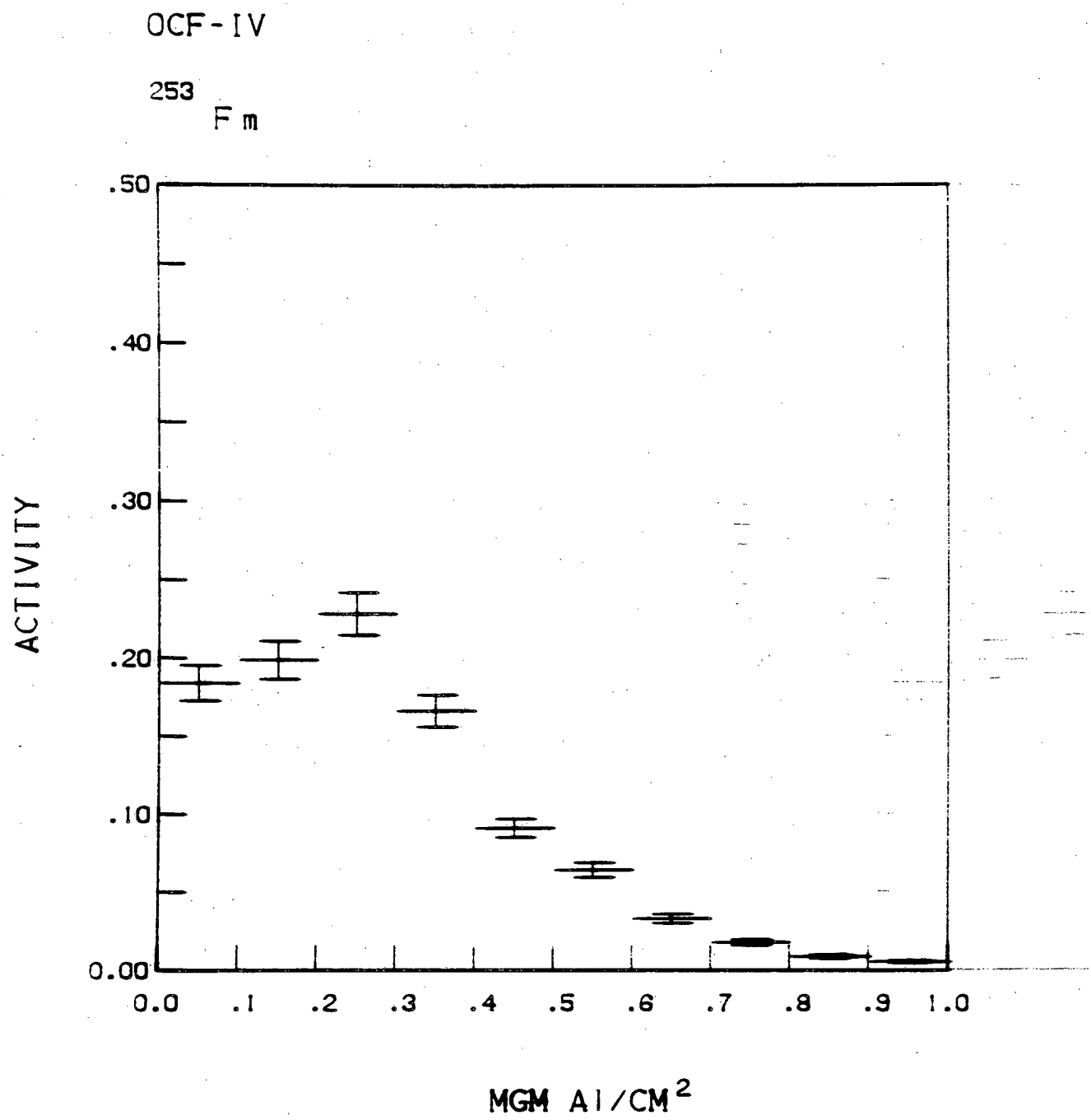
OCF-IV
253
Fm
.50
.40
.30
.20
.10
0.00
ACTIVITY
0.0
.1
.2
.3
.4
.5
.6
.7
.8
.9
1.0
MGM Al/CM 2
XBL 823-9502

Fig. 5d

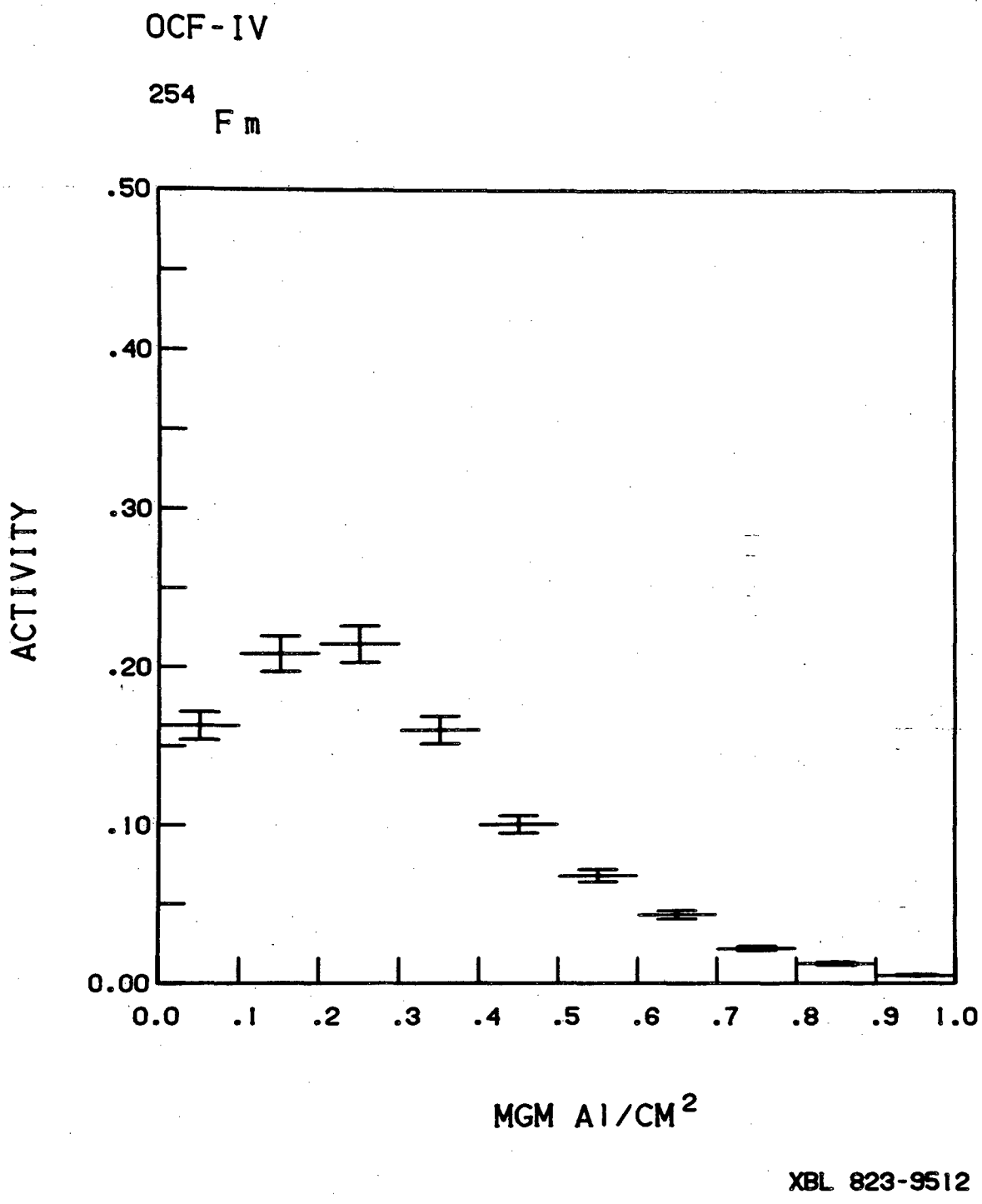
OCF-IV
254
Fm
.50
.40
.30
.20
.10
0.00
ACTIVITY
0.0
.1
.2
.3
.4
.5
.6
.7
.8
.9
1.0
MGM Al/CM2
XBL 823-9512

Fig. 5e

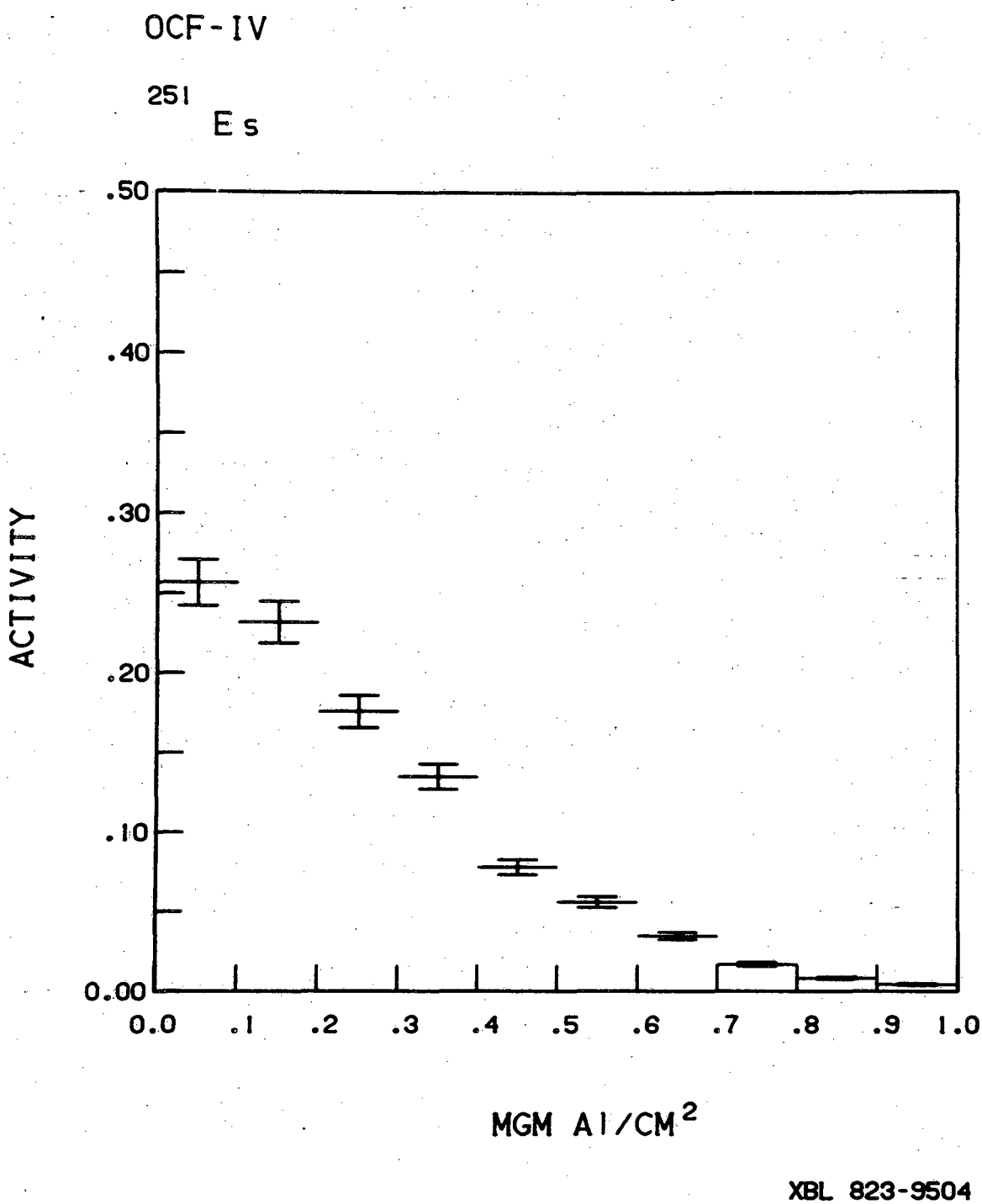
OCF-IV
251
Es
.50
.40
.30
.20
.10
0.00
ACTIVITY
0.0
.1
.2
.3
.4
.5
.6
.7
.8
.9
1.0
MGM Al/CM 2
XBL 823-9504

Fig. 6a

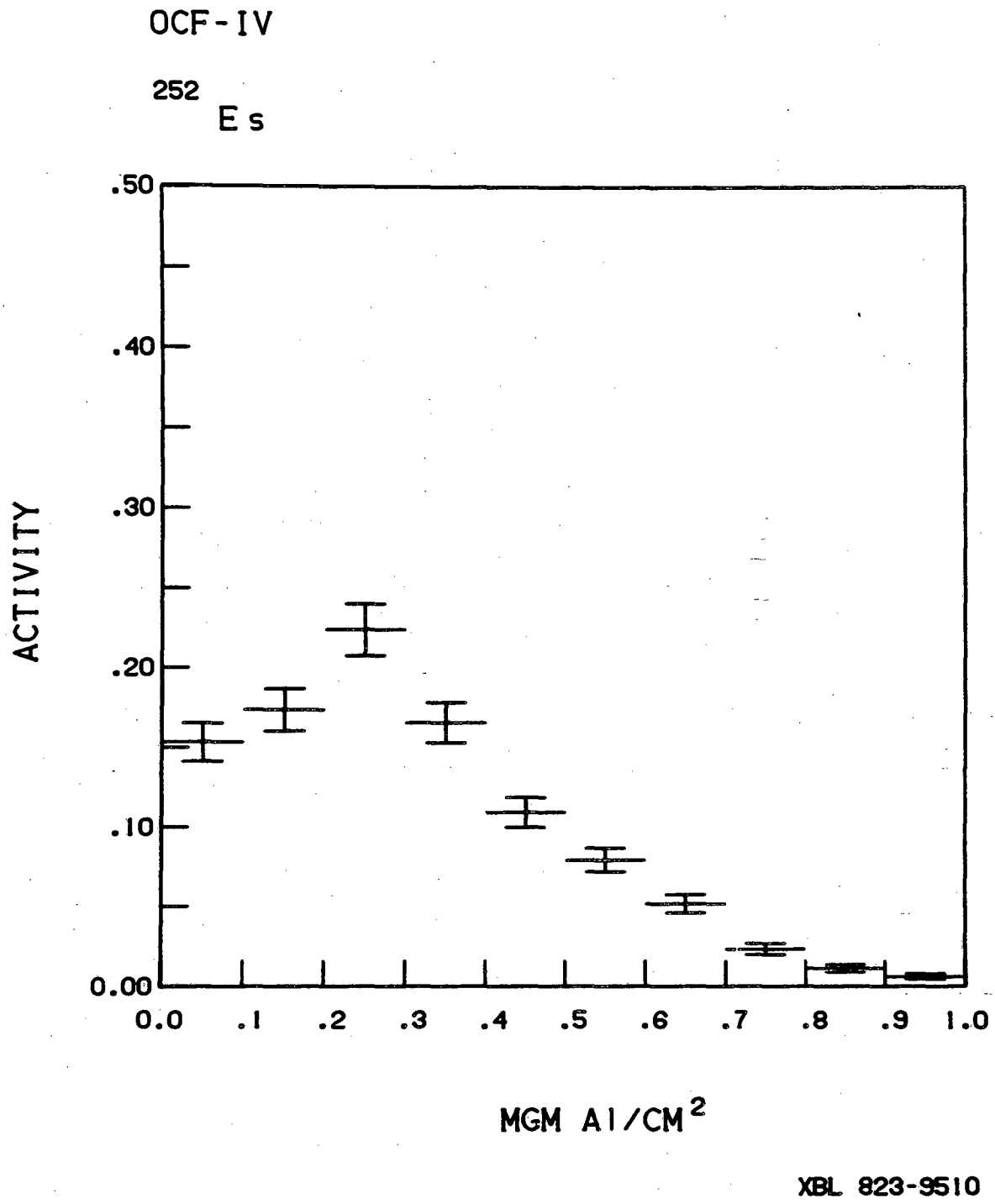
OCF-IV
252
Es
.50
.40
.30
.20
.10
0.00
ACTIVITY
0.0
.1
.2
.3
.4
.5
.6
.7
.8
.9
1.0
MGM Al/CM 2
XBL 823-9510

Fig. 6b

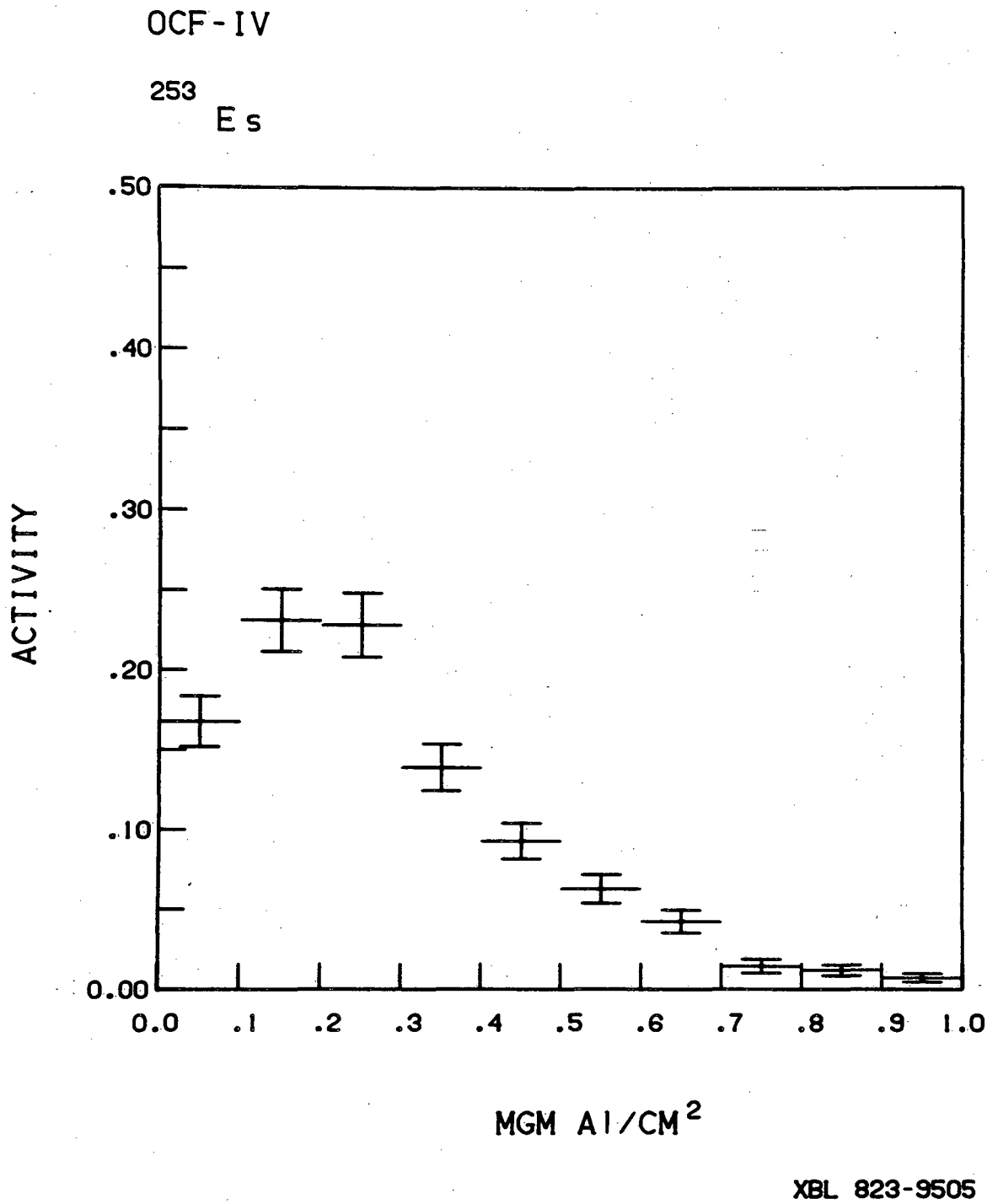
OCF-IV
253
Es
.50
.40
.30
.20
.10
0.00
ACTIVITY
0.0
.1
.2
.3
.4
.5
.6
.7
.8
.9
1.0
MGM Al/CM 2
XBL 823-9505

Fig. 6c

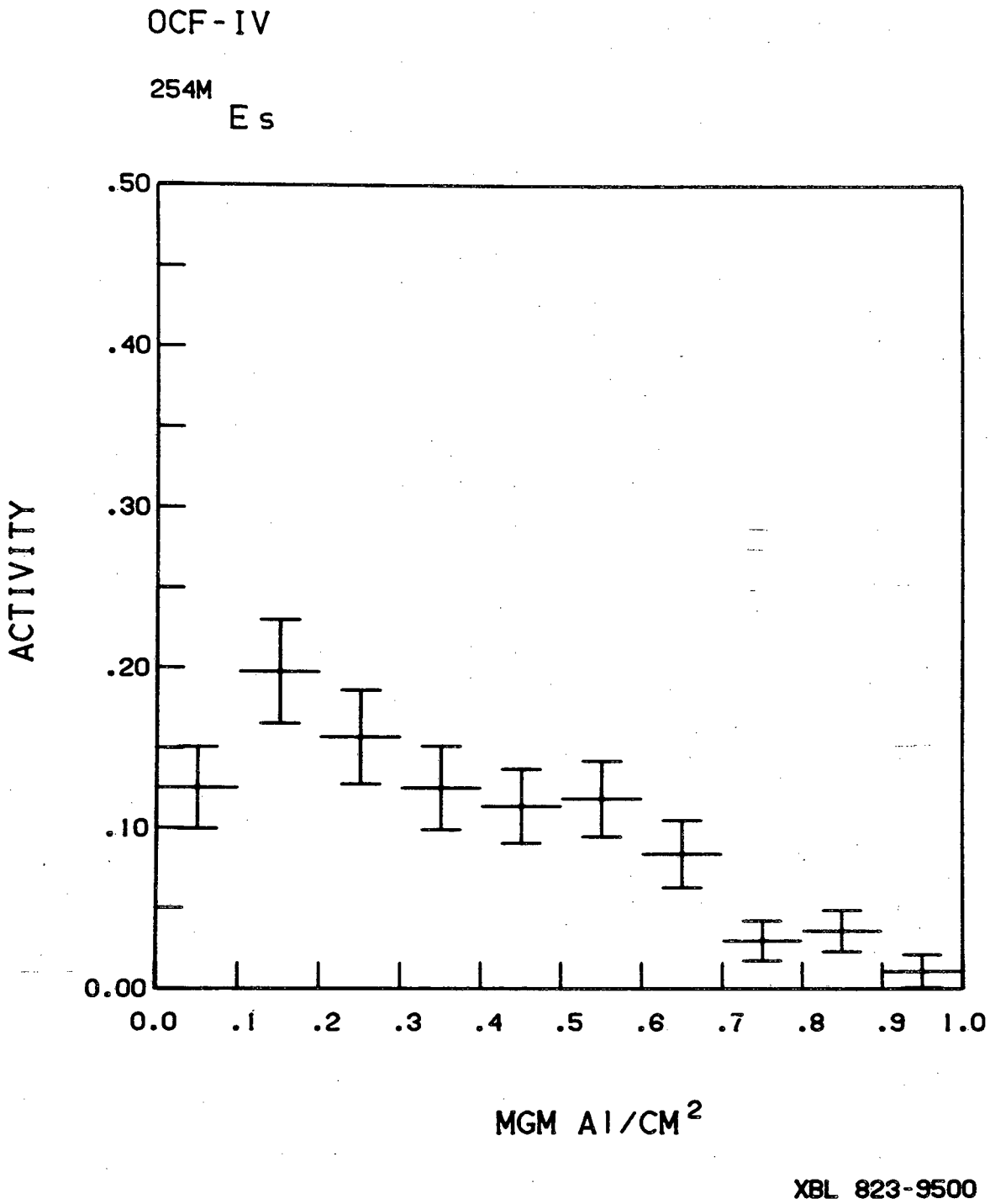
OCF - IV
254M
E s
.50
.40
.30
.20
.10
0.00
ACTIVITY
0.0
.1
.2
.3
.4
.5
.6
.7
.8
.9
1.0
MGM Al/CM 2
XBL 823-9500

Fig. 6d

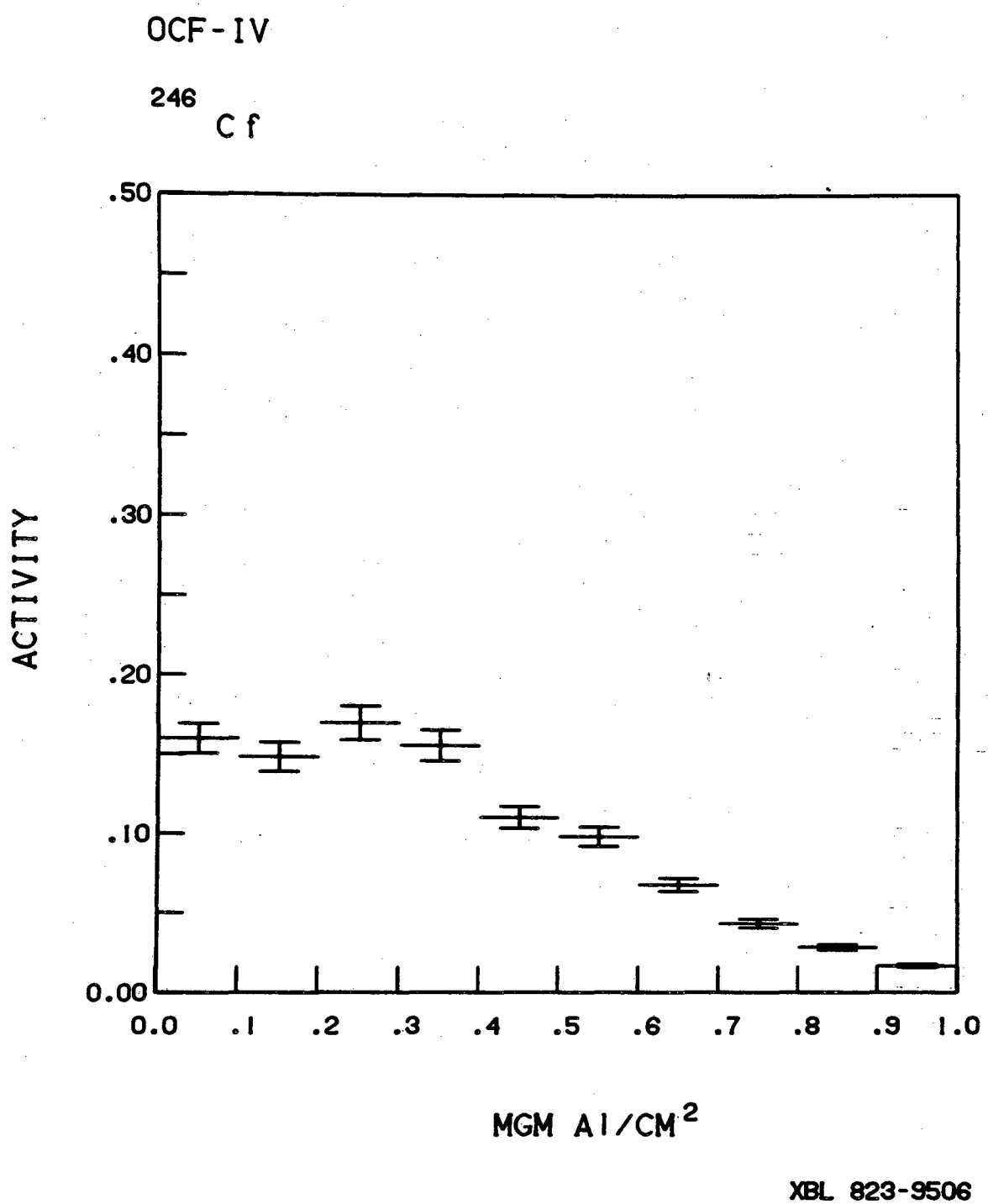
OCF-IV
246 Cf
ACTIVITY
.50
.40
.30
.20
.10
0.00
0.0
.1
.2
.3
.4
.5
.6
.7
.8
.9
1.0
MGM Al/CM2
XBL 823-9506

Fig. 7a

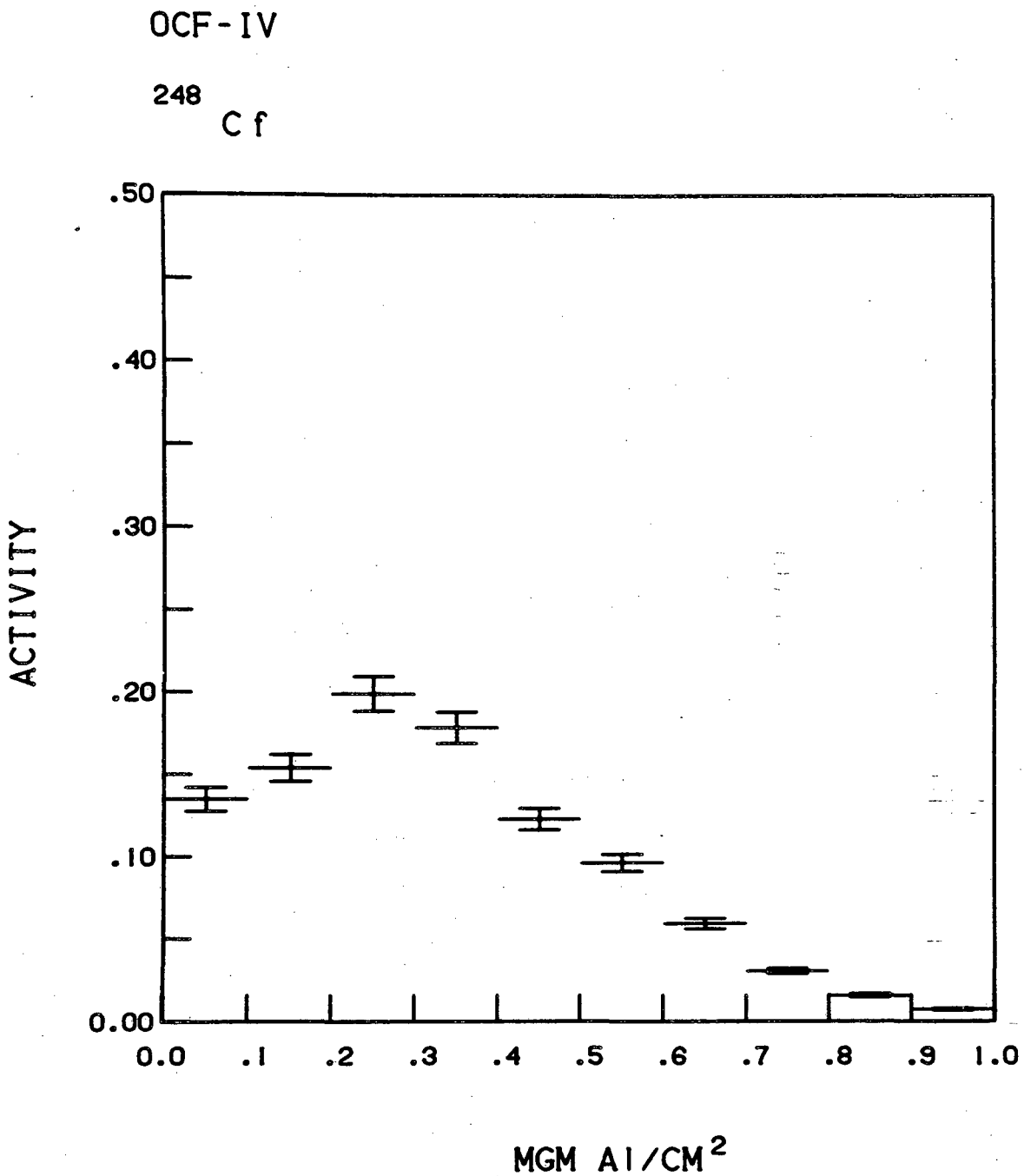
OCF-IV
248 Cf
.50
.40
.30
.20
.10
0.00
ACTIVITY
0.0
.1
.2
.3
.4
.5
.6
.7
.8
.9
1.0
MGM Al/CM 2
XBL 823-9507

Fig. 7b

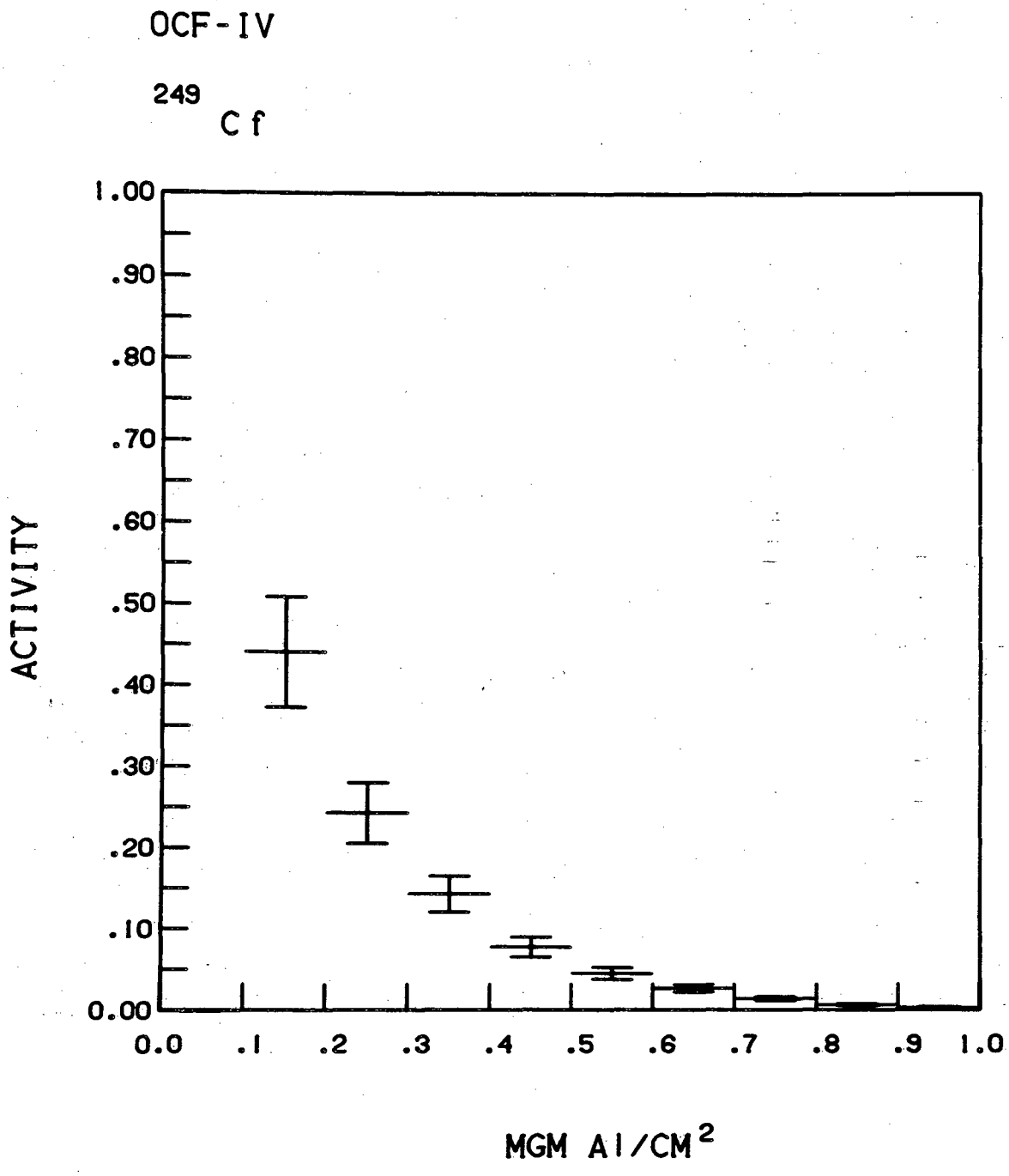
OCF-IV
249 Cf
ACTIVITY
1.00
.90
.80
.70
.60
.50
.40
.30
.20
.10
0.00
0.0
.1
.2
.3
.4
.5
.6
.7
.8
.9
1.0
MGM Al/CM 2
XBL 823-9508

Fig. 7c

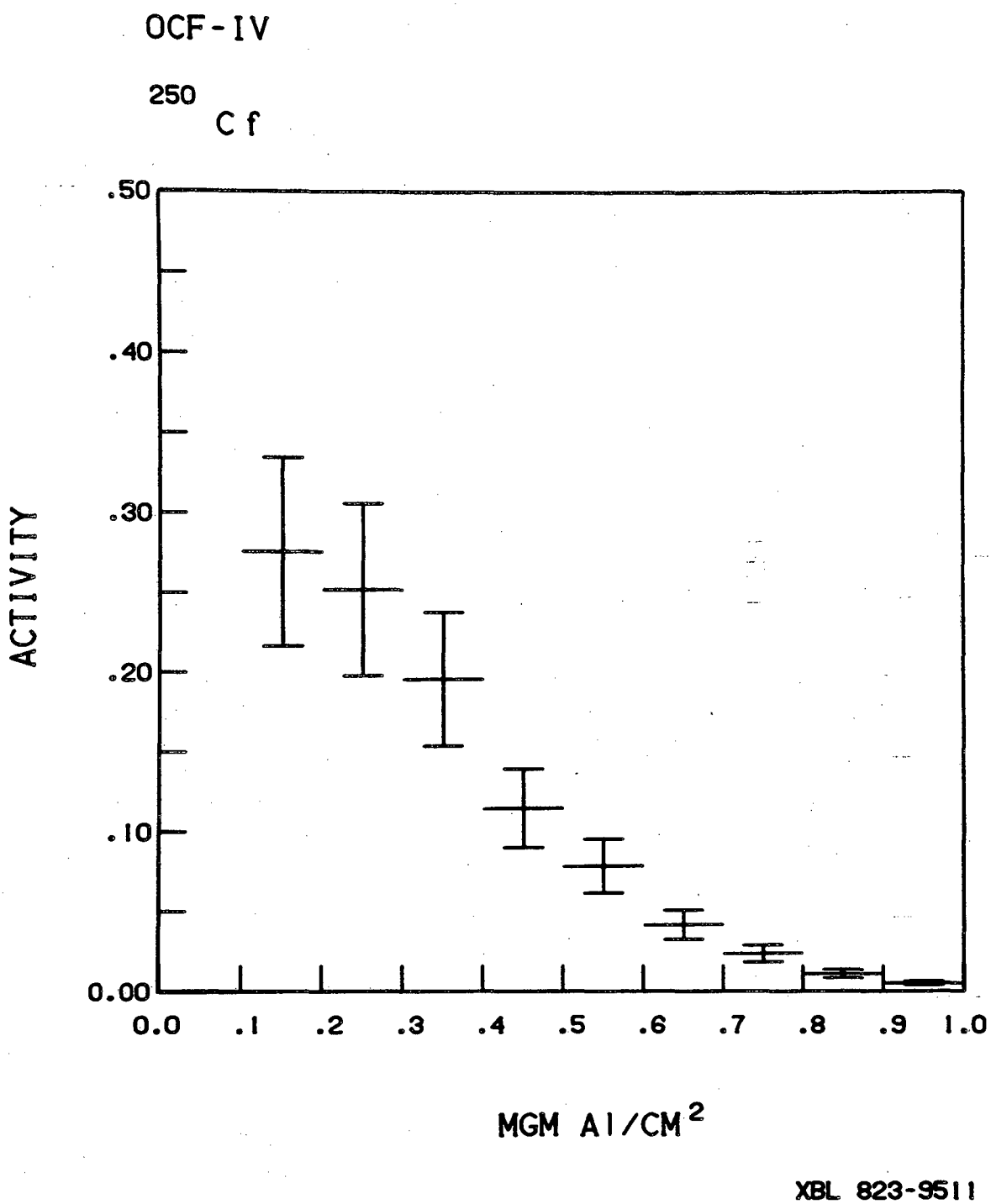
OCF-IV
250 Cf
ACTIVITY
.50
.40
.30
.20
.10
0.00
0.0
.1
.2
.3
.4
.5
.6
.7
.8
.9
1.0
MGM Al/CM 2
XBL 823-9511

Fig. 7d

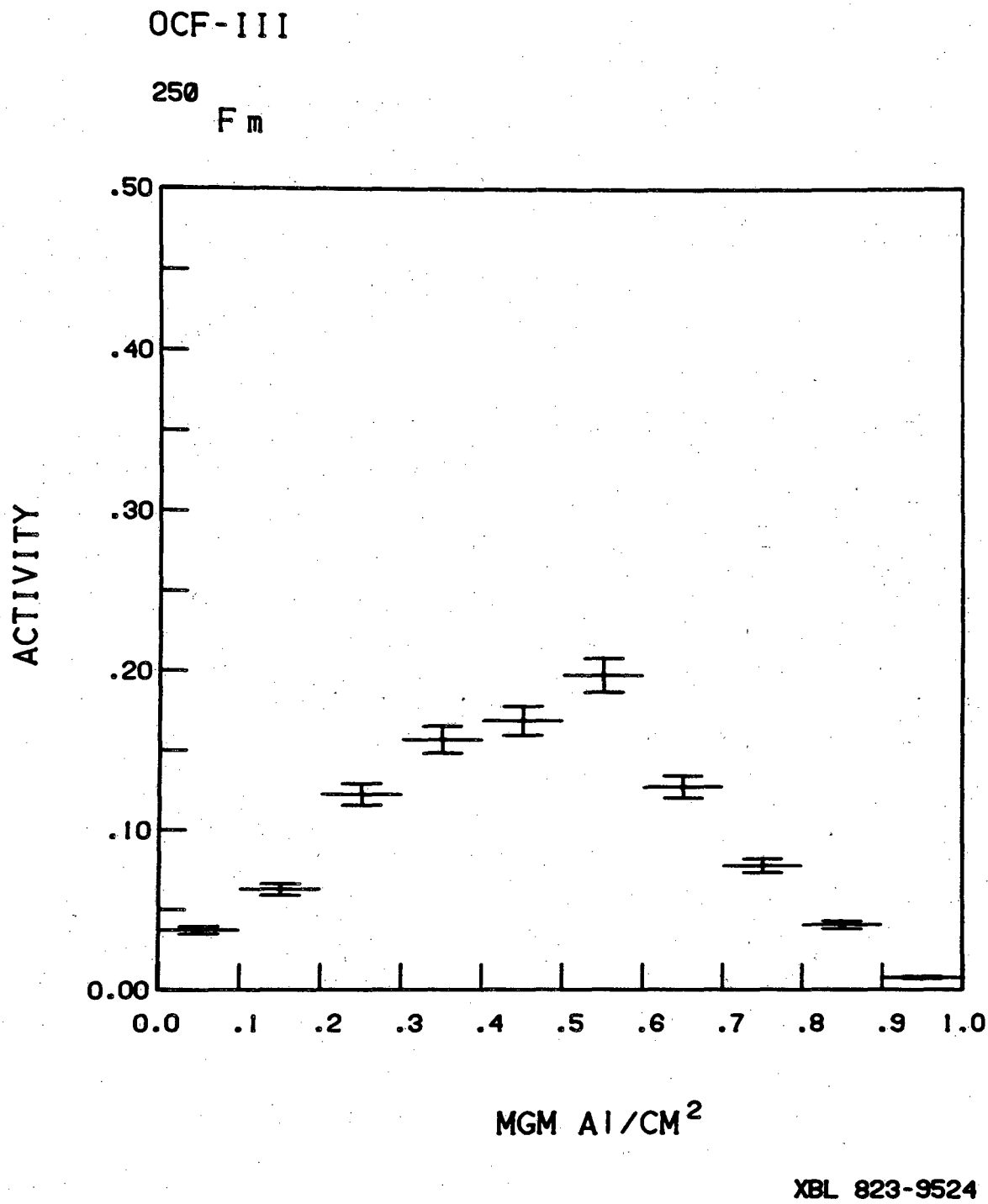
OCF-III
250 Fm
.50
.40
.30
.20
.10
0.00
ACTIVITY
0.0
.1
.2
.3
.4
.5
.6
.7
.8
.9
1.0
MGM Al/CM 2
XBL 823-9524

Fig. 8a

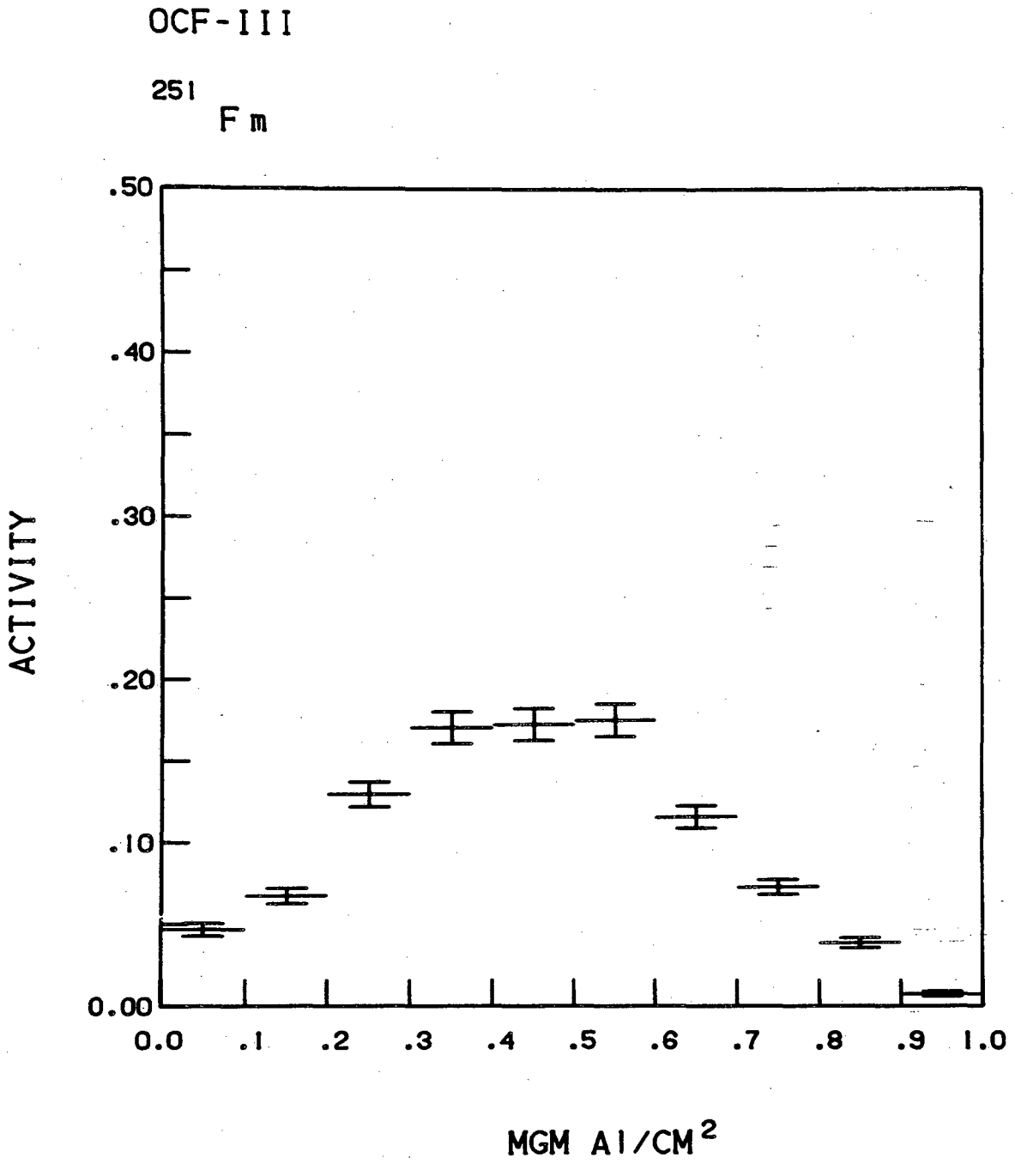
OCF-III
251
Fm
.50
.40
.30
.20
.10
0.00
ACTIVITY
0.0
.1
.2
.3
.4
.5
.6
.7
.8
.9
1.0
MGM Al/CM 2
XBL 823-9527

Fig. 8b

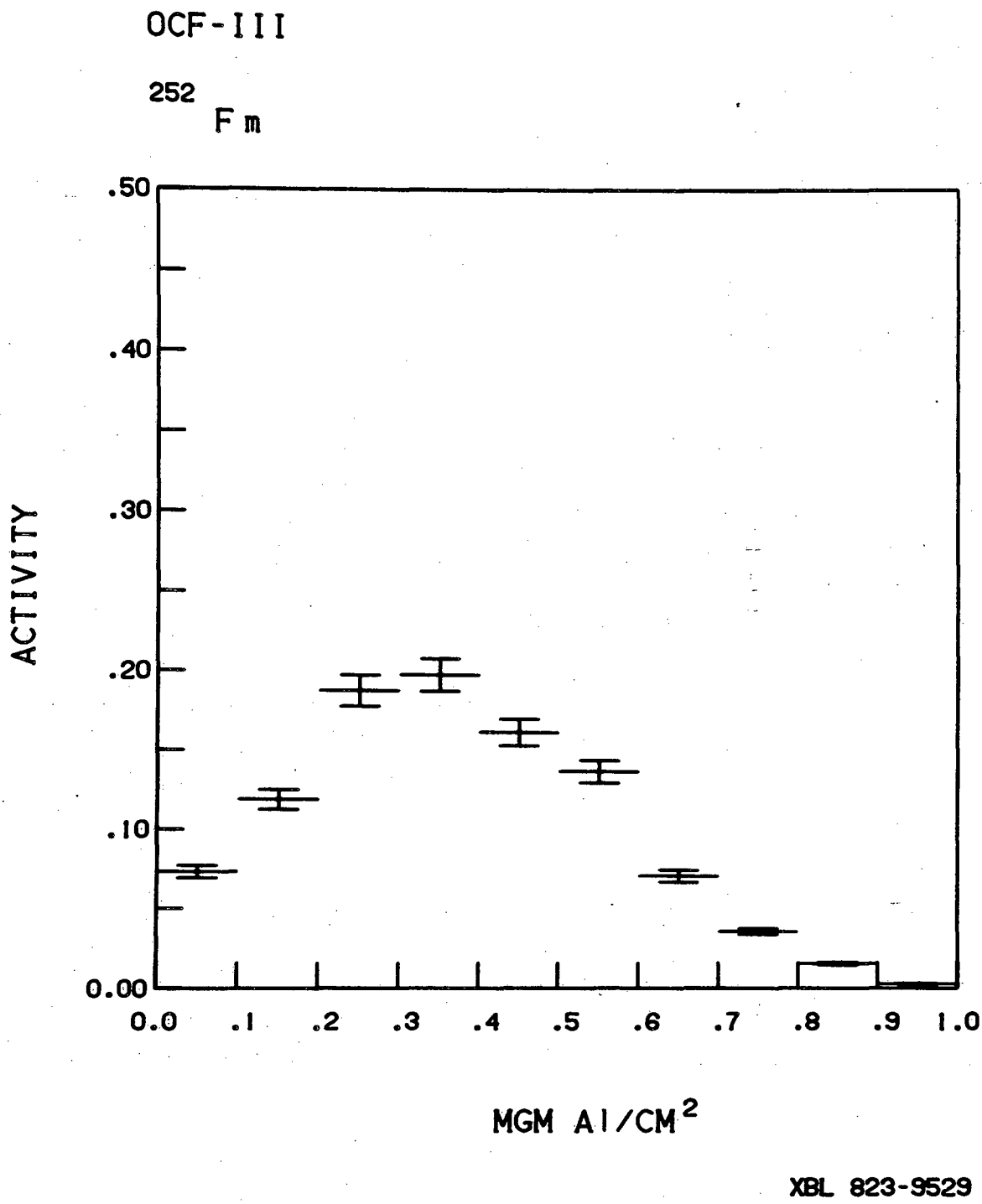
OCF-III
252
Fm
.50
.40
.30
.20
.10
0.00
ACTIVITY
0.0
.1
.2
.3
.4
.5
.6
.7
.8
.9
1.0
MGM Al/CM2
XBL 823-9529

Fig. 8c

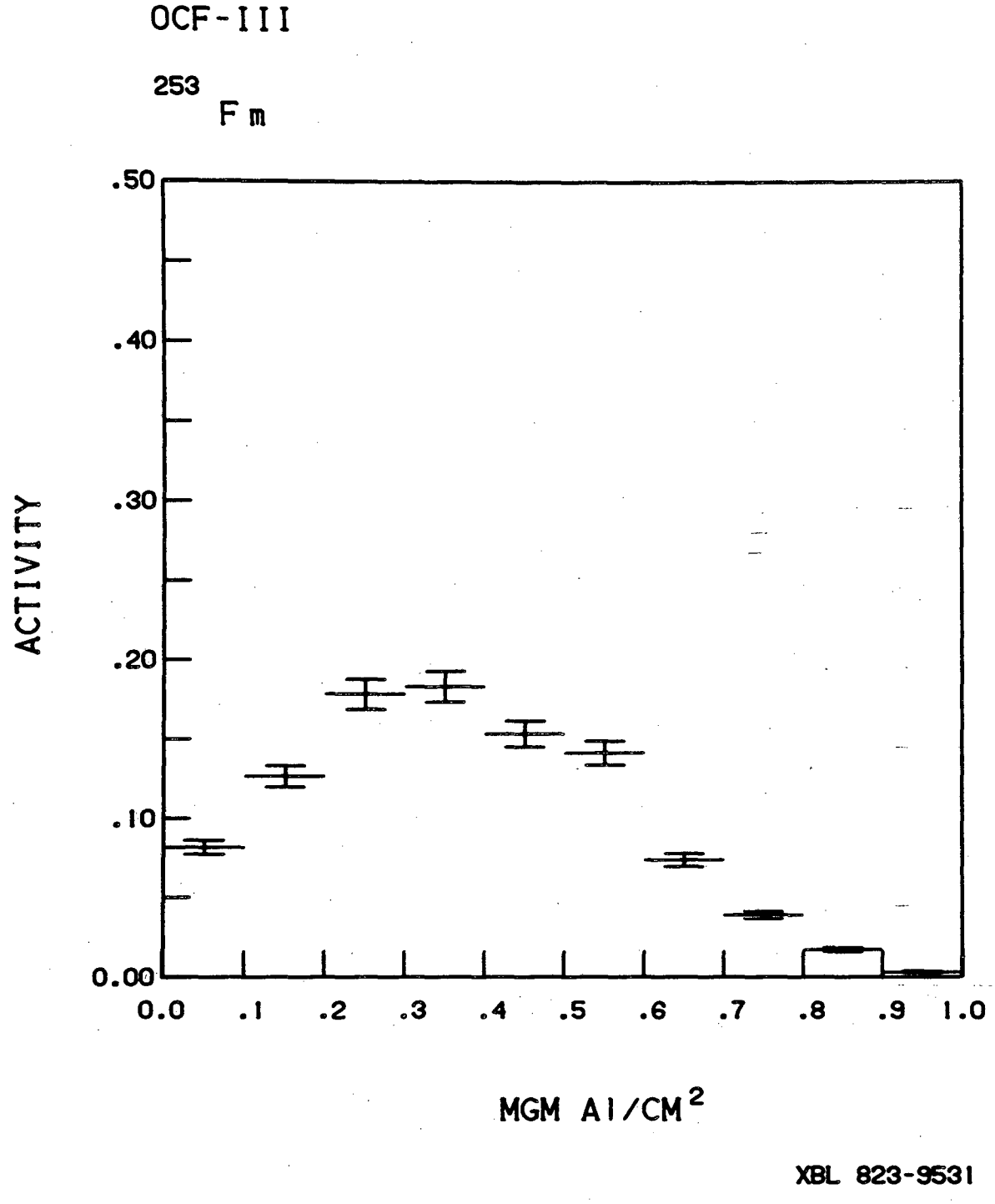
OCF-III
253
Fm
.50
.40
.30
.20
.10
0.00
ACTIVITY
0.0
.1
.2
.3
.4
.5
.6
.7
.8
.9
1.0
MGM Al/CM 2
XBL 823-9531

Fig. 8d

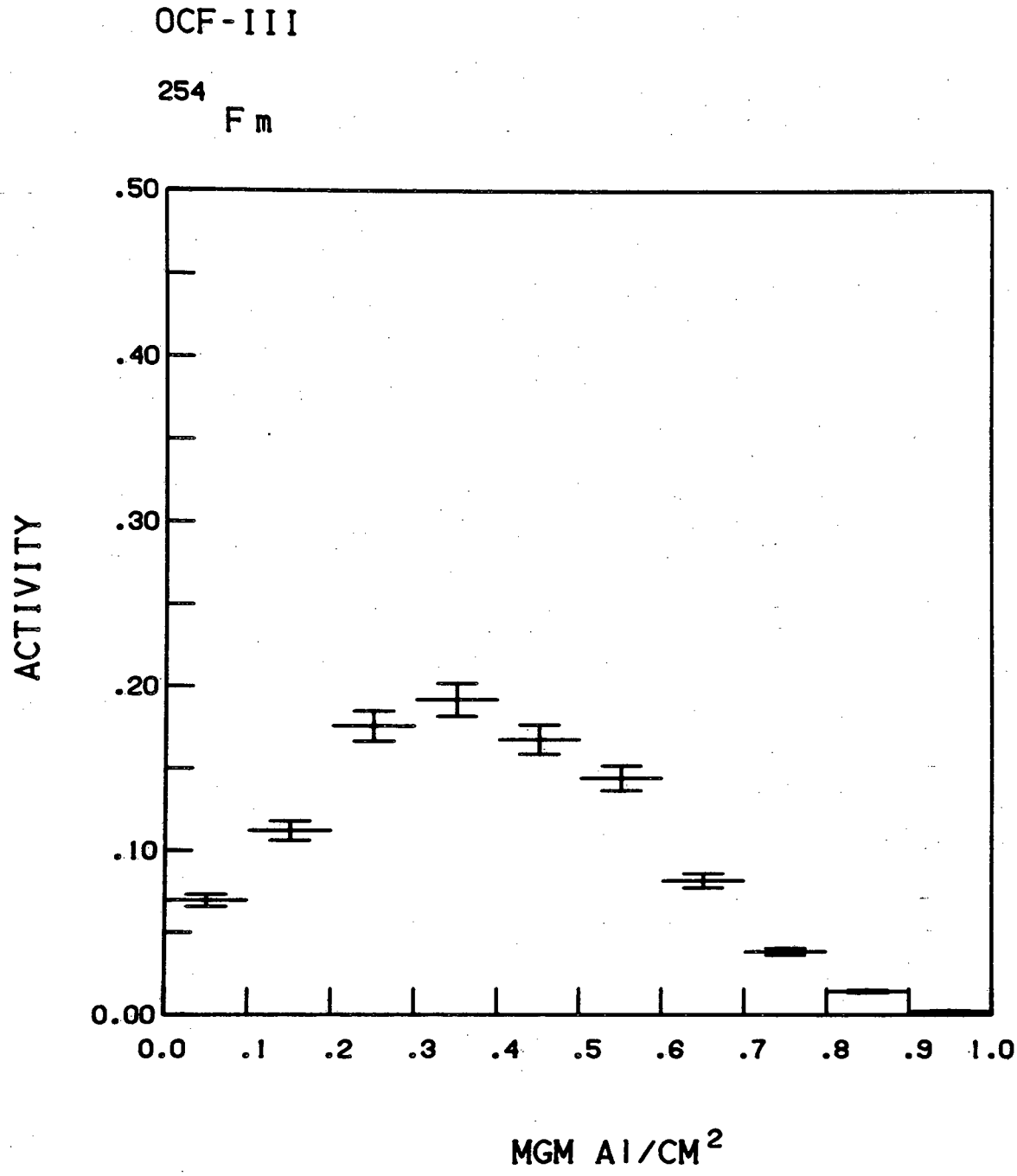
OCF-III
254
Fm
.50
.40
.30
.20
.10
0.00
ACTIVITY
0.0
.1
.2
.3
.4
.5
.6
.7
.8
.9
1.0
MGM Al/CM 2
XBL 823-9526

Fig. 8e

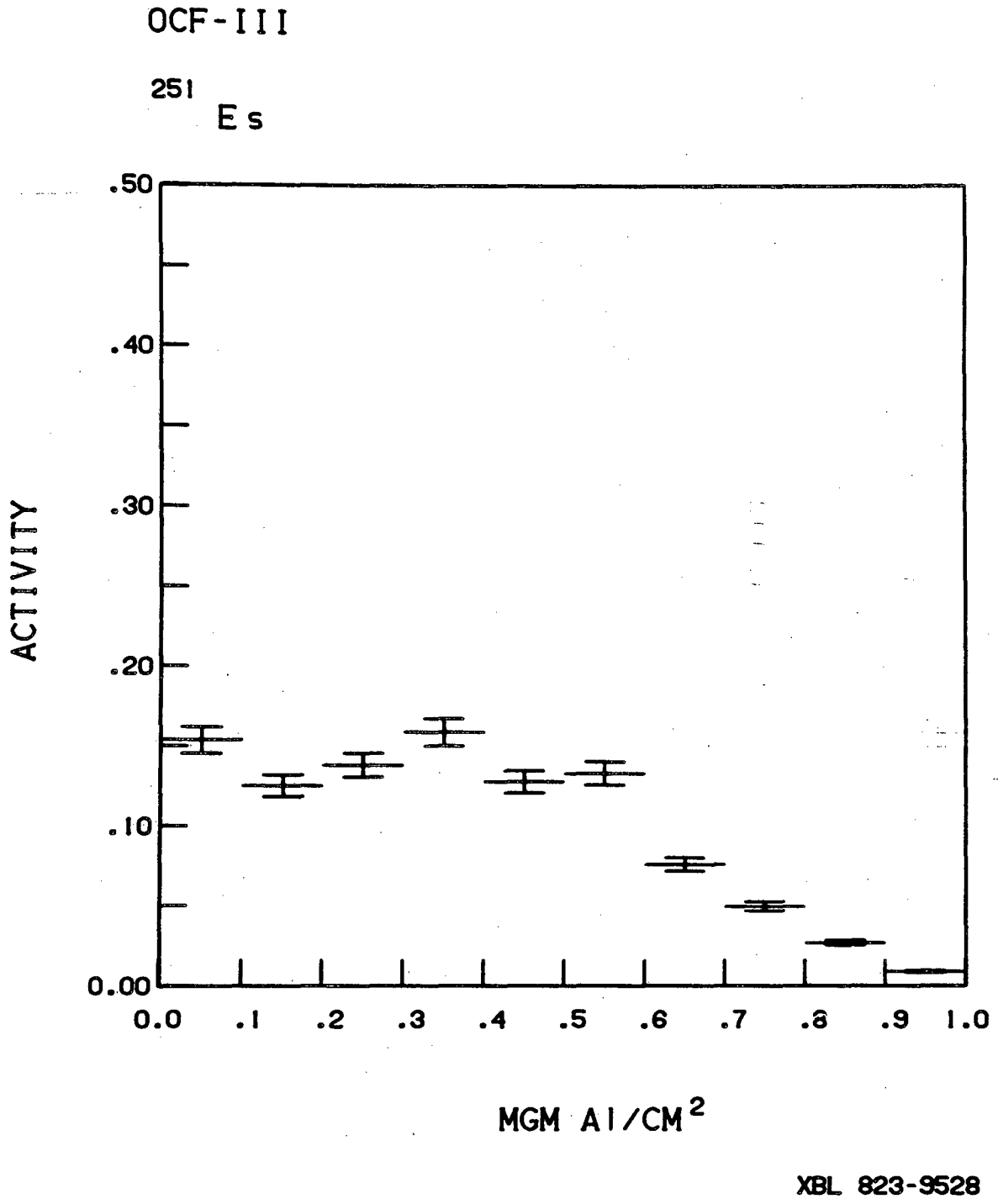
OCF-III
251
Es
.50
.40
.30
.20
.10
0.00
ACTIVITY
0.0
.1
.2
.3
.4
.5
.6
.7
.8
.9
1.0
MGM Al/CM 2
XBL 823-9528

Fig. 9a

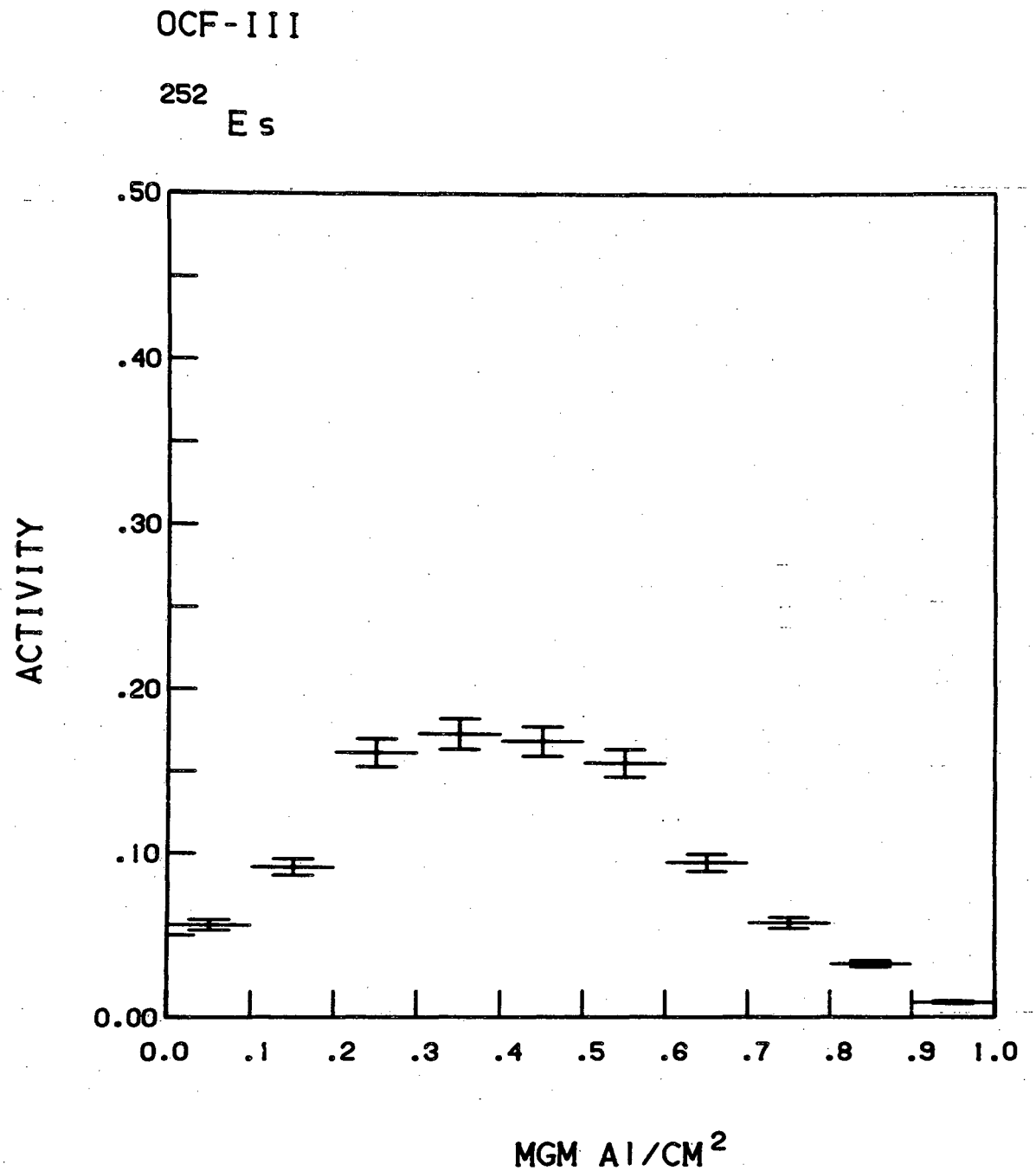
OCF-III
252 Es
ACTIVITY
.50
.40
.30
.20
.10
0.00
0.0
.1
.2
.3
.4
.5
.6
.7
.8
.9
1.0
MGM Al/CM 2
XBL 823-9532

Fig. 9b

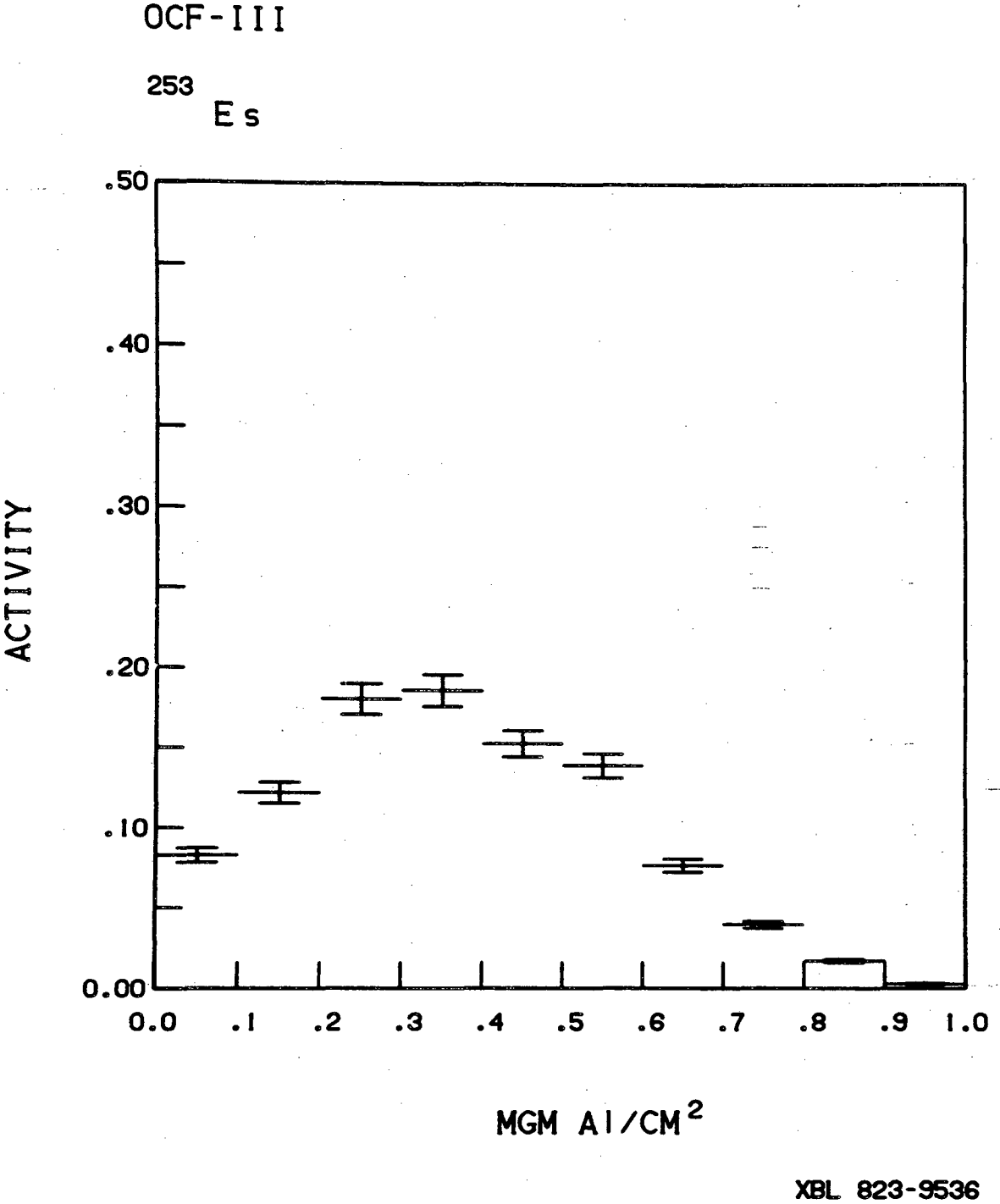
OCF-III
253 Es
.50
.40
.30
.20
.10
0.00
ACTIVITY
0.0
.1
.2
.3
.4
.5
.6
.7
.8
.9
1.0
MGM Al/CM 2
XBL 823-9536

Fig. 9c

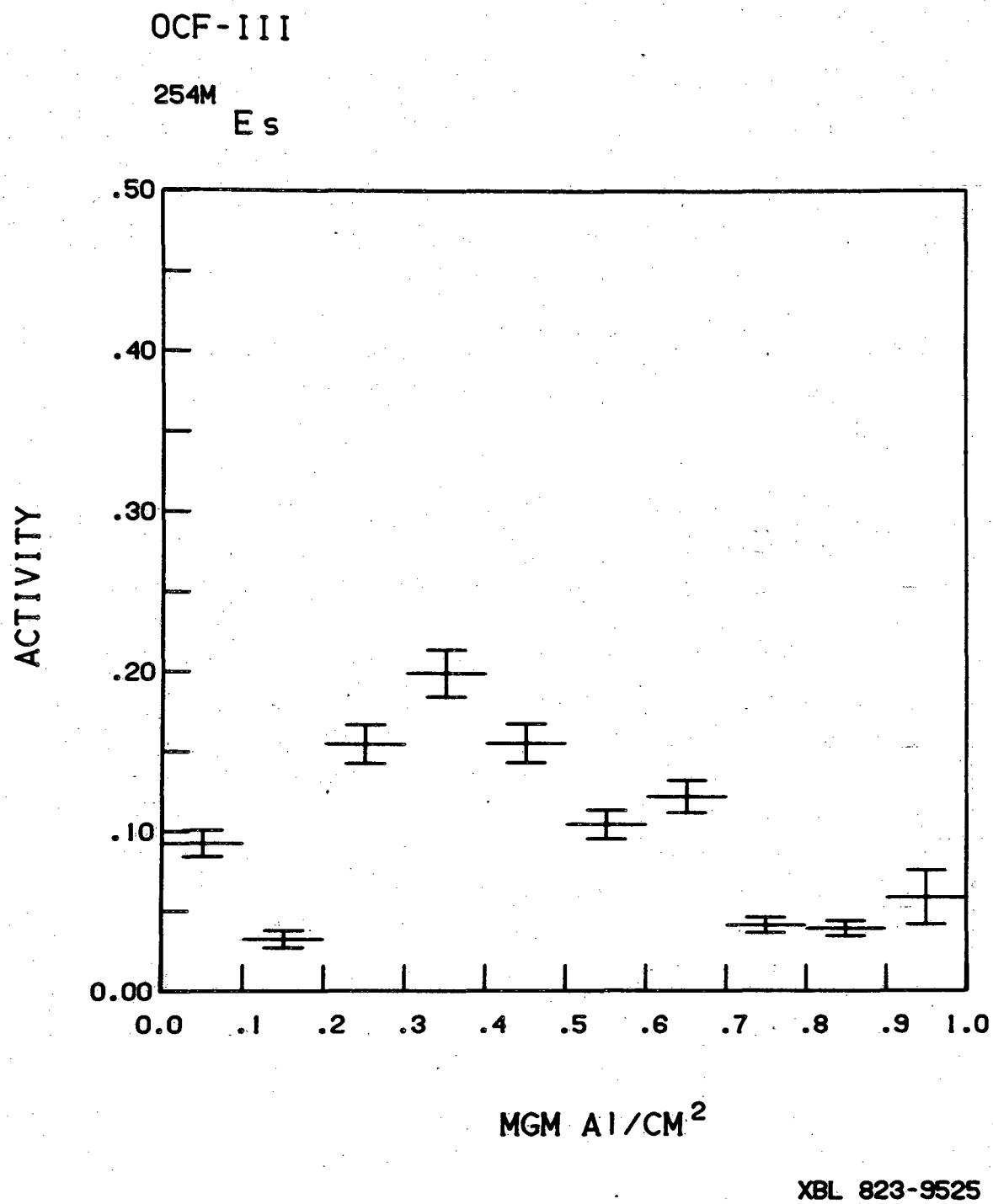
OCF-III
254M
Es
.50
.40
.30
.20
.10
0.00
ACTIVITY
0.0
.1
.2
.3
.4
.5
.6
.7
.8
.9
1.0
MGM Al/CM2
XBL 823-9525

Fig. 9d

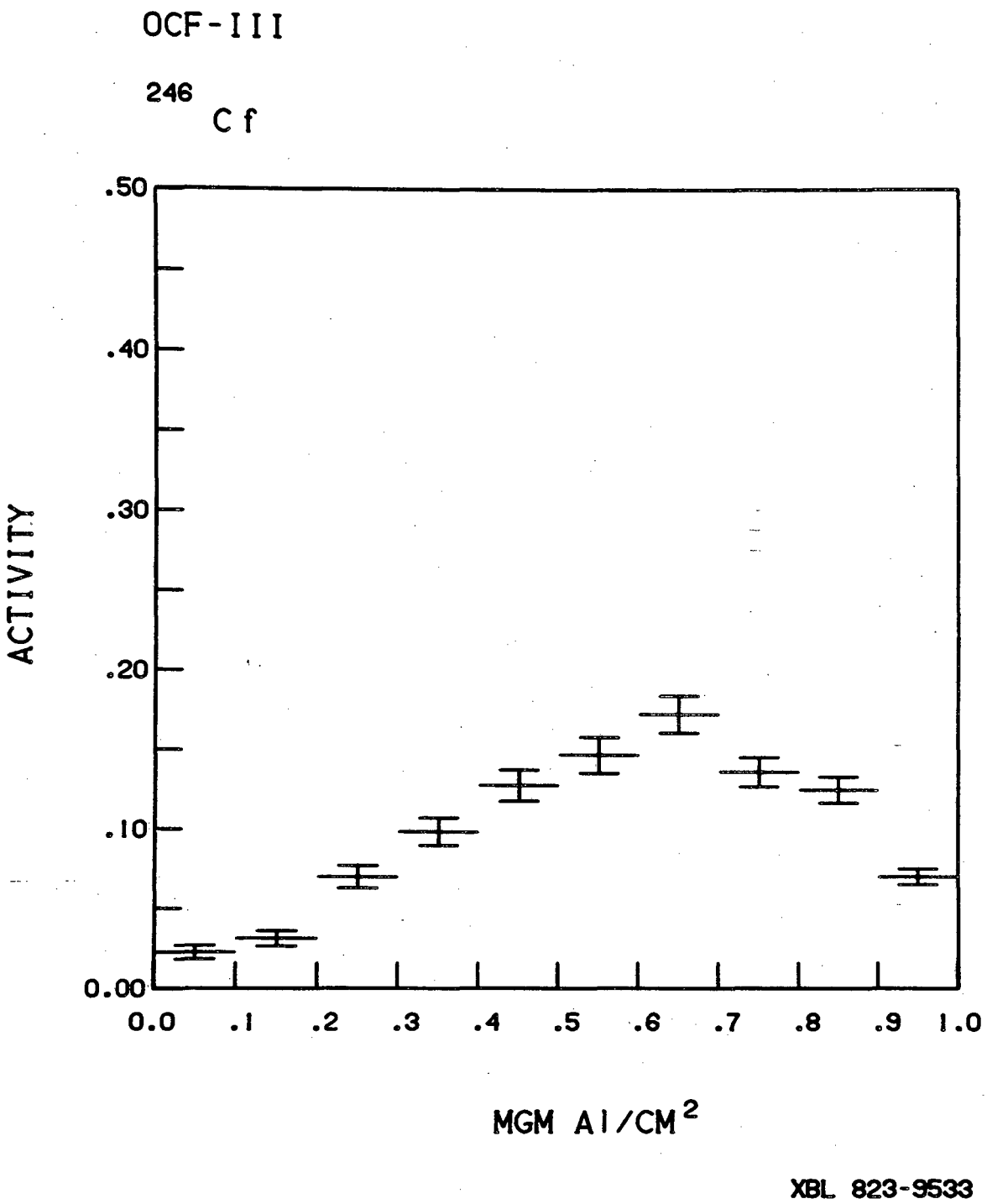
OCF-III
246 Cf
ACTIVITY
.50
.40
.30
.20
.10
0.00
0.0
.1
.2
.3
.4
.5
.6
.7
.8
.9
1.0
MGM Al/CM 2
XBL 823-9533

Fig. 10a

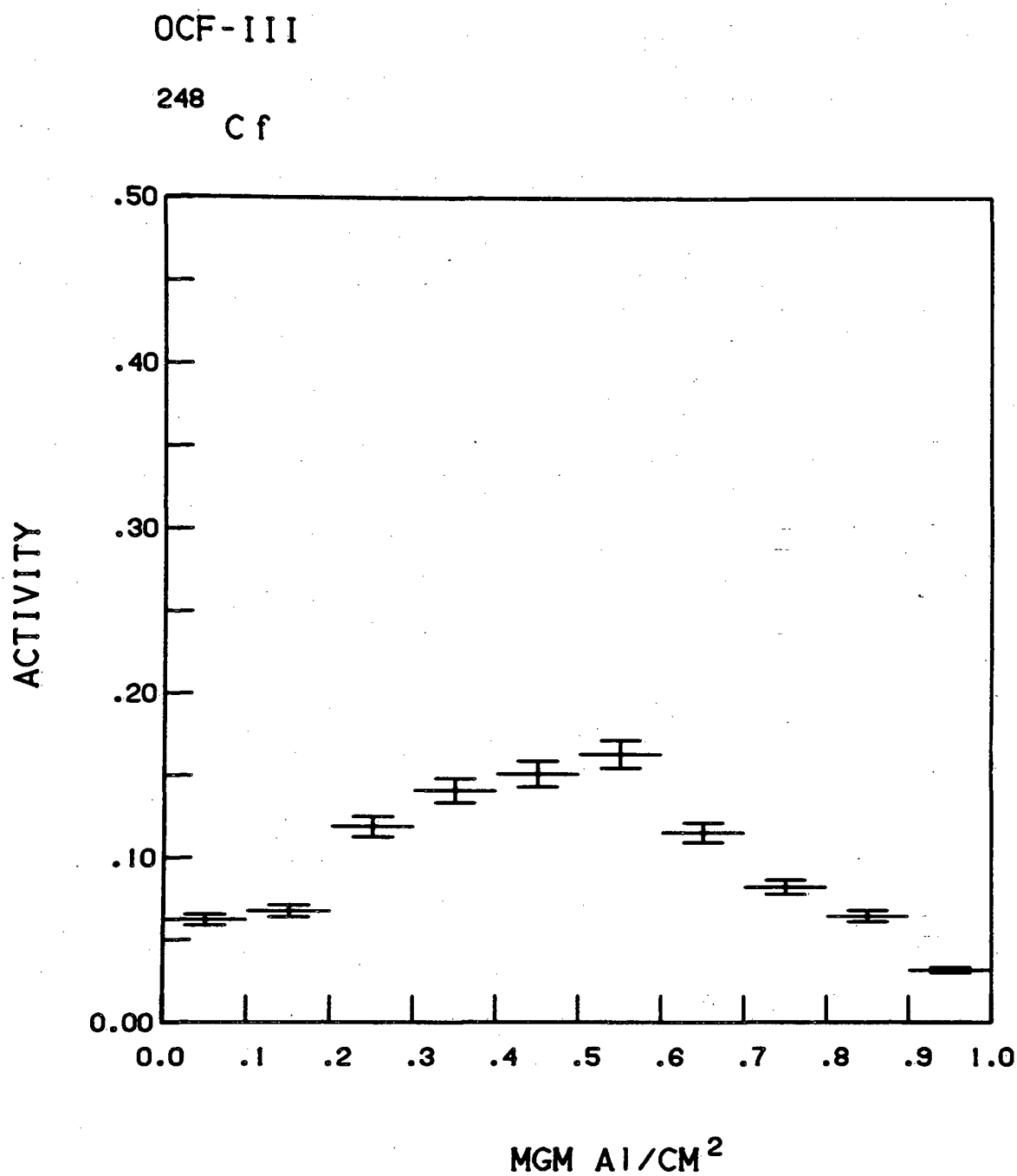
OCF-III
248 Cf
ACTIVITY
.50
.40
.30
.20
.10
0.00
0.0
.1
.2
.3
.4
.5
.6
.7
.8
.9
1.0
MGM Al/CM 2
XBL 823-9530

Fig. 10b

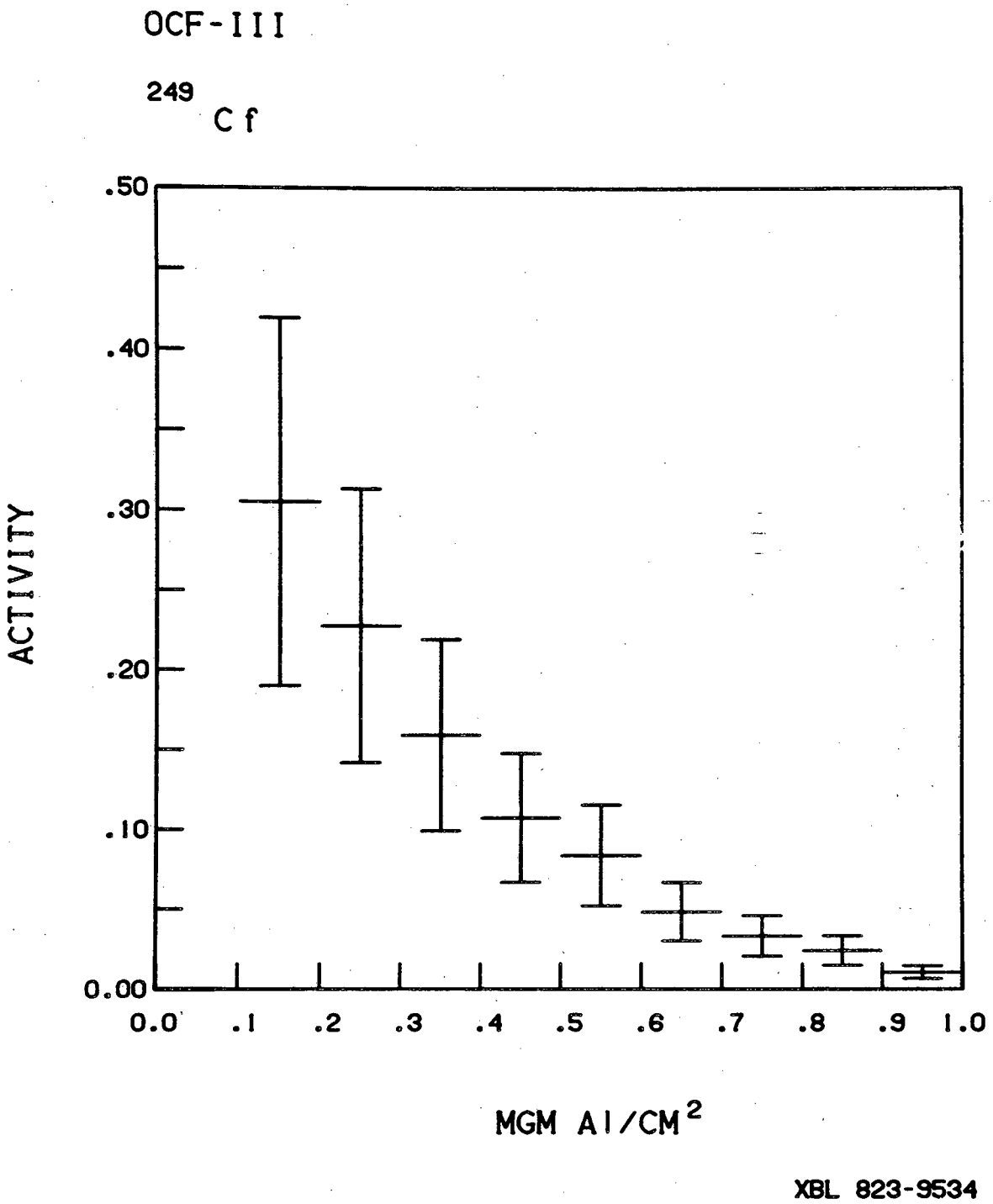
OCF-III
249 Cf
.50
.40
.30
.20
.10
0.00
ACTIVITY
0.0
.1
.2
.3
.4
.5
.6
.7
.8
.9
1.0
MGM Al/CM 2
XBL 823-9534

Fig. 10c

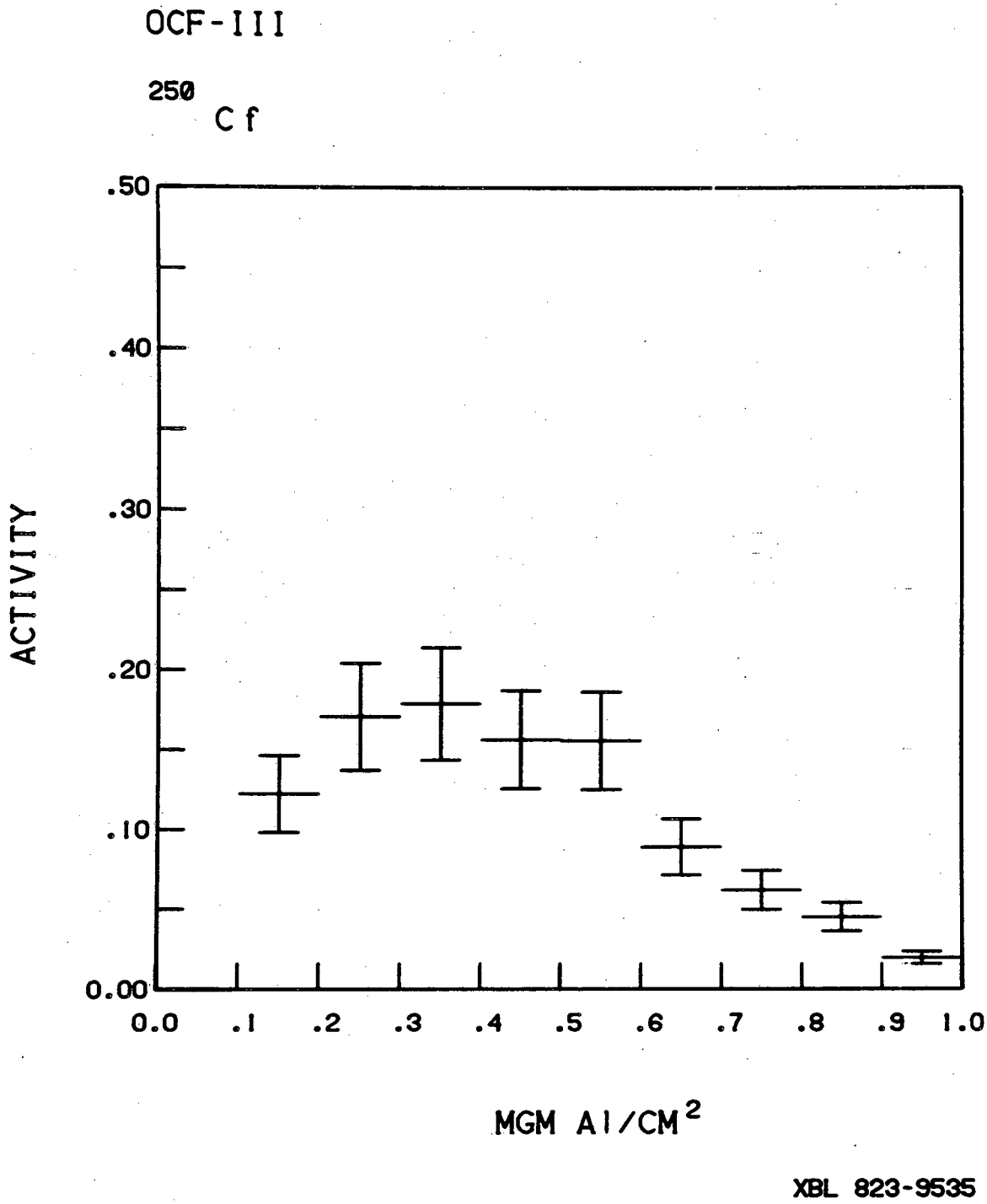
OCF-III
250 Cf
.50
.40
.30
.20
.10
0.00
ACTIVITY
0.0
.1
.2
.3
.4
.5
.6
.7
.8
.9
1.0
MGM Al/CM 2
XBL 823-9535

Fig. 10d

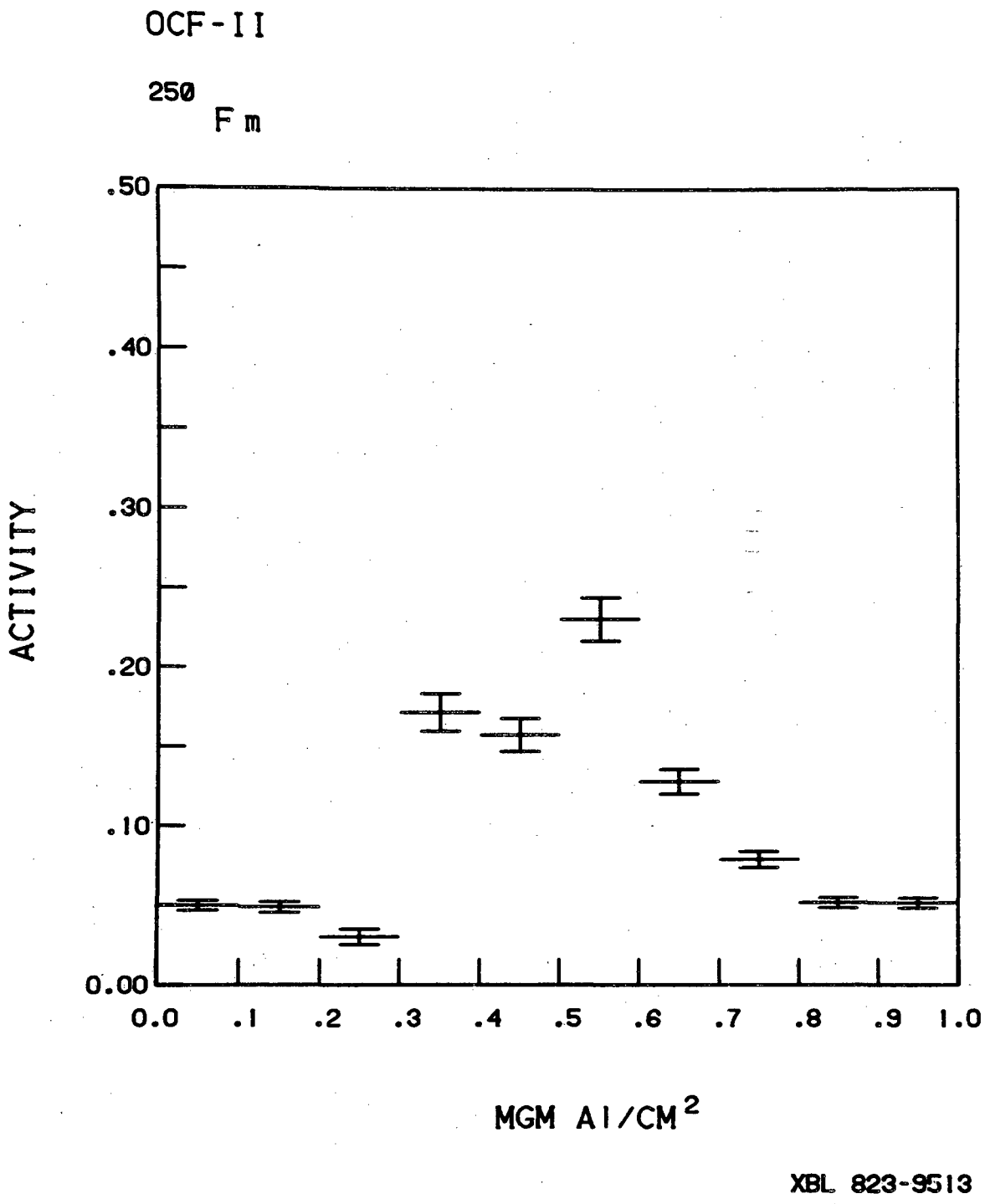
OCF-II
250
Fm
.50
.40
.30
.20
.10
0.00
ACTIVITY
0.0
.1
.2
.3
.4
.5
.6
.7
.8
.9
1.0
MGM Al/CM2
XBL 823-9513

Fig. 11a

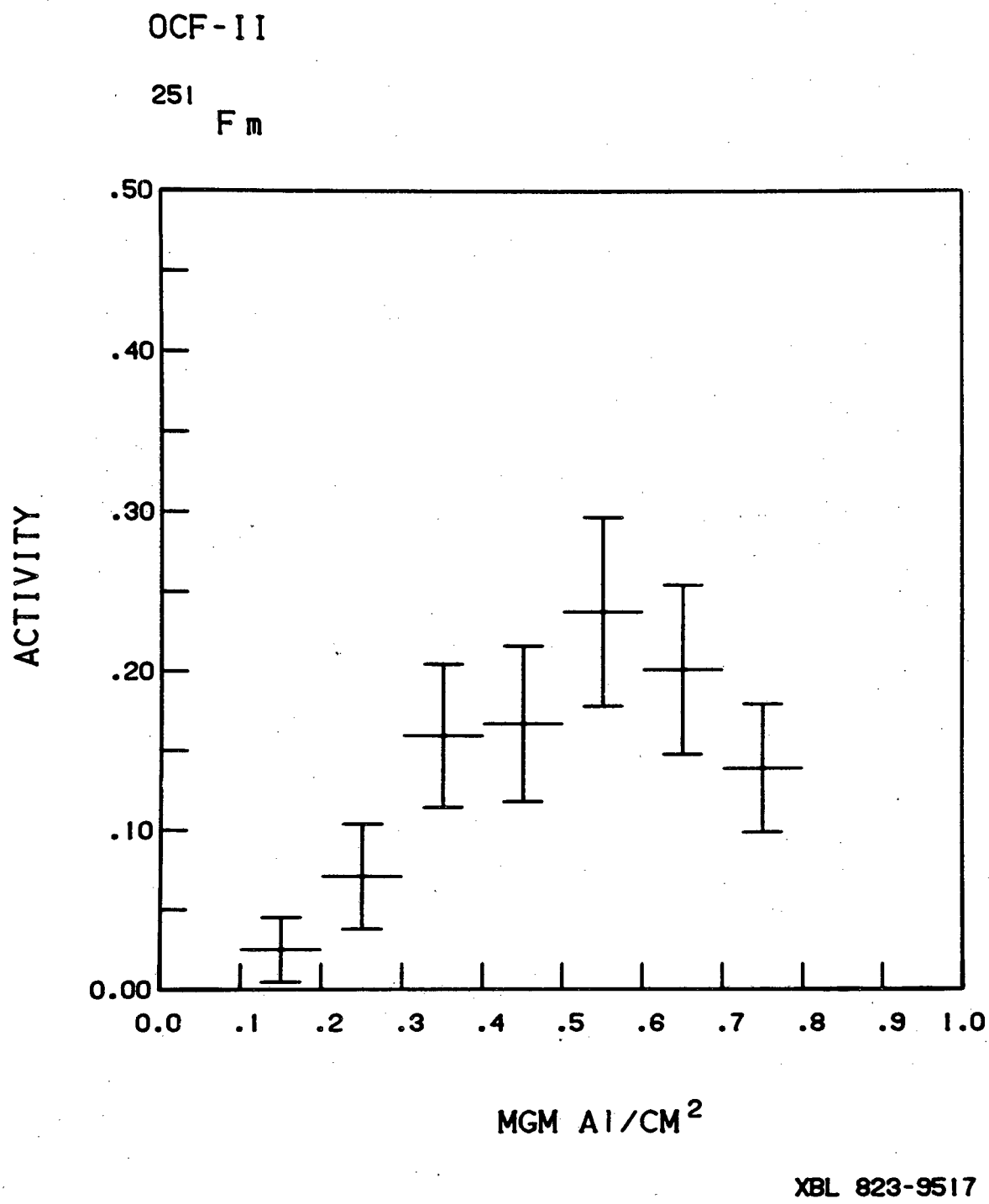
OCF-II
251
Fm
.50
.40
.30
.20
.10
0.00
ACTIVITY
0.0
.1
.2
.3
.4
.5
.6
.7
.8
.9
1.0
MGM Al/CM 2
XBL 823-9517

Fig. 11b

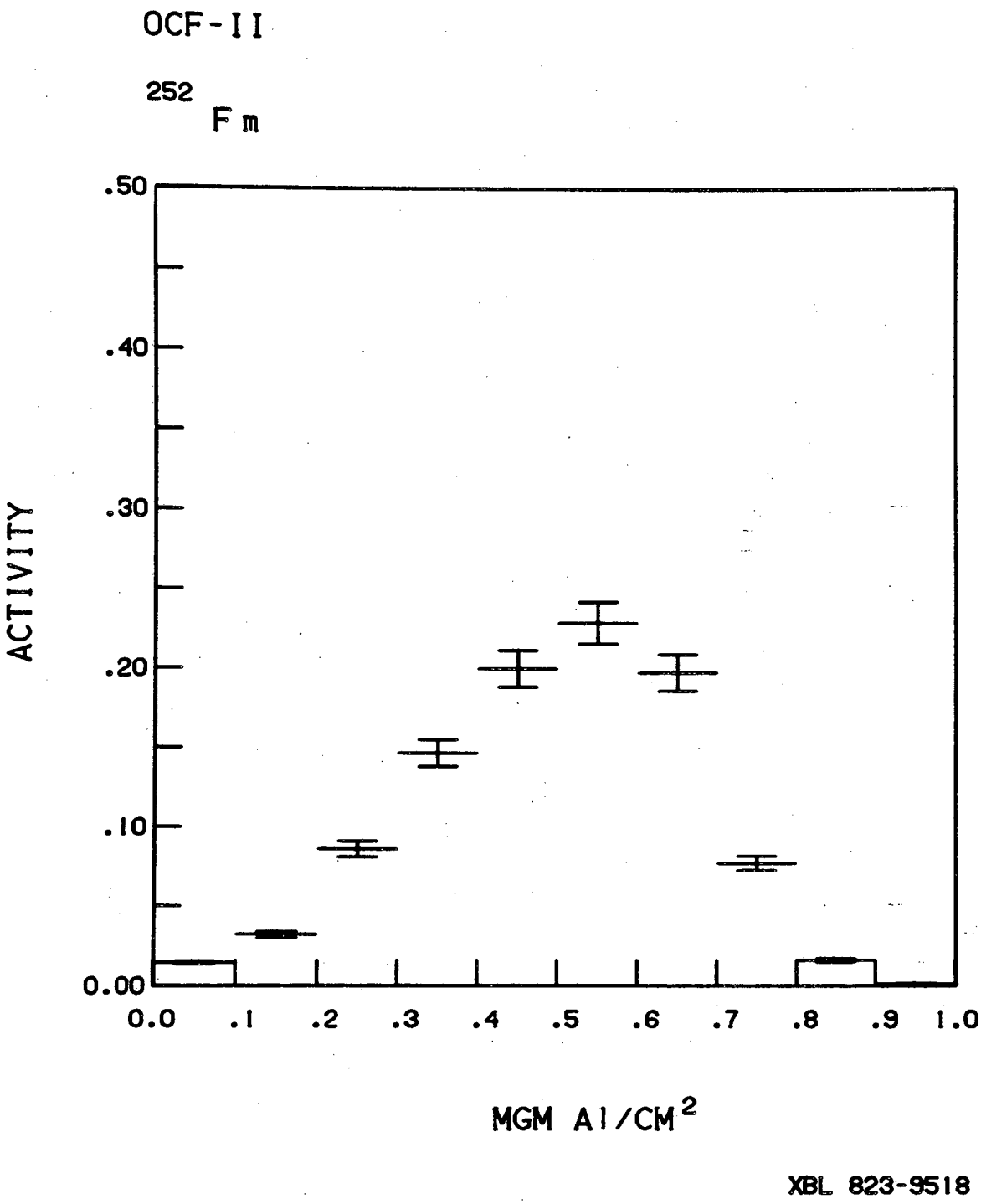
OCF-II
252 Fm
ACTIVITY
.50
.40
.30
.20
.10
0.00
0.0
.1
.2
.3
.4
.5
.6
.7
.8
.9
1.0
MGM Al/CM 2
XBL 823-9518

Fig. 11c

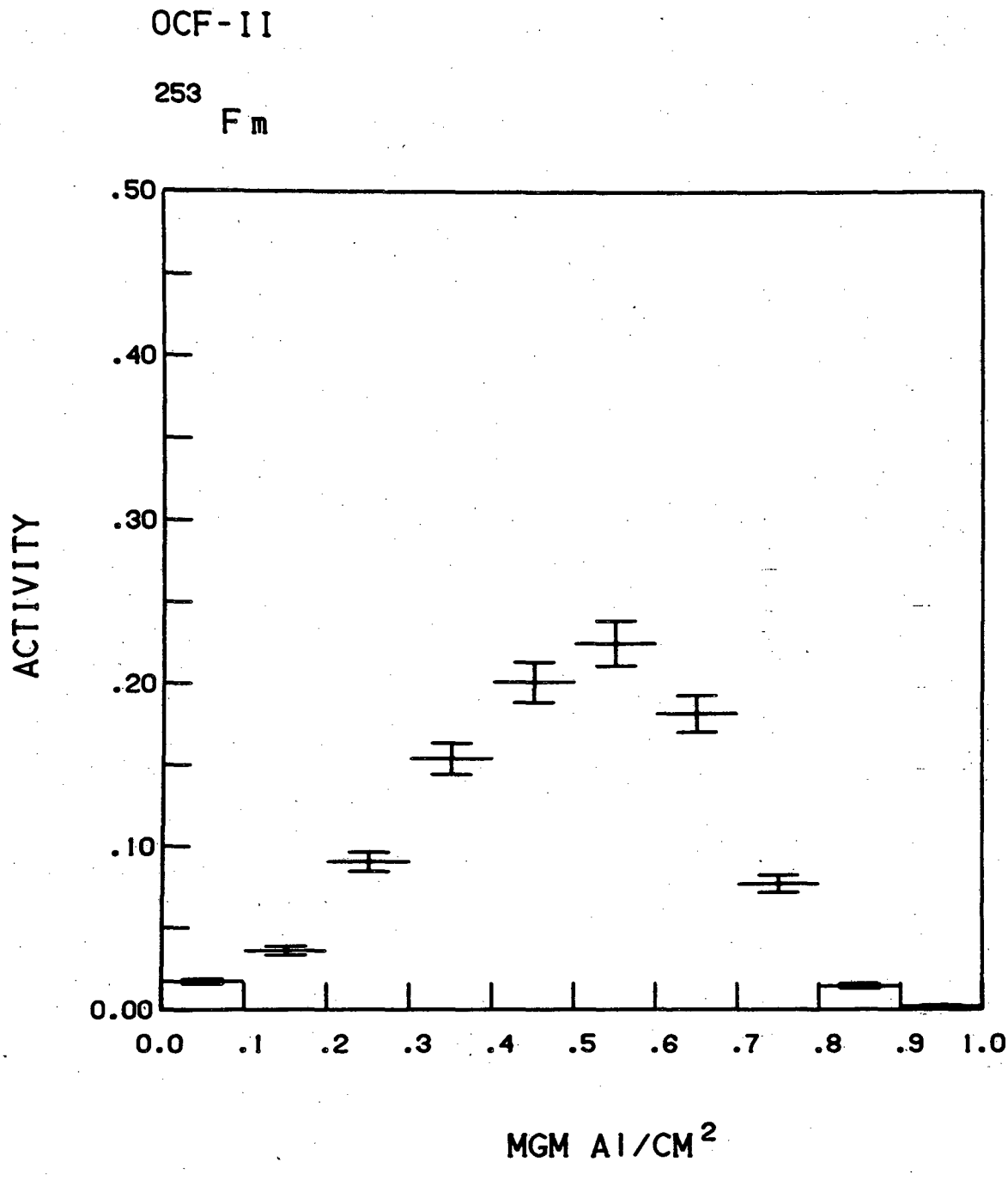
OCF-II
253 Fm
ACTIVITY
.50
.40
.30
.20
.10
0.00
0.0
.1
.2
.3
.4
.5
.6
.7
.8
.9
1.0
MGM Al/CM 2
XBL 823-9519

Fig. 11d

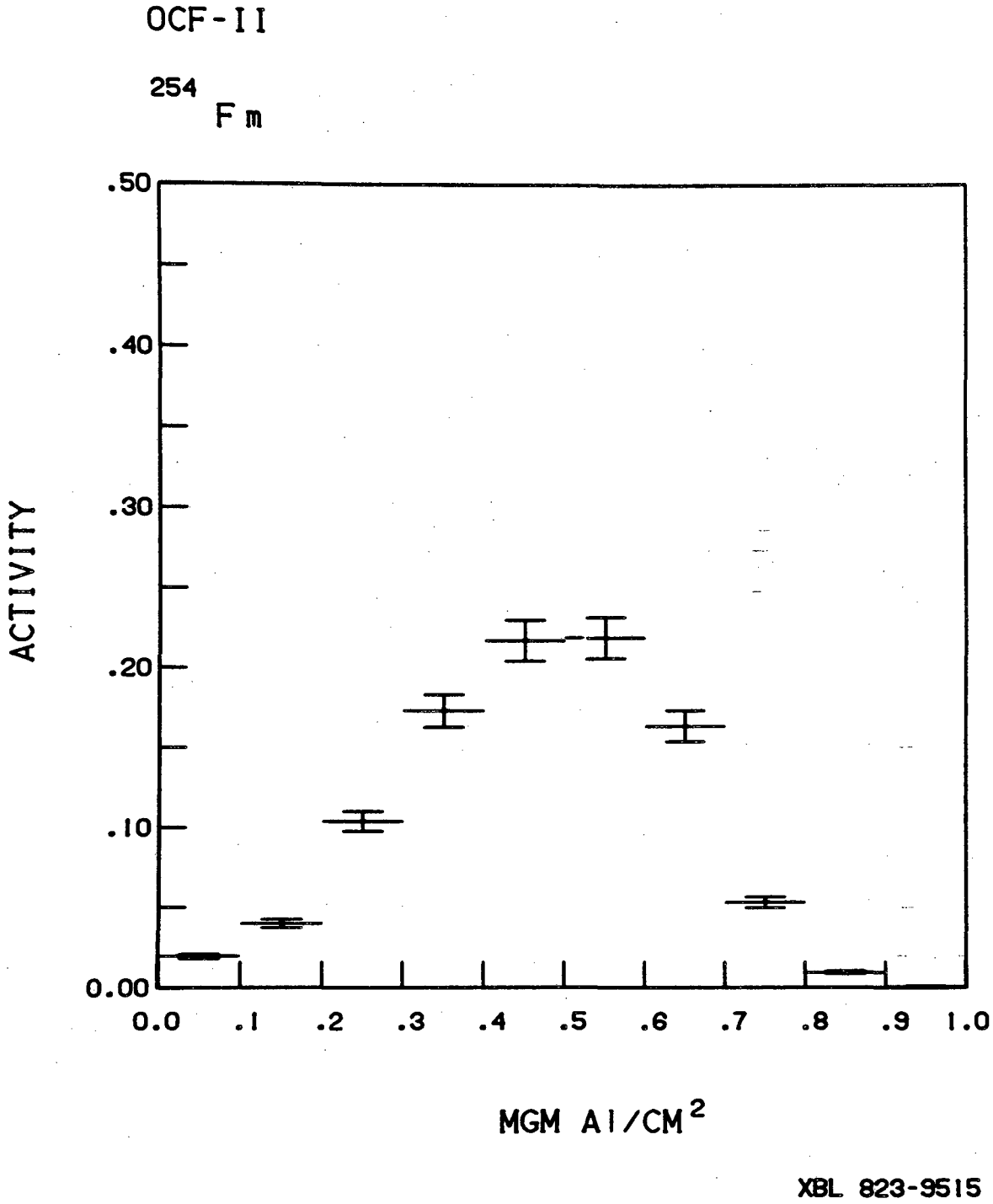
OCF-II
254
Fm
.50
.40
.30
.20
.10
0.00
ACTIVITY
0.0
.1
.2
.3
.4
.5
.6
.7
.8
.9
1.0
MGM Al/CM2
XBL 823-9515

Fig. 11e

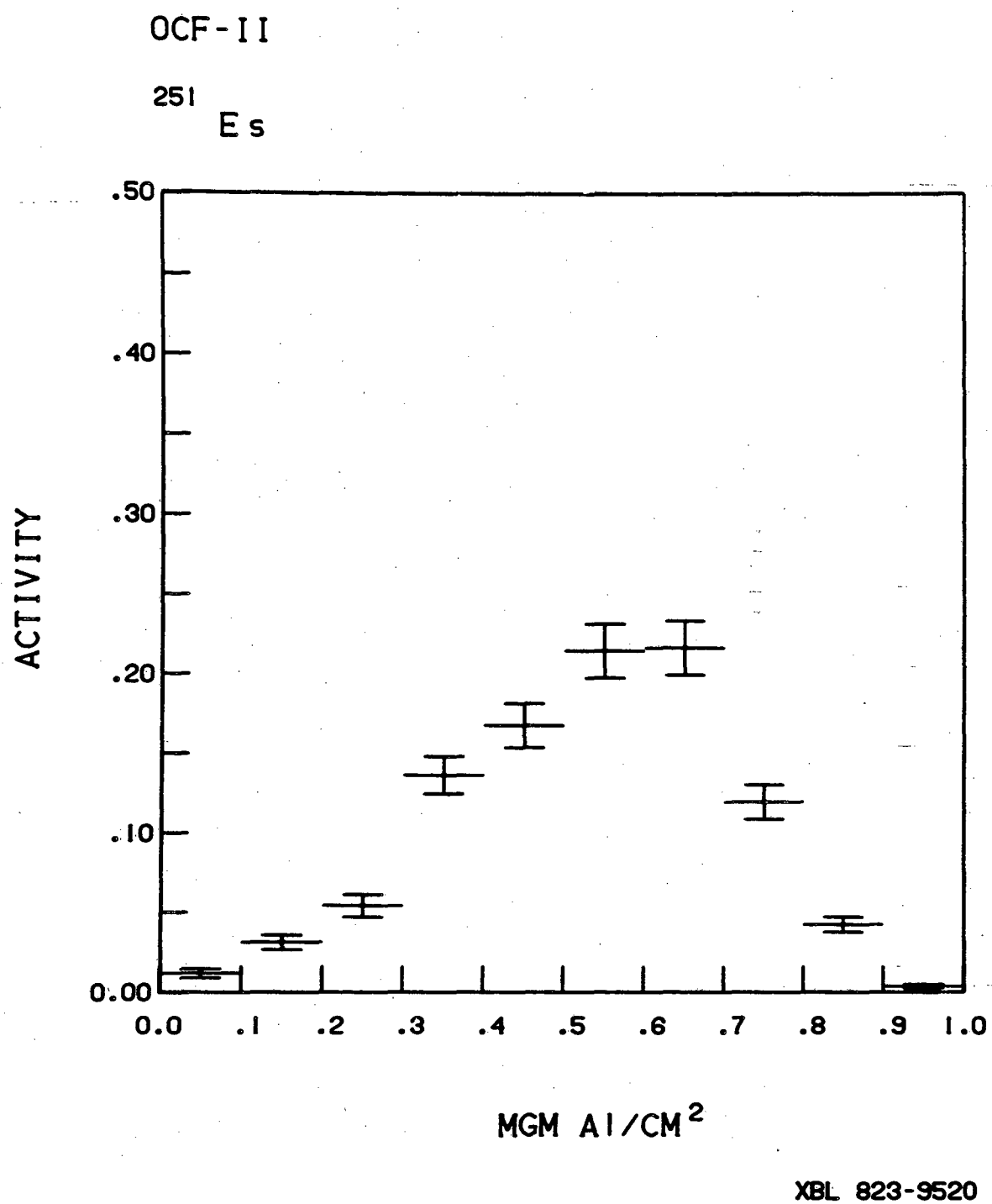
OCF-II
251
Es
.50
.40
.30
.20
.10
0.00
ACTIVITY
0.0
.1
.2
.3
.4
.5
.6
.7
.8
.9
1.0
MGM Al/CM 2
XBL 823-9520

Fig. 12a

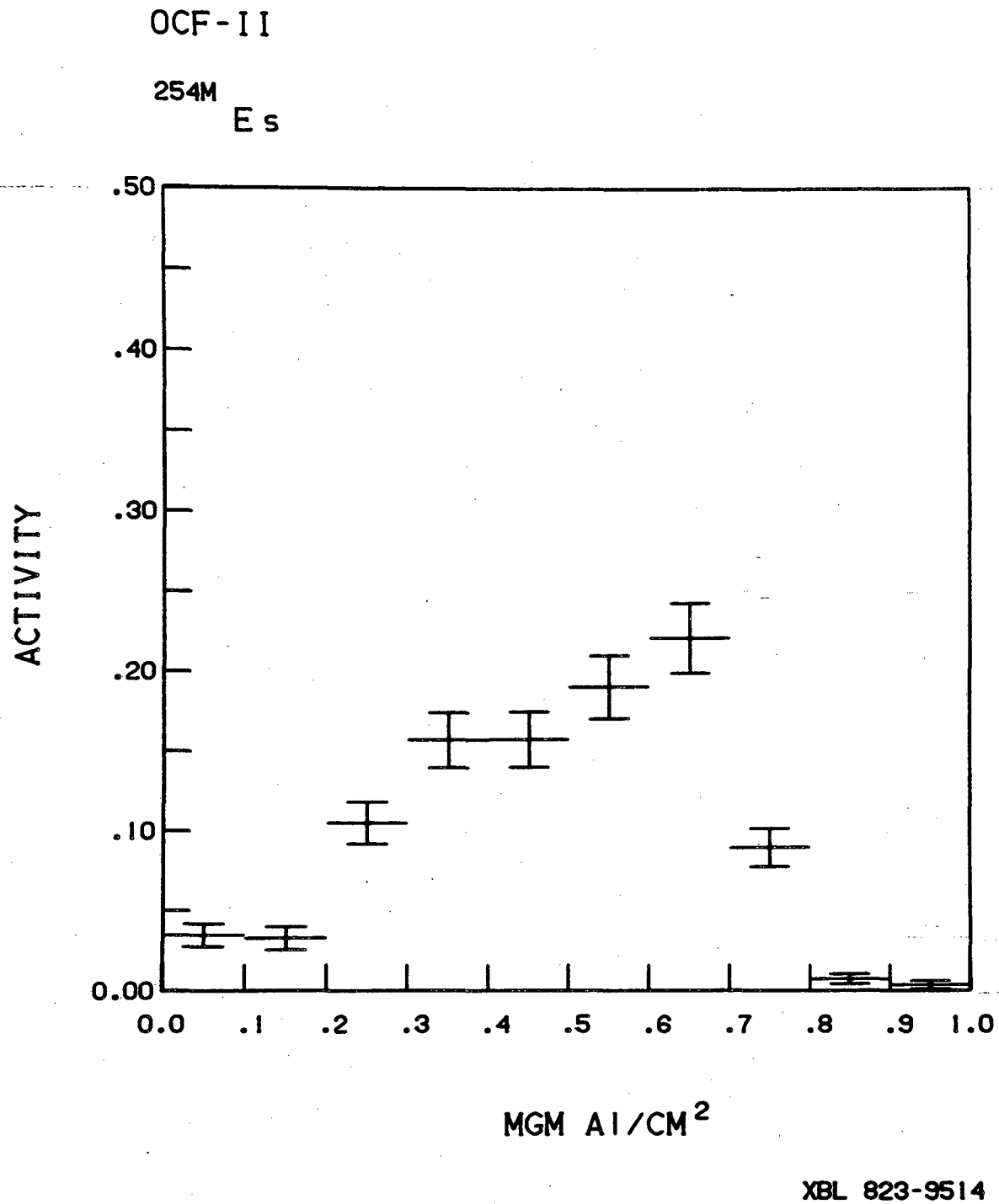
OCF-II
254M Es
.50
.40
.30
.20
.10
0.00
ACTIVITY
0.0
.1
.2
.3
.4
.5
.6
.7
.8
.9
1.0
MGM Al/CM 2
XBL 823-9514

Fig. 12b

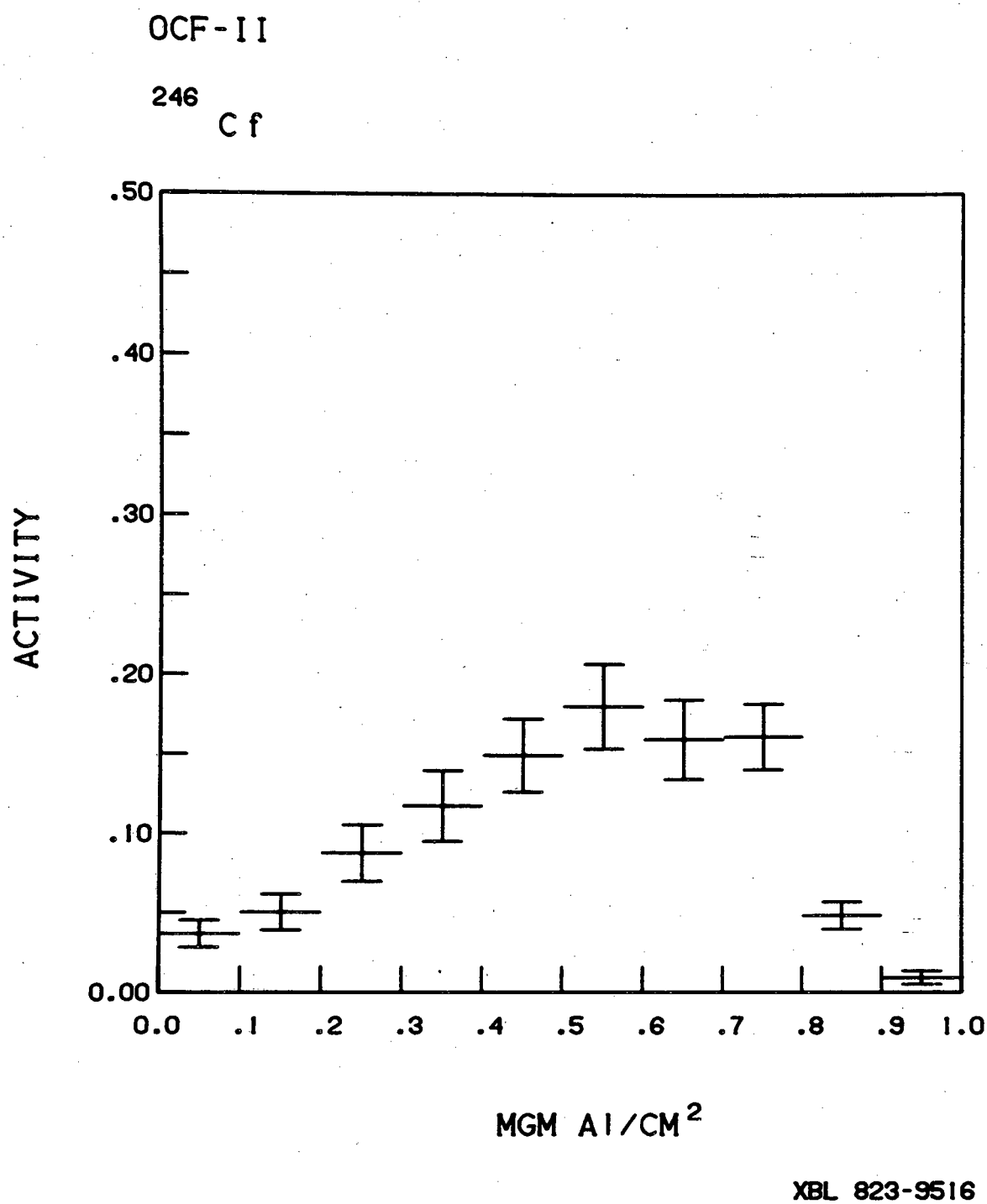
OCF-II
246 Cf
.50
.40
.30
.20
.10
0.00
ACTIVITY
0.0
.1
.2
.3
.4
.5
.6
.7
.8
.9
1.0
MGM Al/CM 2
XBL 823-9516

Fig. 13a

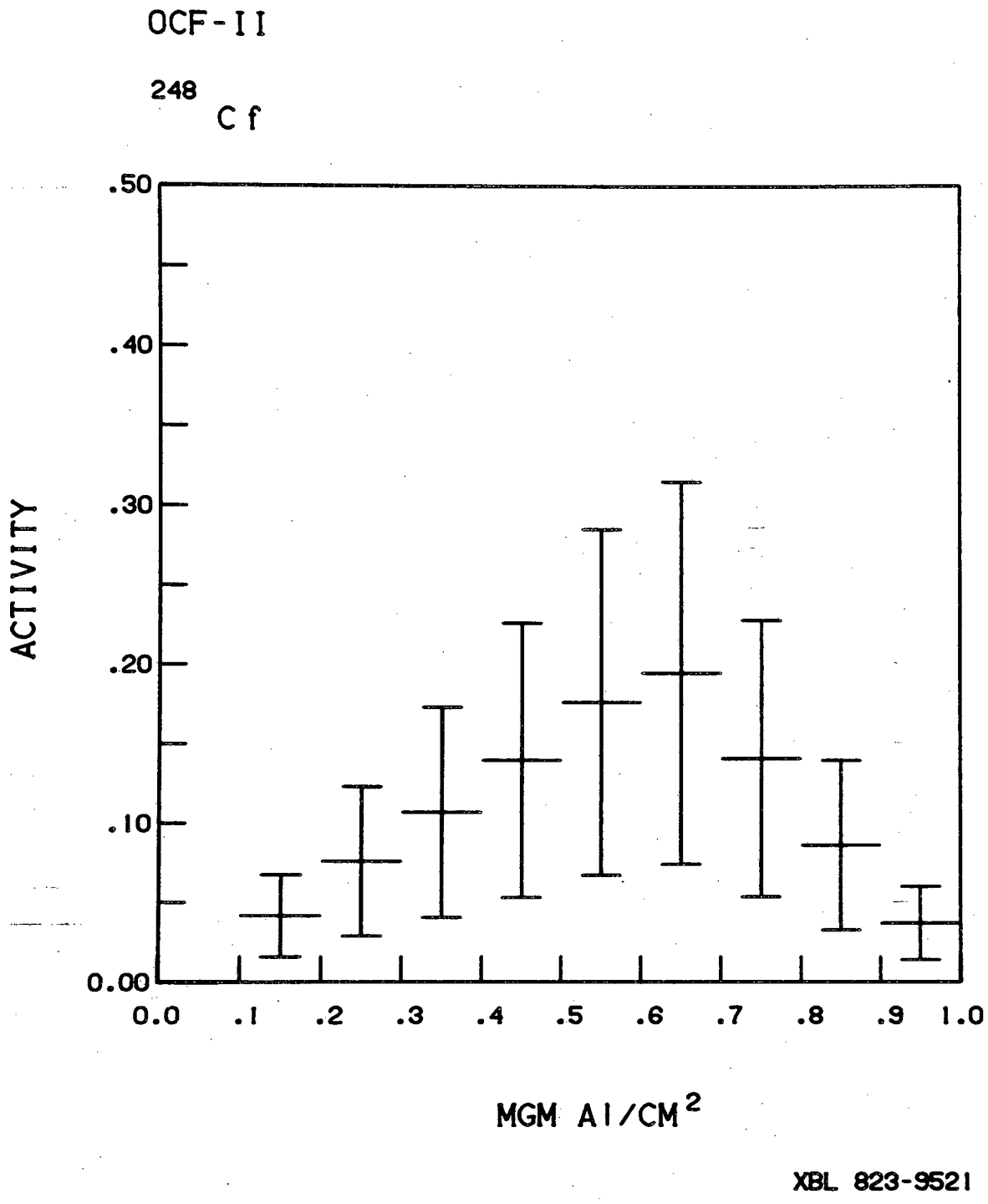
OCF-II
248 Cf
.50
.40
.30
.20
.10
0.00
ACTIVITY
0.0
.1
.2
.3
.4
.5
.6
.7
.8
.9
1.0
MGM Al/CM 2
XBL 823-9521

Fig. 13b

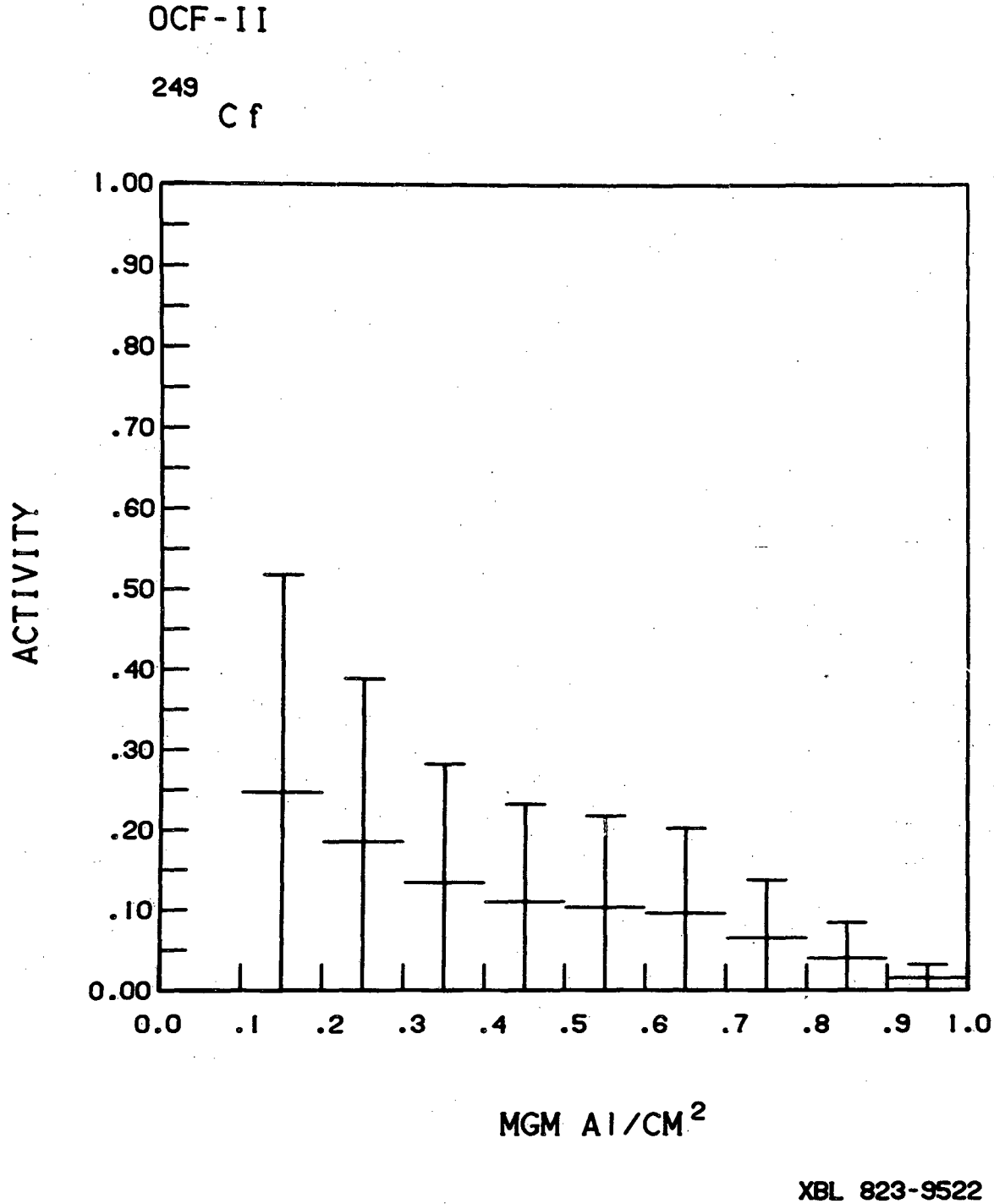
OCF-II
249 Cf
ACTIVITY
1.00
.90
.80
.70
.60
.50
.40
.30
.20
.10
0.00
0.0
.1
.2
.3
.4
.5
.6
.7
.8
.9
1.0
MGM Al/CM2
XBL 823-9522

Fig. 13c

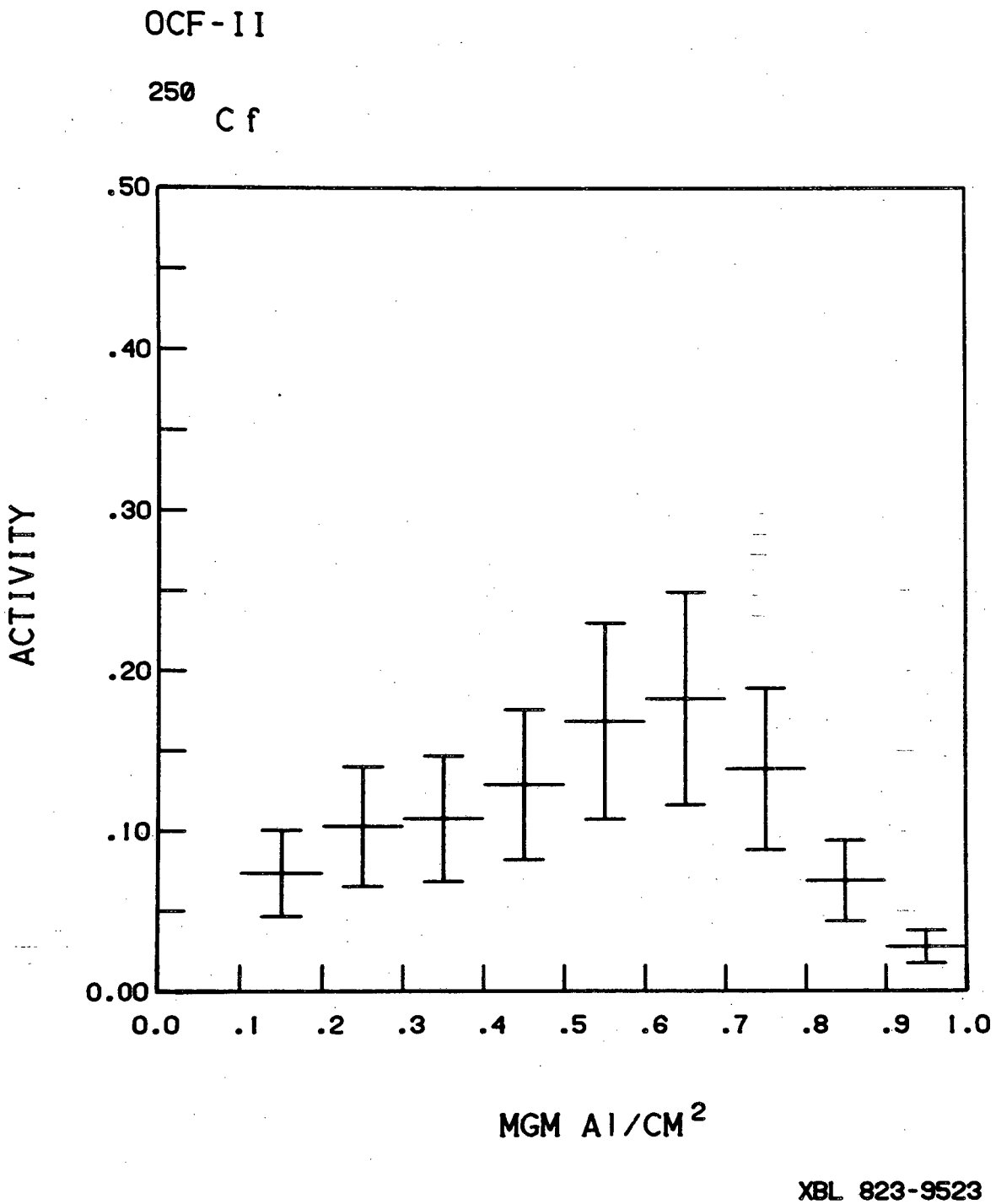
OCF-II
250 Cf
ACTIVITY
.50
.40
.30
.20
.10
0.00
0.0
.1
.2
.3
.4
.5
.6
.7
.8
.9
1.0
MGM Al/CM 2
XBL 823-9523

Fig. 13d

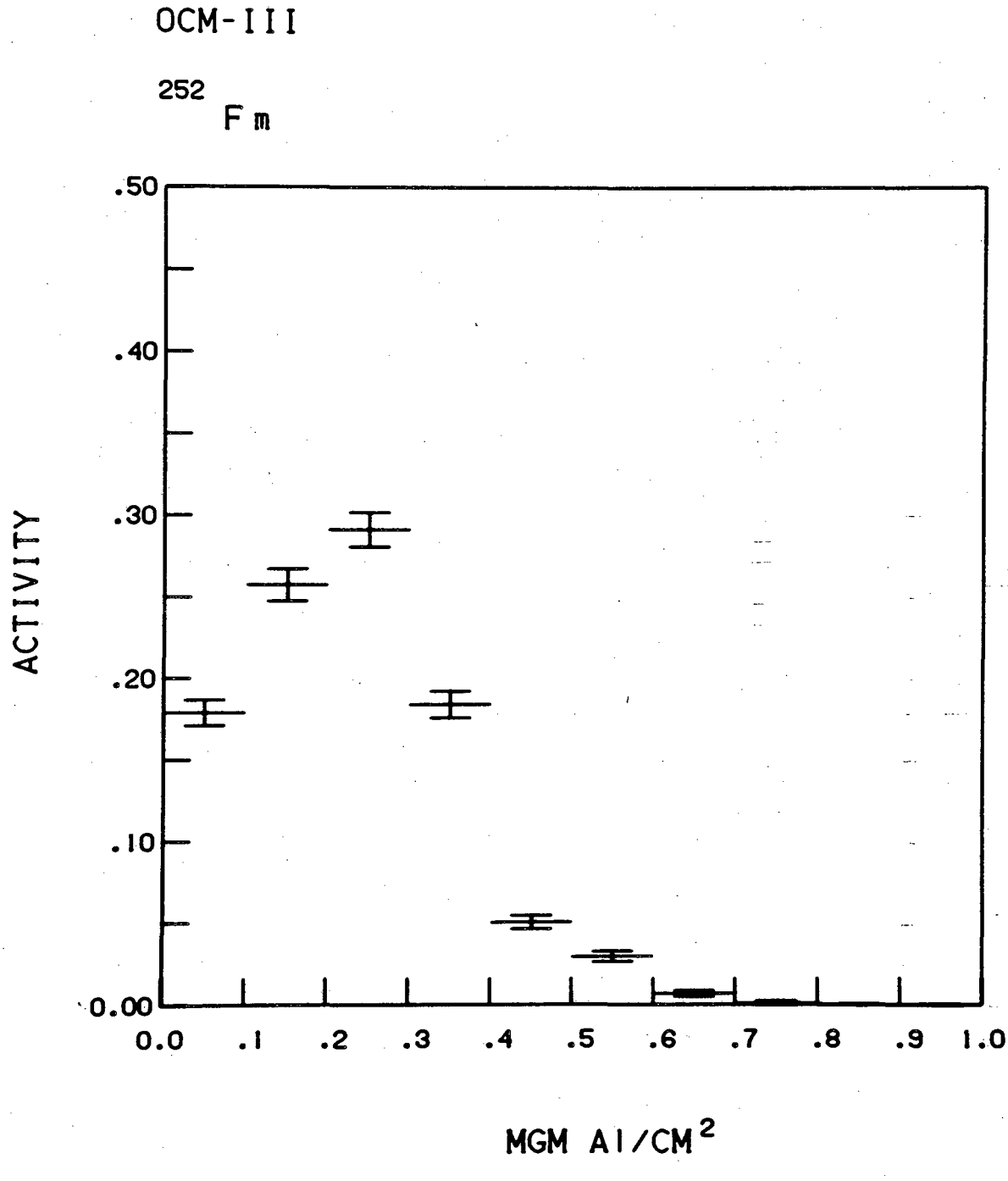
OCM-III
252 Fm
.50
.40
.30
.20
.10
0.00
ACTIVITY
0.0
.1
.2
.3
.4
.5
.6
.7
.8
.9
1.0
MGM Al/CM 2
XBL 823-9554

Fig. 14

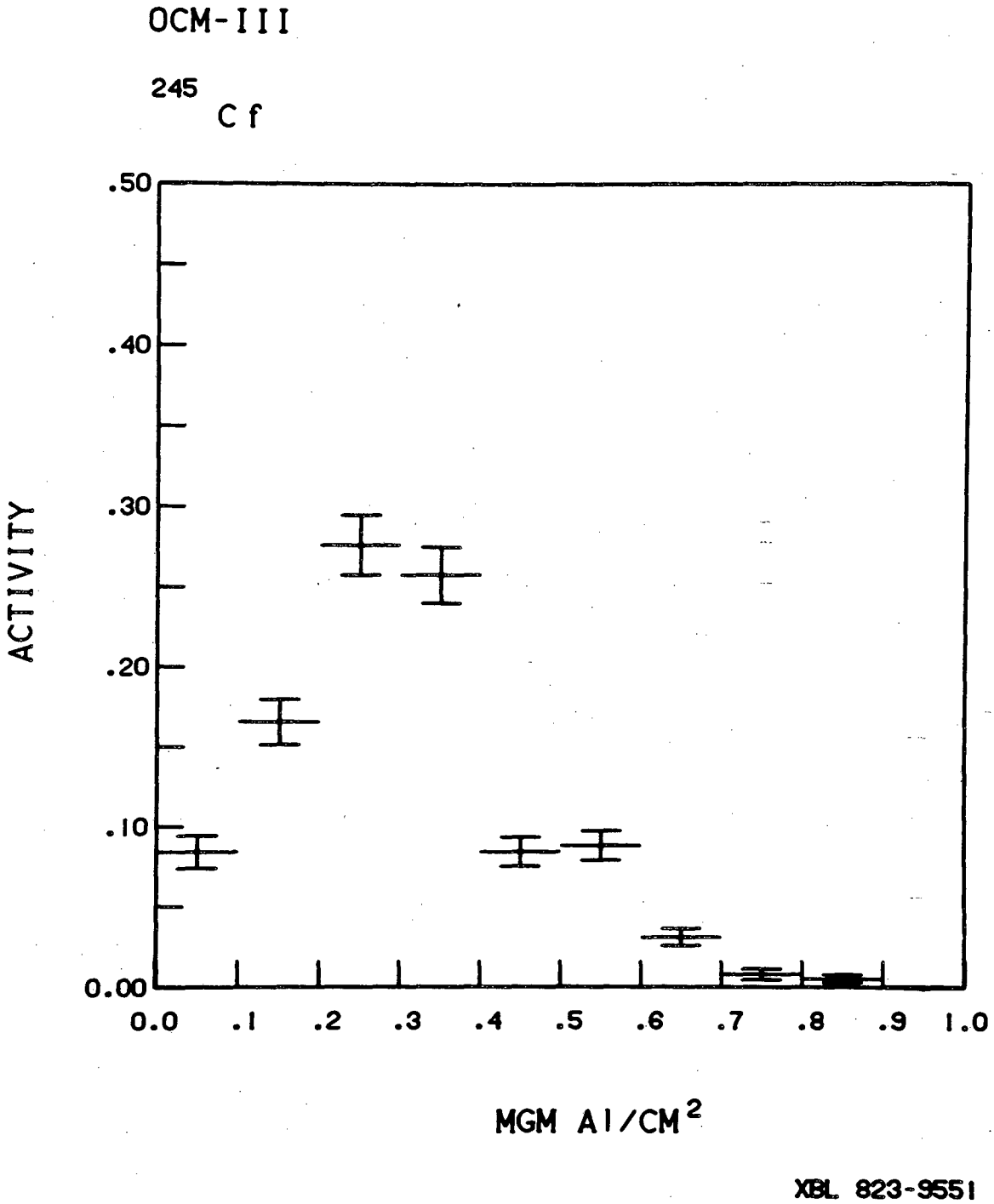
OCM-III
245 Cf
.50
.40
.30
.20
.10
0.00
ACTIVITY
0.0
.1
.2
.3
.4
.5
.6
.7
.8
.9
1.0
MGM Al/CM 2
XBL 823-9551

Fig. 15a

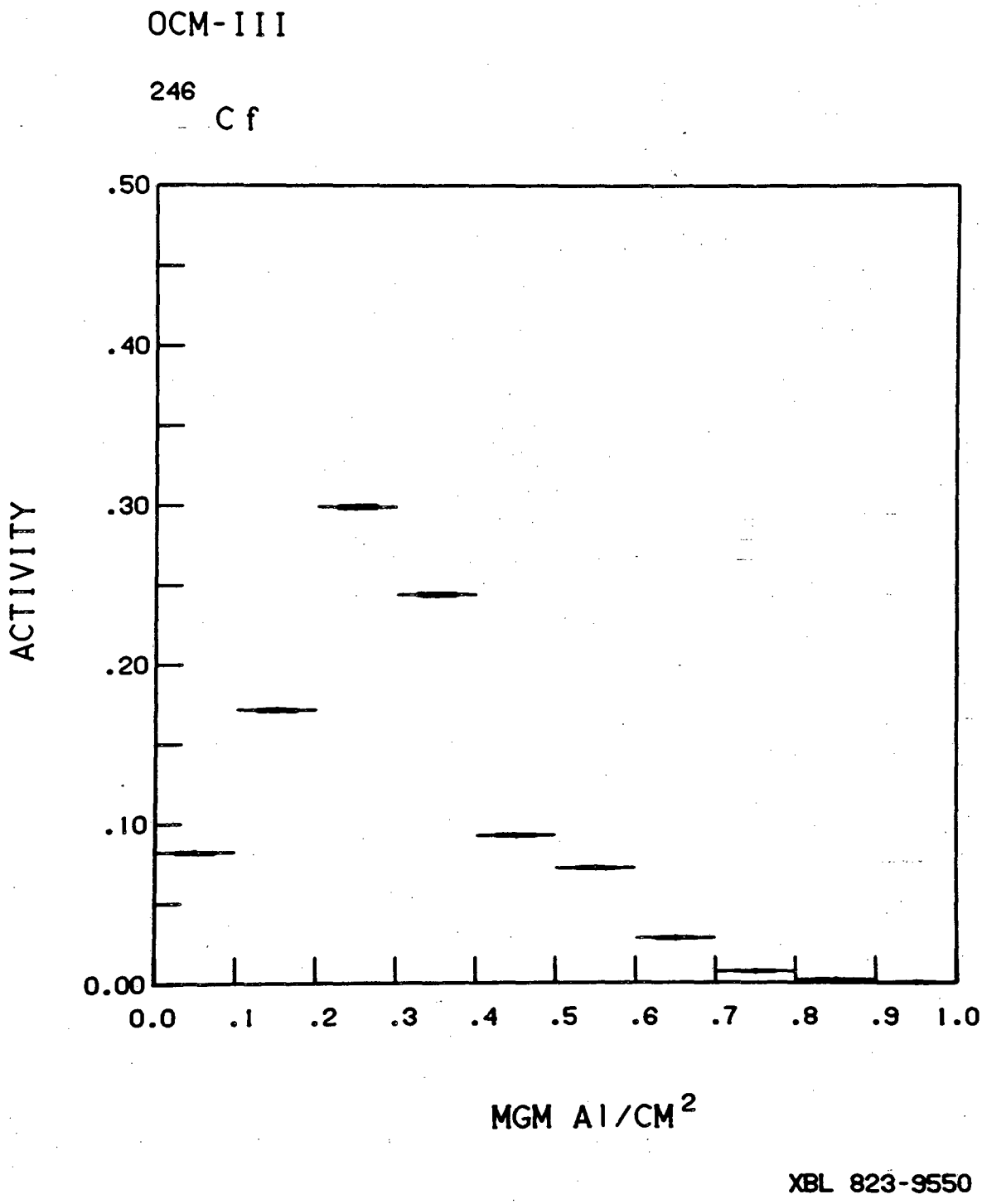
OCM-III
246
Cf
.50
.40
.30
.20
.10
0.00
ACTIVITY
0.0
.1
.2
.3
.4
.5
.6
.7
.8
.9
1.0
MGM Al/CM 2
XBL 823-9550

Fig. 15b

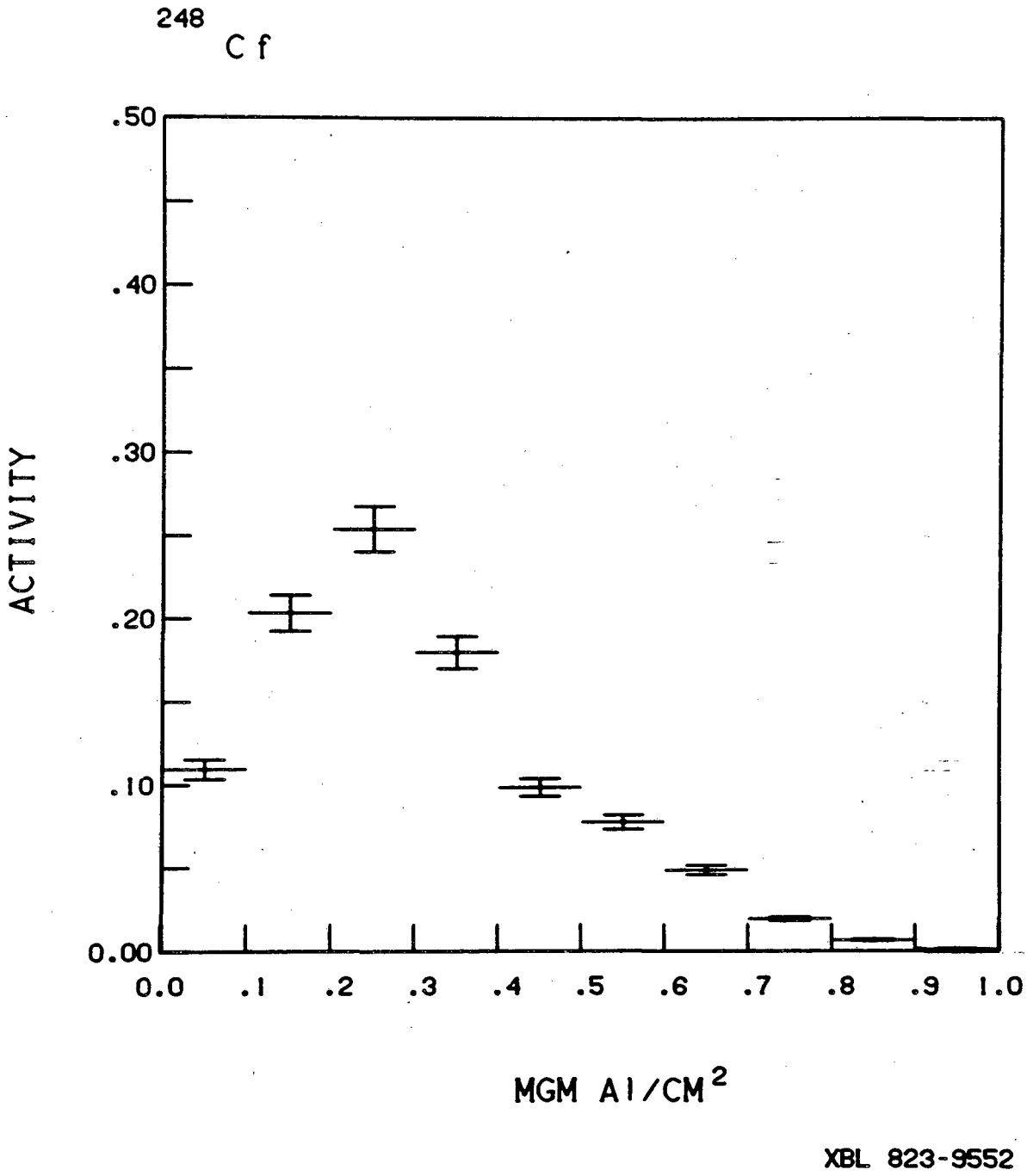
248
Cf
.50
.40
.30
.20
.10
0.00
ACTIVITY
0.0
.1
.2
.3
.4
.5
.6
.7
.8
.9
1.0
MGM Al/CM 2
XBL 823-9552

Fig. 15c

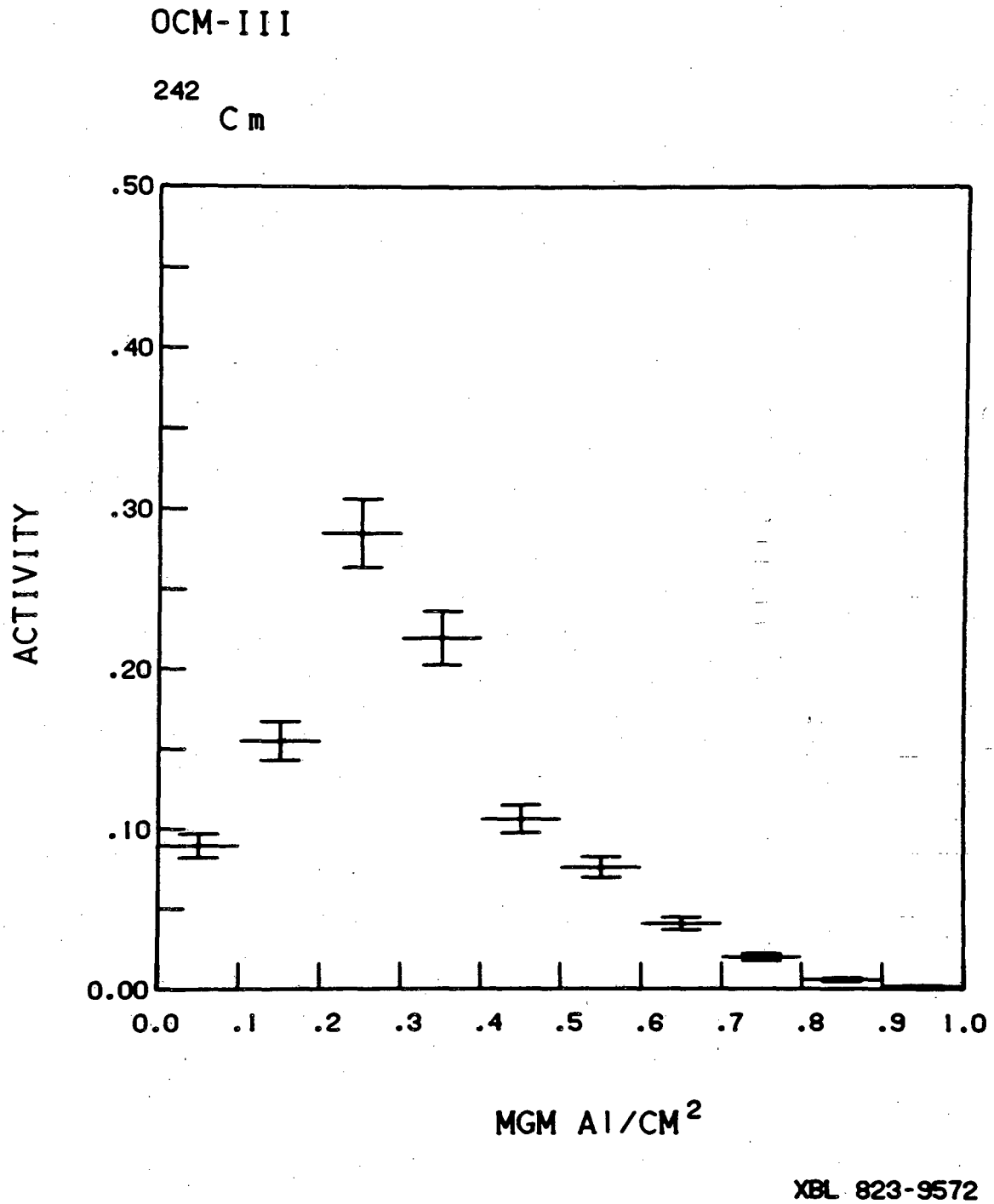
OCM-III
242
Cm
ACTIVITY
.50
.40
.30
.20
.10
0.00
0.0
.1
.2
.3
.4
.5
.6
.7
.8
.9
1.0
MGM Al/CM2
XBL 823-9572

Fig. 16a

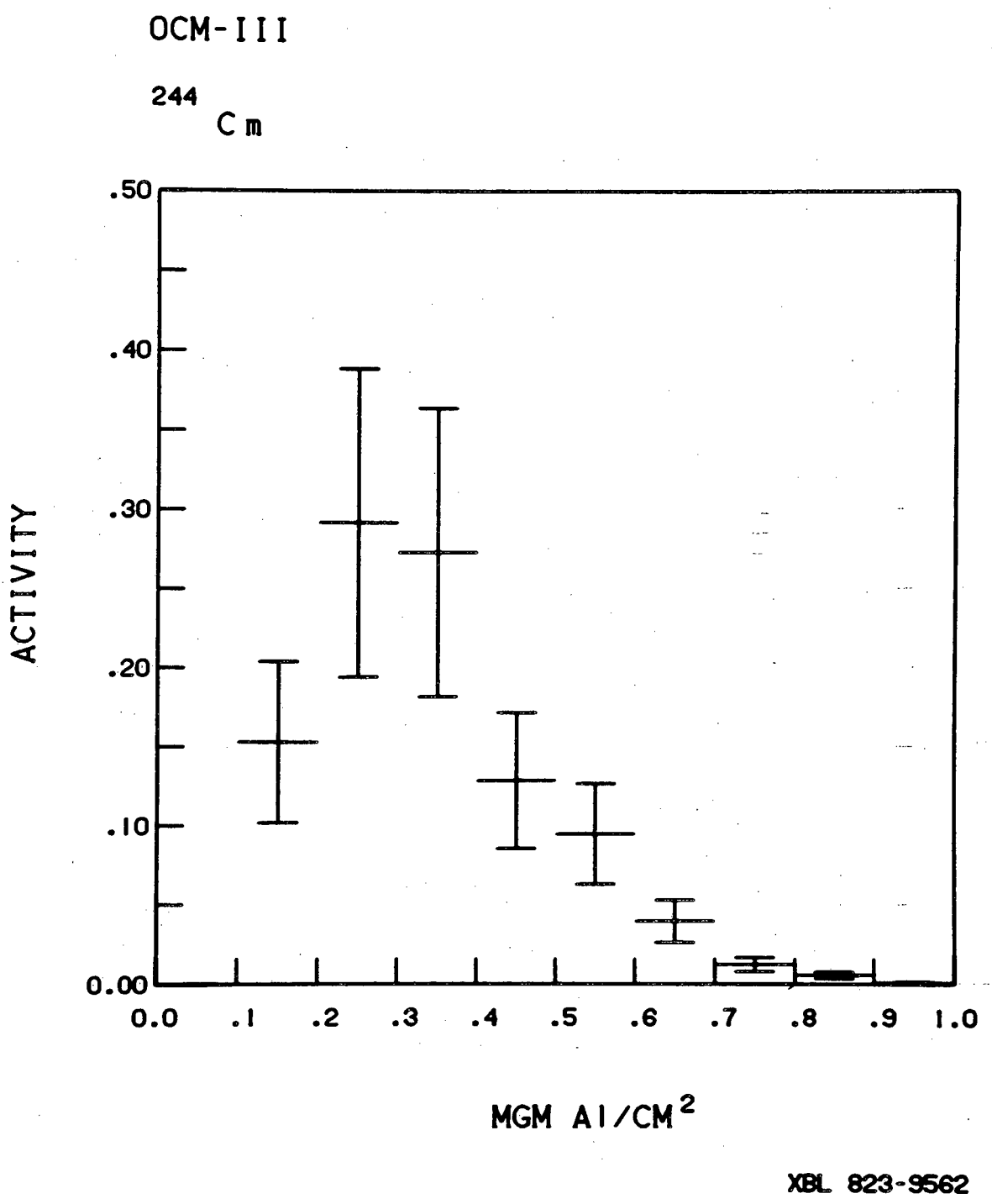
OCM-III
244 Cm
ACTIVITY
.50
.40
.30
.20
.10
0.00
0.0
.1
.2
.3
.4
.5
.6
.7
.8
.9
1.0
MGM Al/CM 2
XBL 823-9562

Fig. 16b

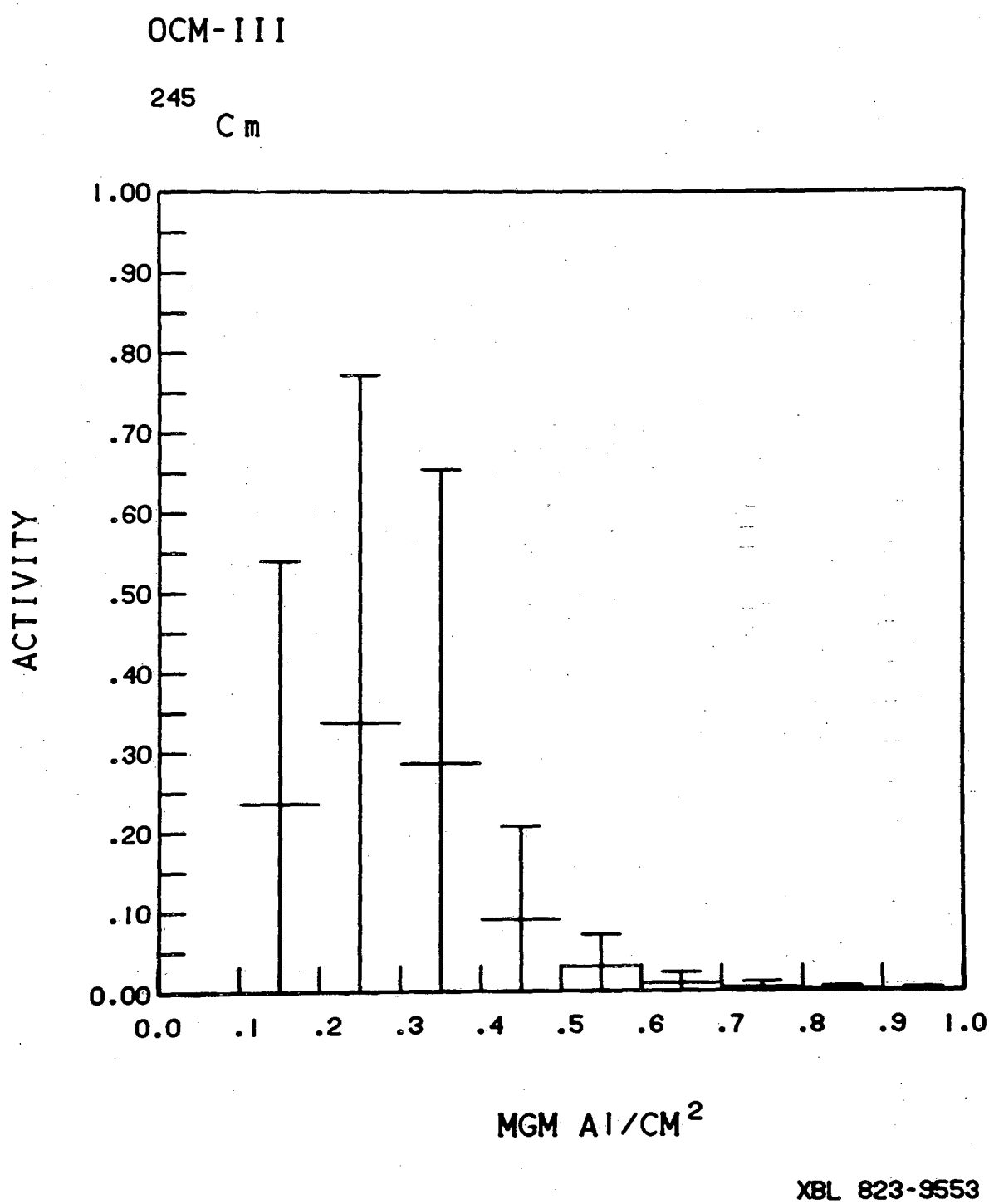
OCM-III
245
Cm
ACTIVITY
1.00
.90
.80
.70
.60
.50
.40
.30
.20
.10
0.00
0.0
.1
.2
.3
.4
.5
.6
.7
.8
.9
1.0
MGM Al/CM2
XBL 823-9553

Fig. 16c

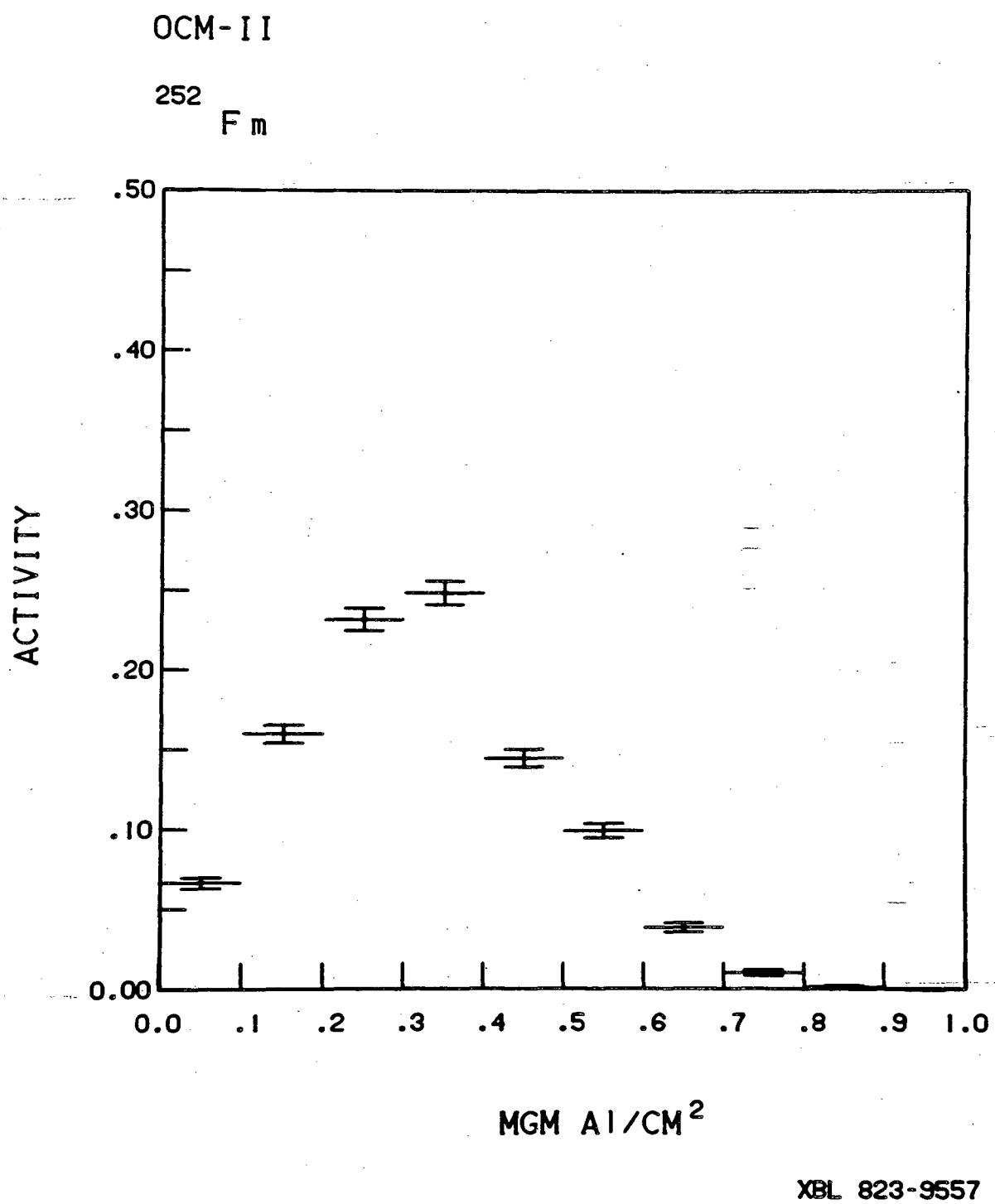
OCM-II
252 Fm
ACTIVITY
.50
.40
.30
.20
.10
0.00
0.0
.1
.2
.3
.4
.5
.6
.7
.8
.9
1.0
MGM Al/CM2
XBL 823-9557

Fig. 17

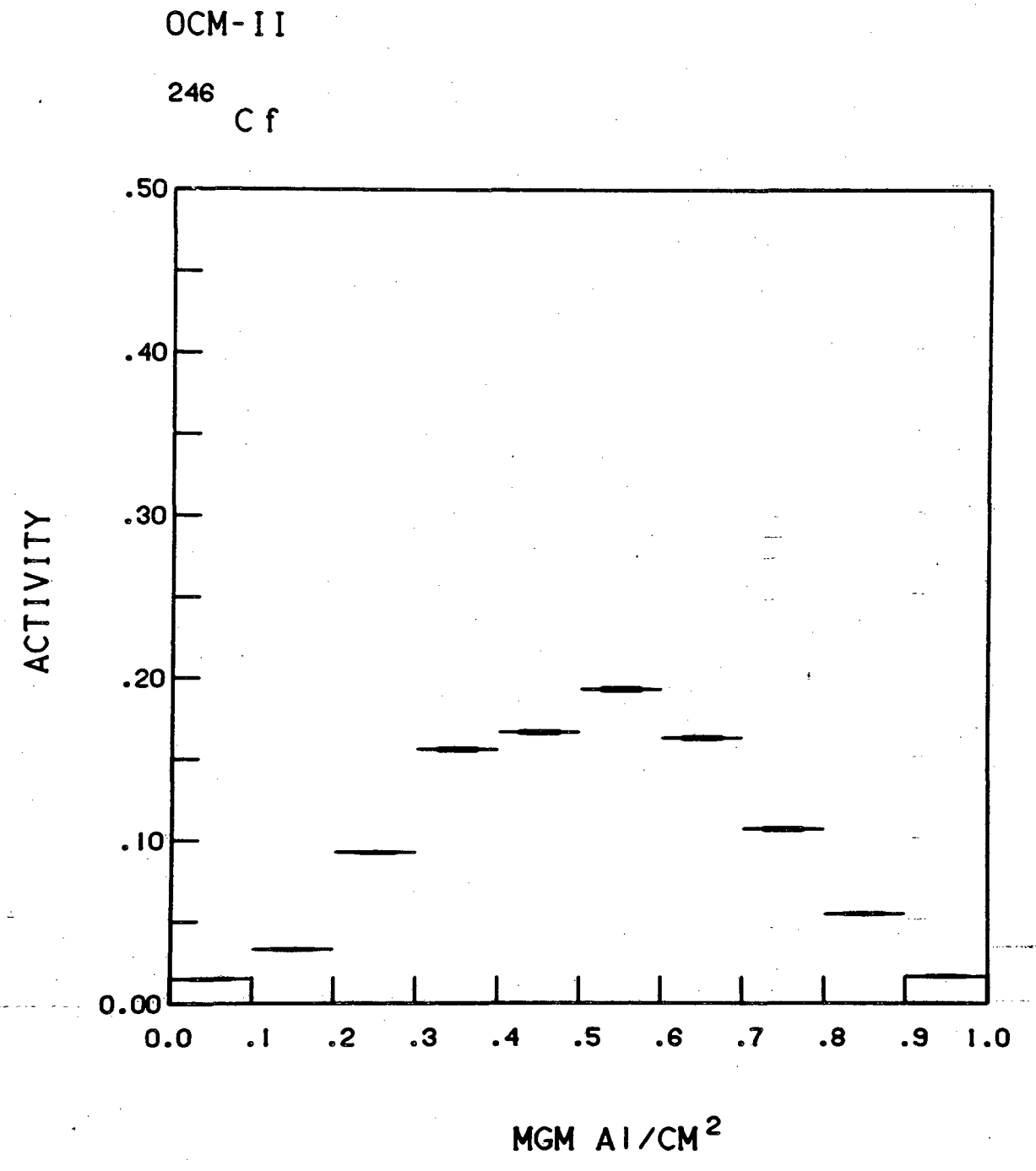
OCM-II
246 Cf
ACTIVITY
.50
.40
.30
.20
.10
0.00
0.0
.1
.2
.3
.4
.5
.6
.7
.8
.9
1.0
MGM Al/CM 2
XBL 823-9555

Fig. 18a

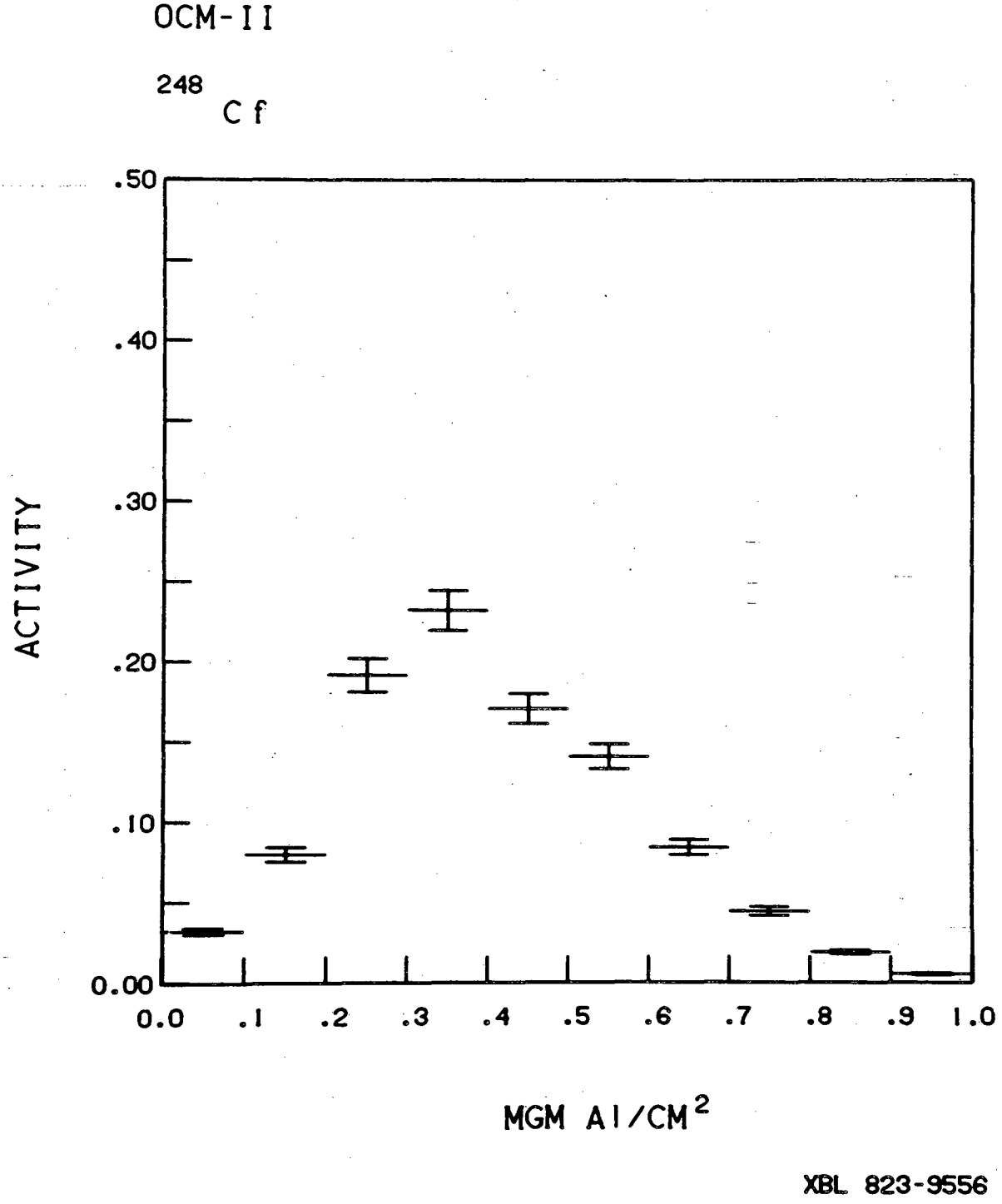
OCM-II
248 Cf
ACTIVITY
.50
.40
.30
.20
.10
0.00
0.0
.1
.2
.3
.4
.5
.6
.7
.8
.9
1.0
MGM Al/CM2
XBL 823-9556

Fig. 18b

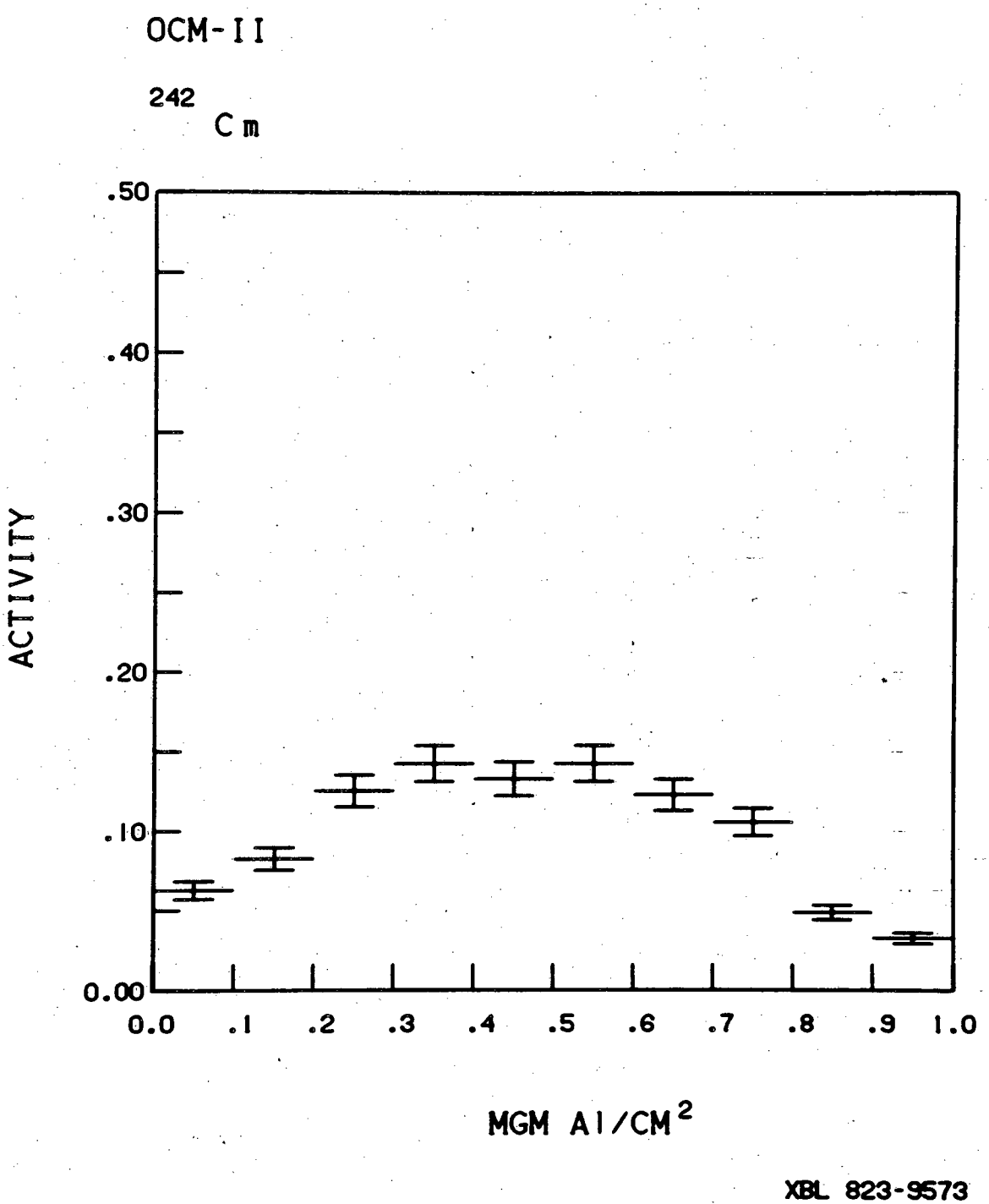
OCM-II
242
Cm
.50
.40
.30
.20
.10
0.00
ACTIVITY
0.0
.1
.2
.3
.4
.5
.6
.7
.8
.9
1.0
MGM Al/CM 2
XBL 823-9573

Fig. 19a

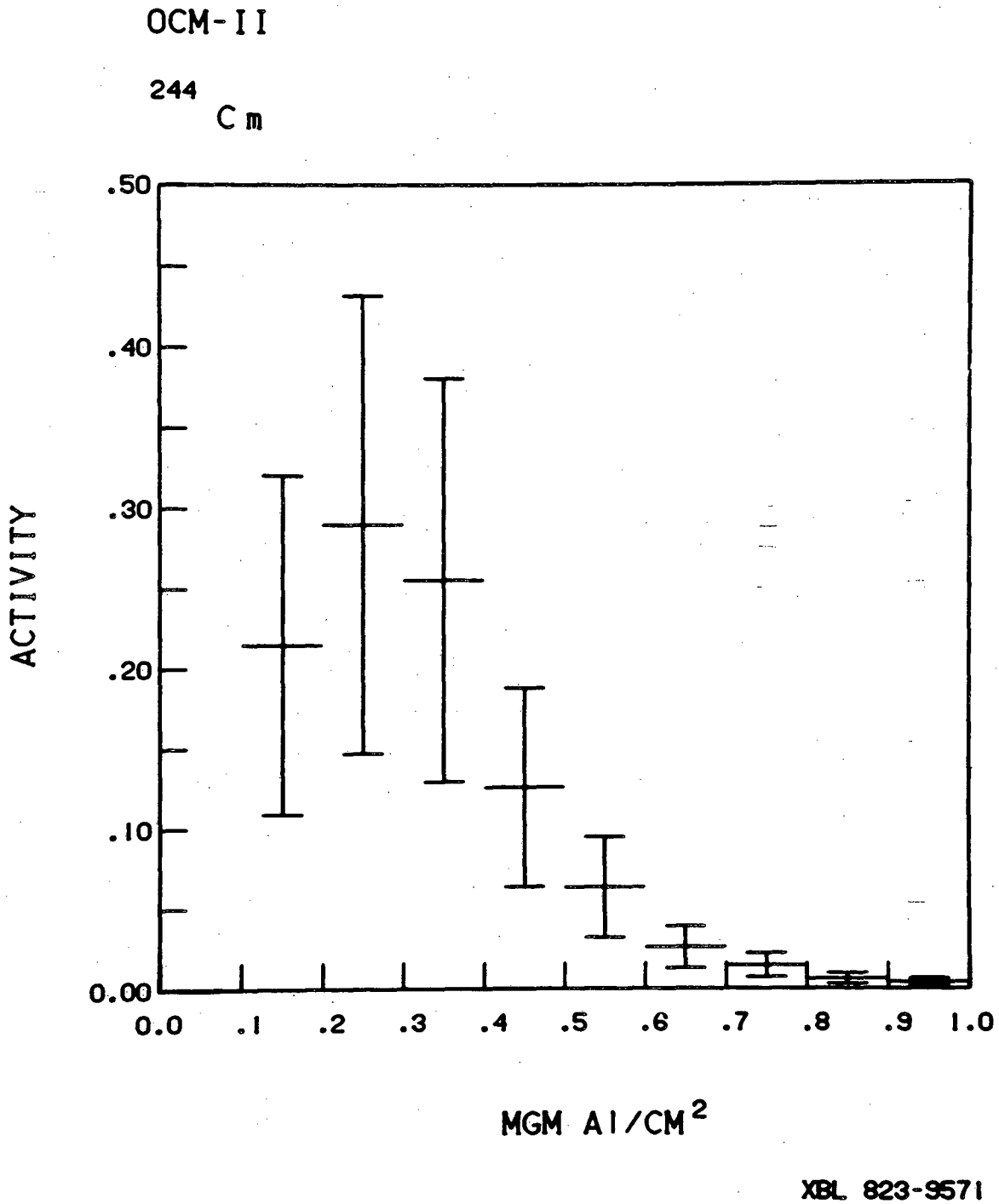
OCM-II
244 Cm
.50
.40
.30
.20
.10
0.00
ACTIVITY
0.0
.1
.2
.3
.4
.5
.6
.7
.8
.9
1.0
MGM Al/CM 2
XBL 823-9571

Fig. 19b

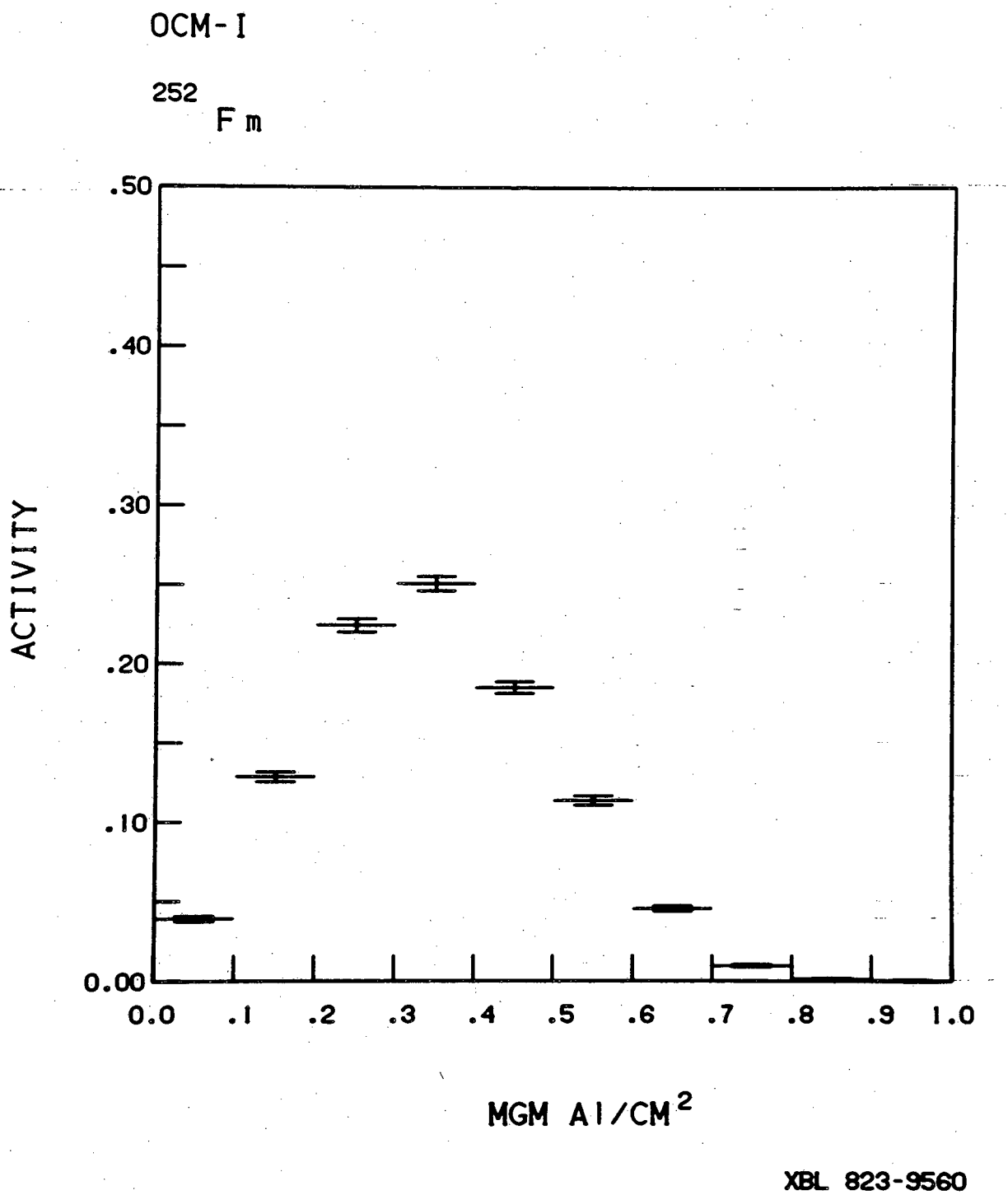
OCM-I
252
Fm
.50
.40
.30
.20
.10
0.00
ACTIVITY
0.0
.1
.2
.3
.4
.5
.6
.7
.8
.9
1.0
MGM Al/CM2
XBL 823-9560

Fig. 20

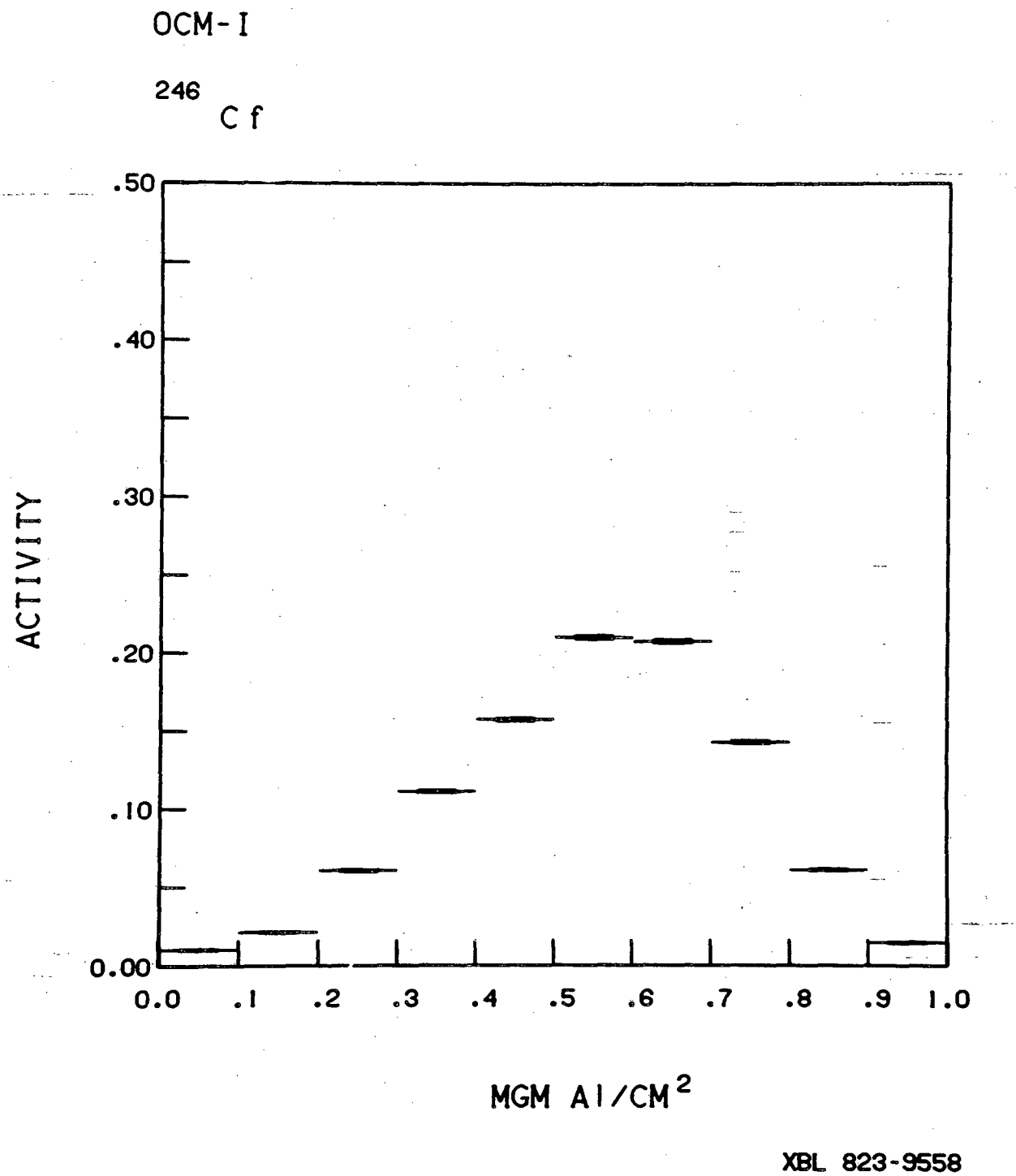
OCM-I
246 Cf
.50
.40
.30
.20
.10
0.00
ACTIVITY
0.0
.1
.2
.3
.4
.5
.6
.7
.8
.9
1.0
MGM Al/CM 2
XBL 823-9558

Fig. 21a

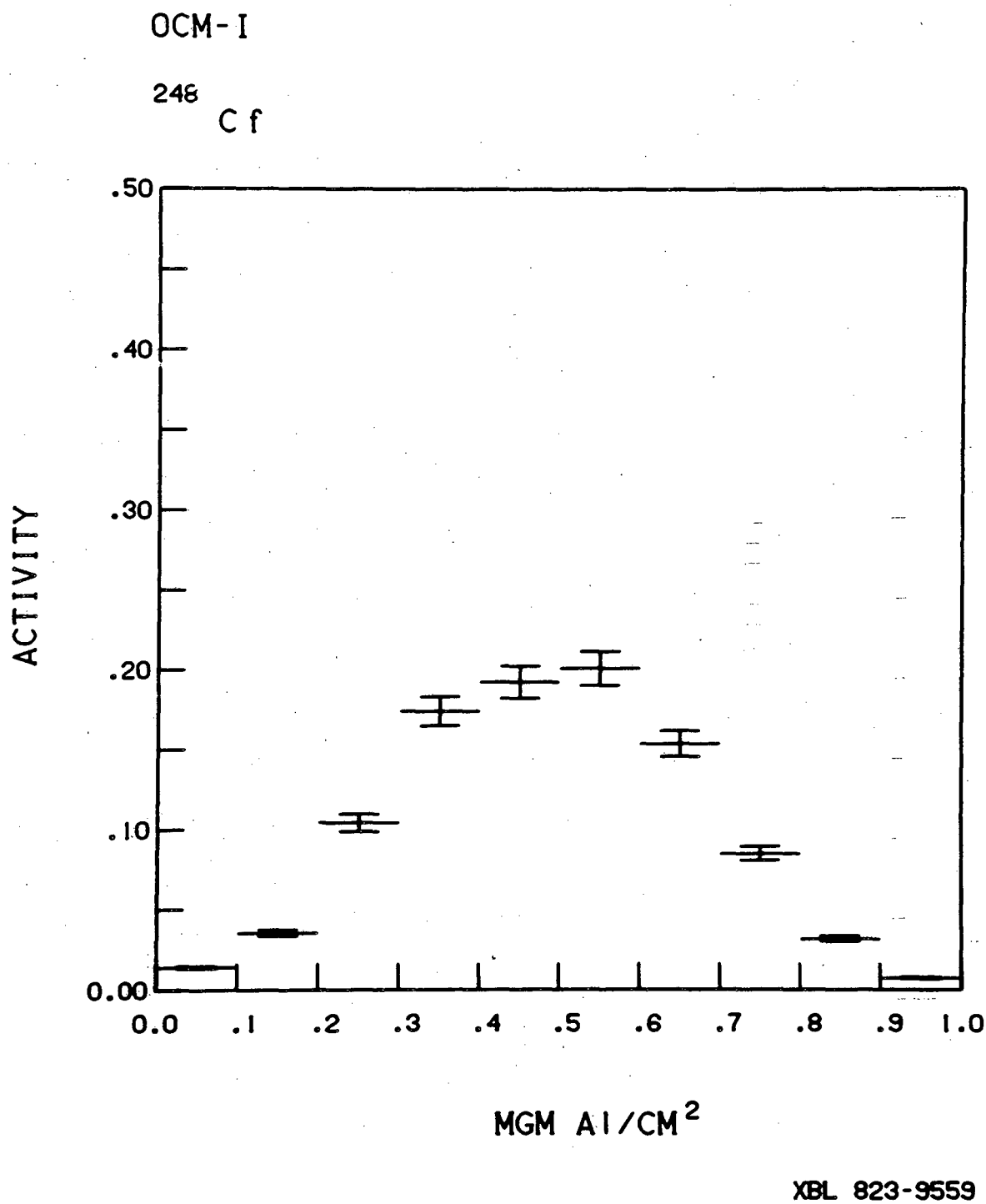
OCM-I
248 Cf
ACTIVITY
.50
.40
.30
.20
.10
0.00
0.0
.1
.2
.3
.4
.5
.6
.7
.8
.9
1.0
MGM Al/CM2
XBL 823-9559

Fig. 21b

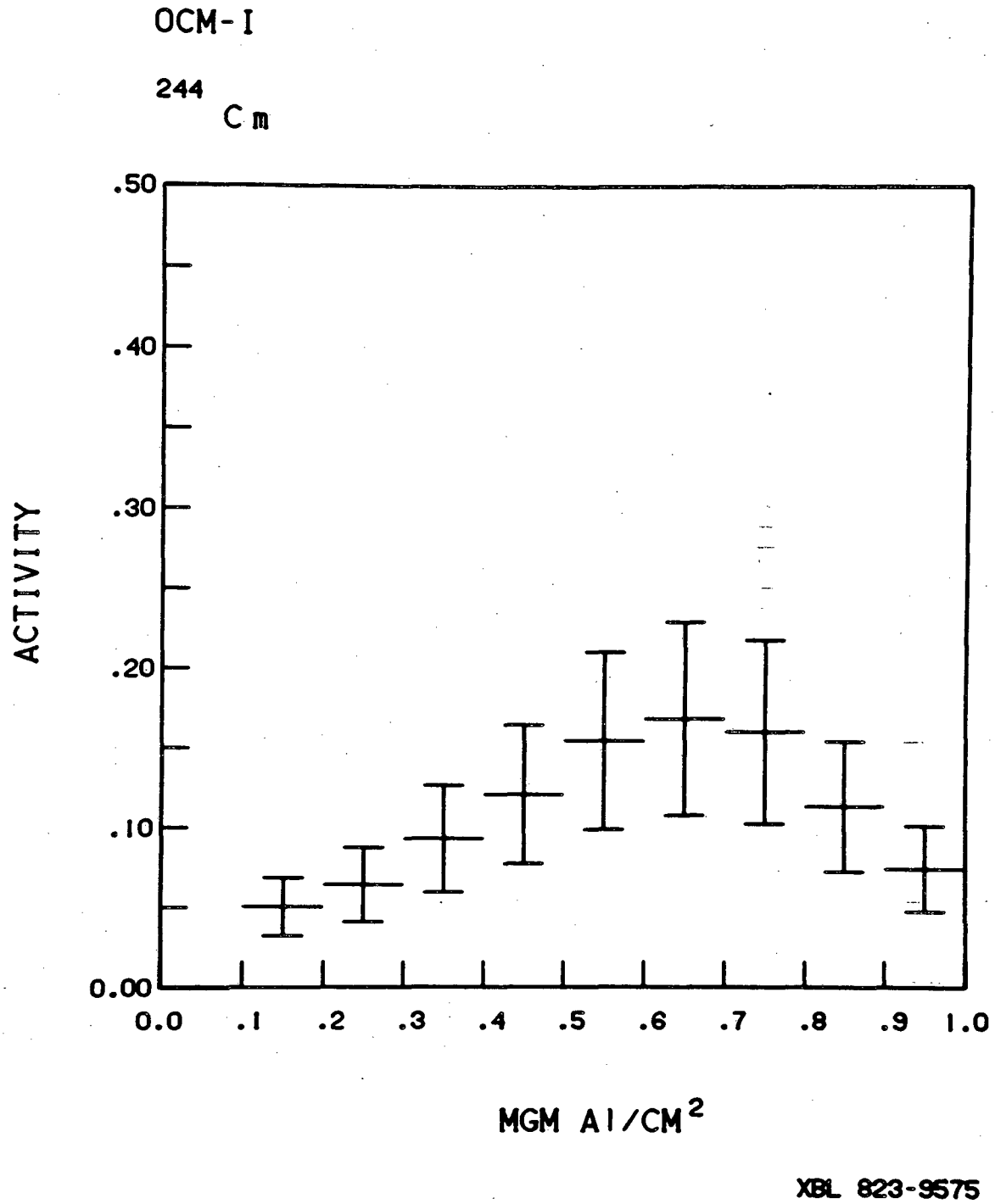
OCM-I
244 Cm
ACTIVITY
.50
.40
.30
.20
.10
0.00
0.0
.1
.2
.3
.4
.5
.6
.7
.8
.9
1.0
MGM Al/CM2
XBL 823-9575

Fig. 22a

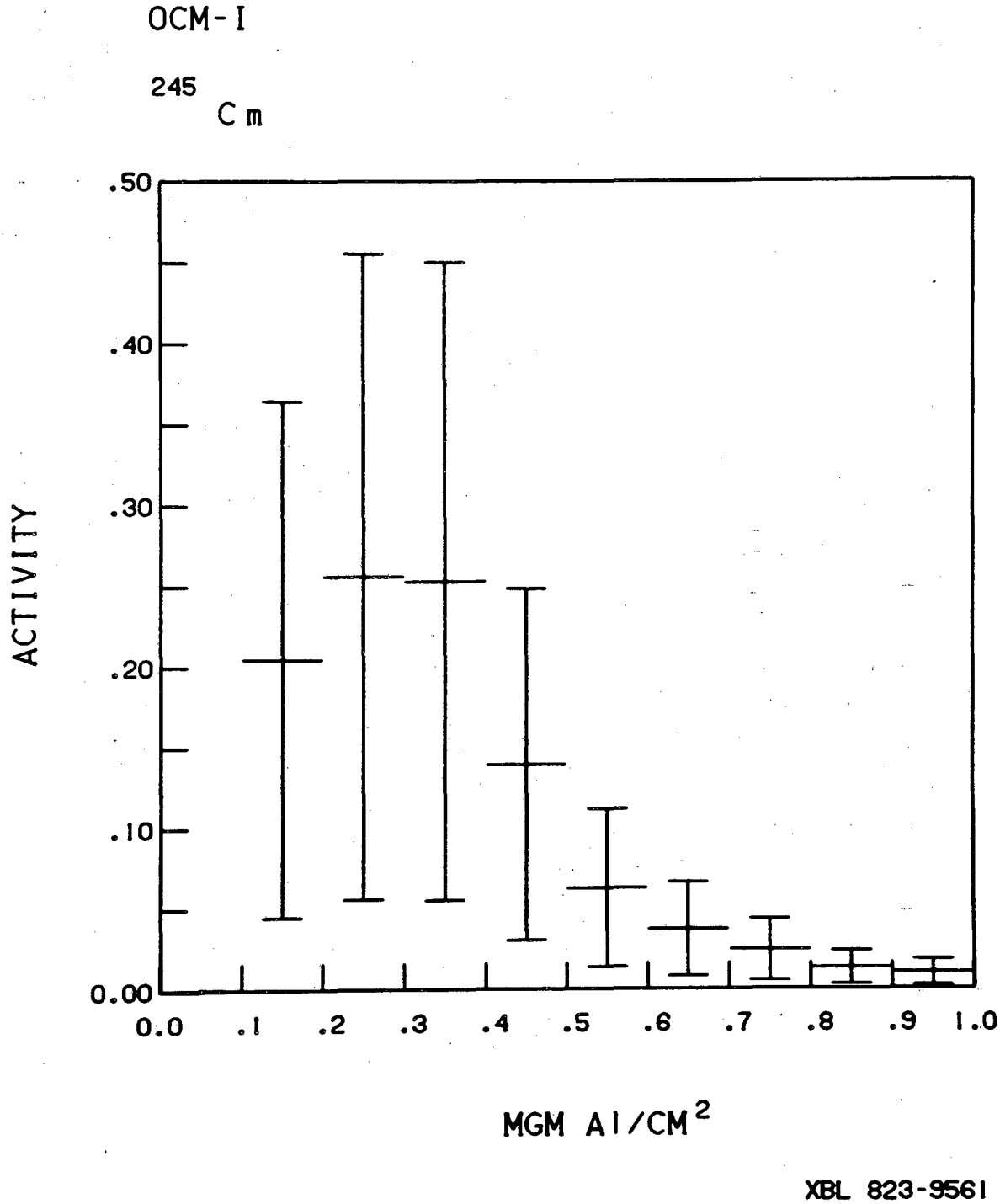
OCM-I
245 Cm
.50
.40
.30
.20
.10
0.00
ACTIVITY
0.0
.1
.2
.3
.4
.5
.6
.7
.8
.9
1.0
MGM Al/CM 2
XBL 823-9561

Fig. 22b

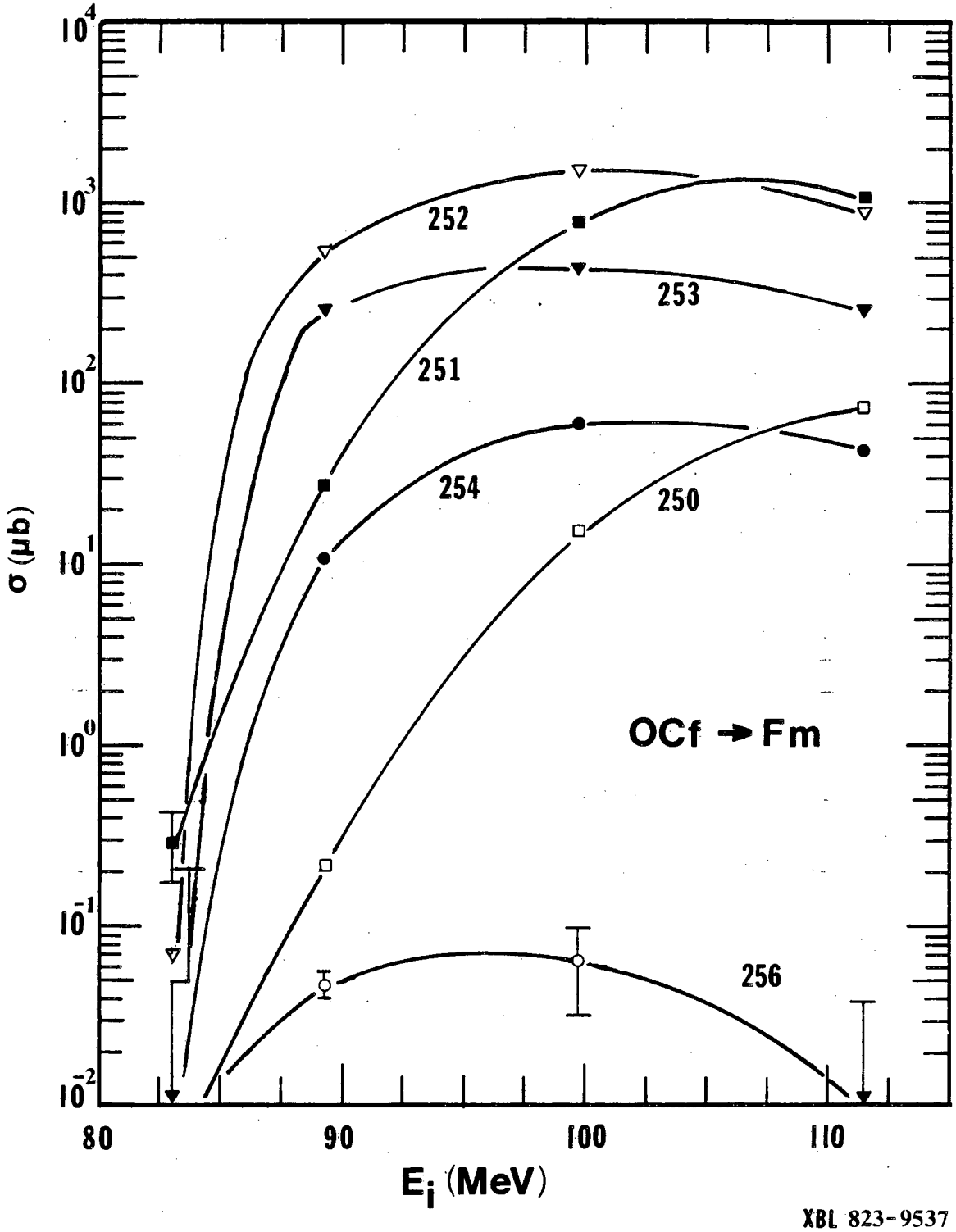
σ (μb)
10^4
10^3
10^2
10^1
10^0
10^{-1}
10^{-2}
252
253
251
254
250
256
OCf → Fm
80
90
100
110
E_i (MeV)
XBL 823-9537

Fig. 23

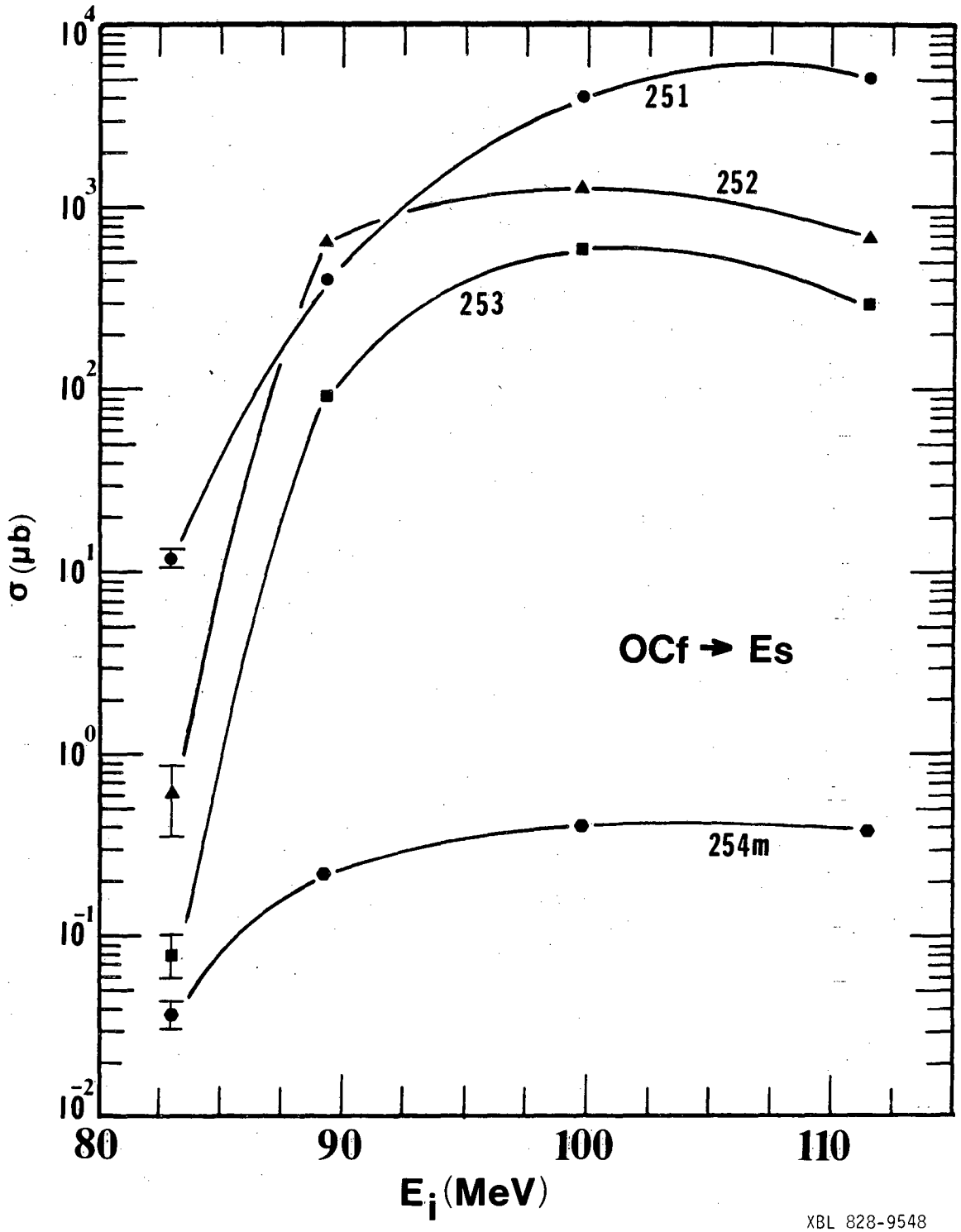
10^4
10^3
10^2
10^1
10^0
10^{-1}
10^{-2}
σ (μb)
251
252
253
254m
OCf → Es
80
90
100
110
E_i (MeV)
XBL 828-9548

Fig. 24

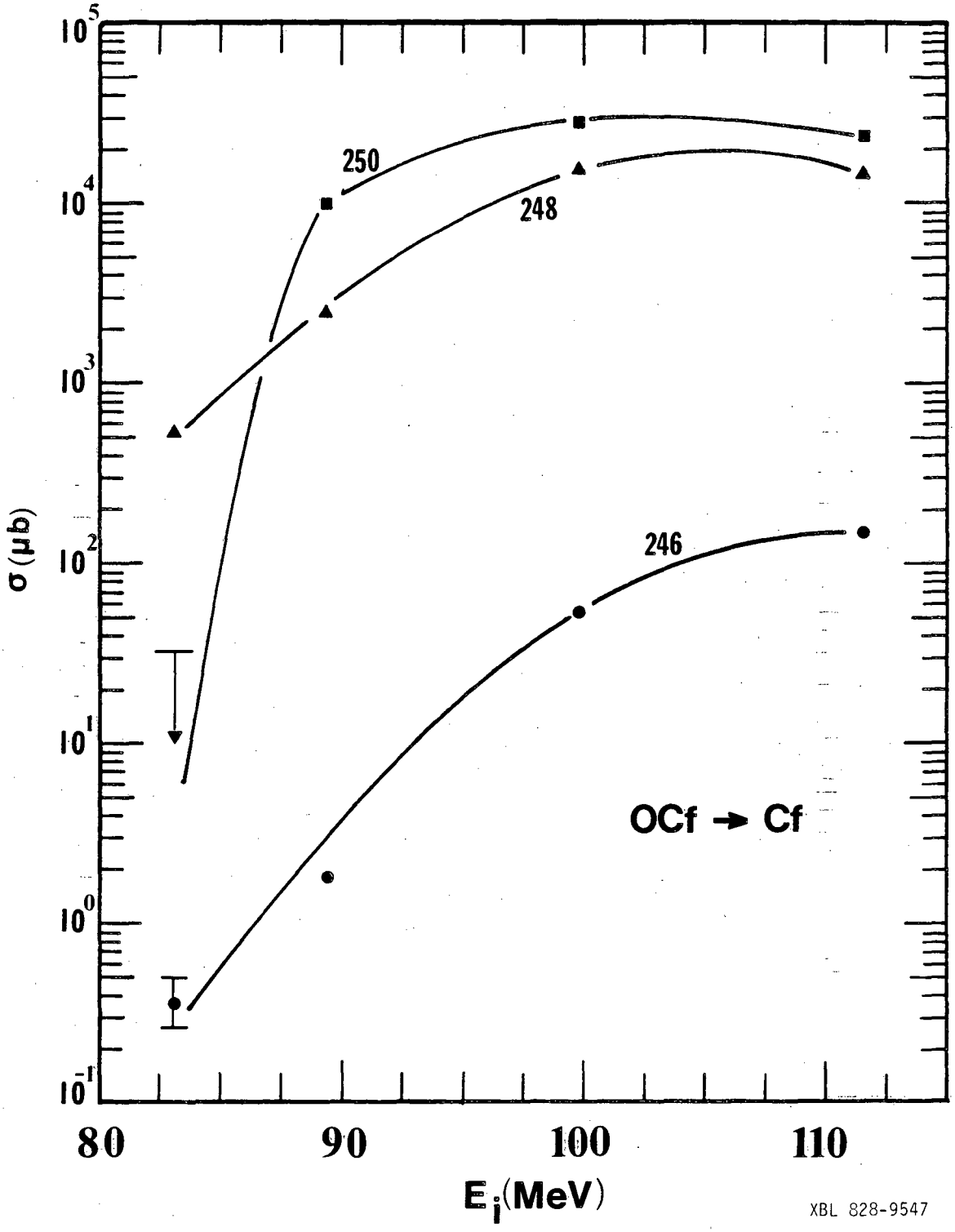
10^5
10^4
10^3
10^2
10^1
10^0
10^{-1}
σ (μb)
250
248
246
OCf → Cf
80
90
100
110
E_i(MeV)
XBL 828-9547

Fig. 25

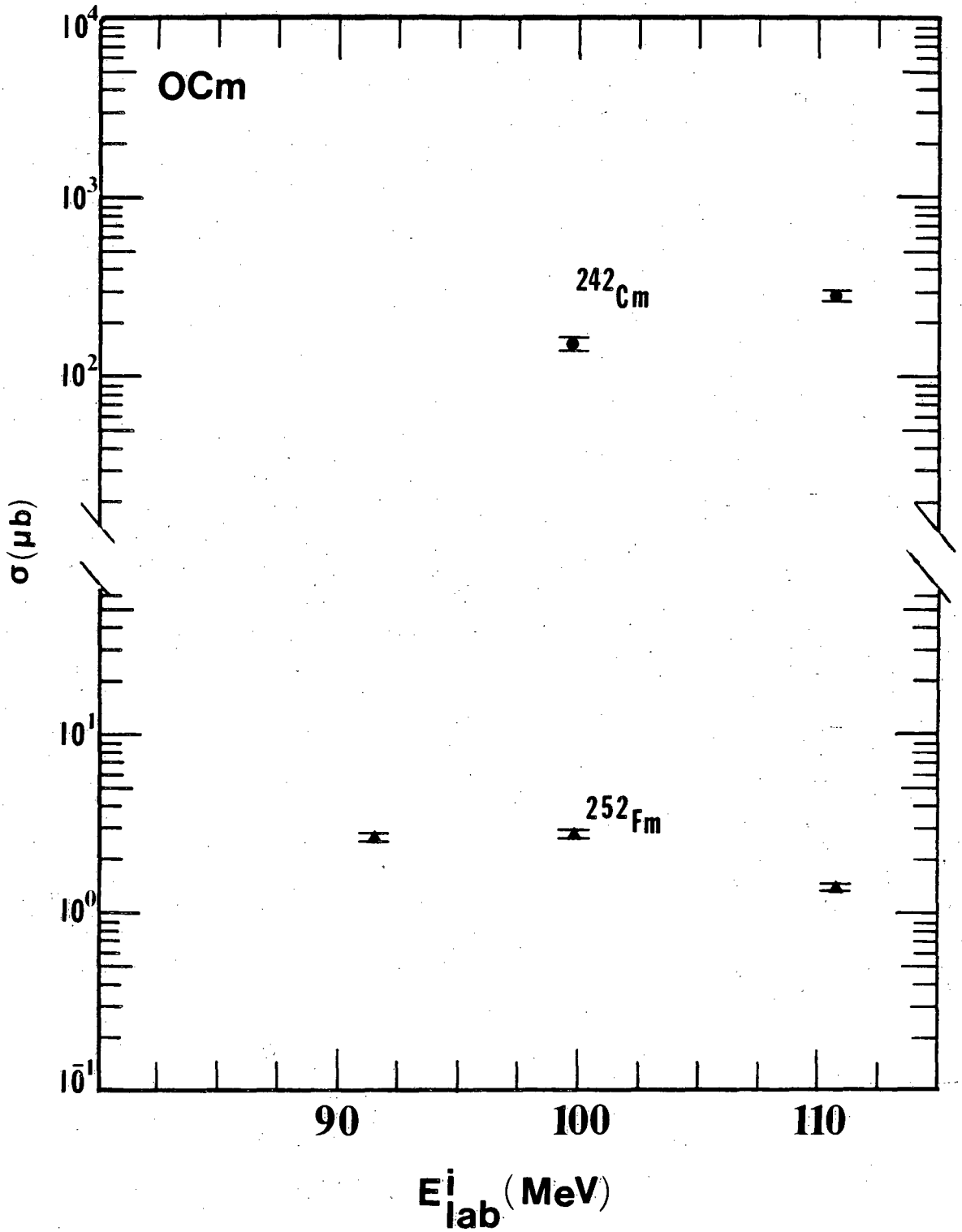
OCm
10^4
10^3
10^2
10^1
10^0
10^{-1}
^{242}Cm
^{252}Fm
σ(μb)
90
100
110
E^i_{lab}(MeV)
XBL 828-9563

Fig. 26

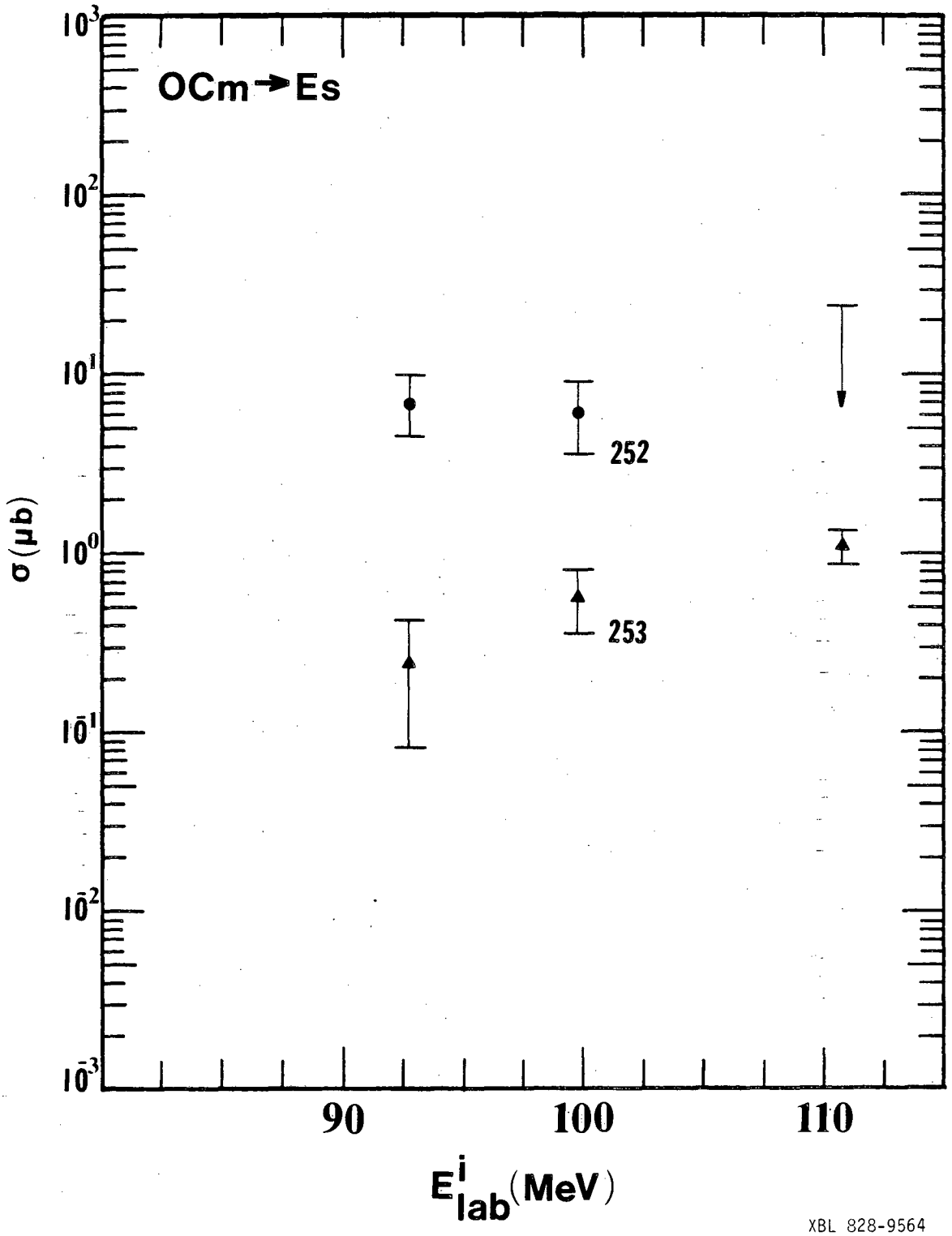
OCm → Es
σ (μb)
10^3
10^2
10^1
10^0
10^{-1}
10^{-2}
10^{-3}
252
253
90
100
110
E^i_{lab}(MeV)
XBL 828-9564

Fig. 27

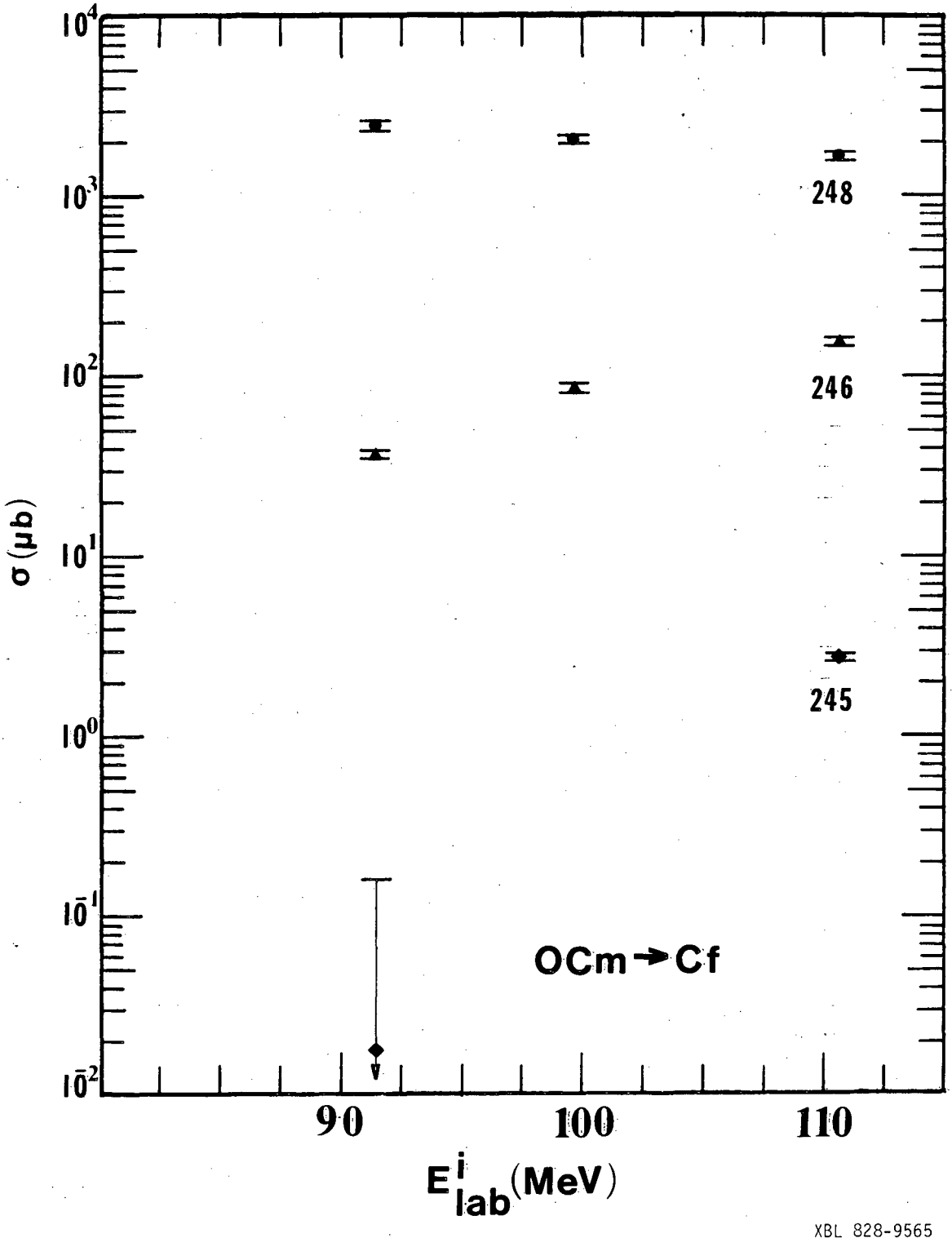
10^4
10^3
10^2
10^1
10^0
10^{-1}
10^{-2}
σ (μb)
248
246
245
OCm→Cf
90
100
110
E^i_{lab}(MeV)
XBL 828-9565

Fig. 28

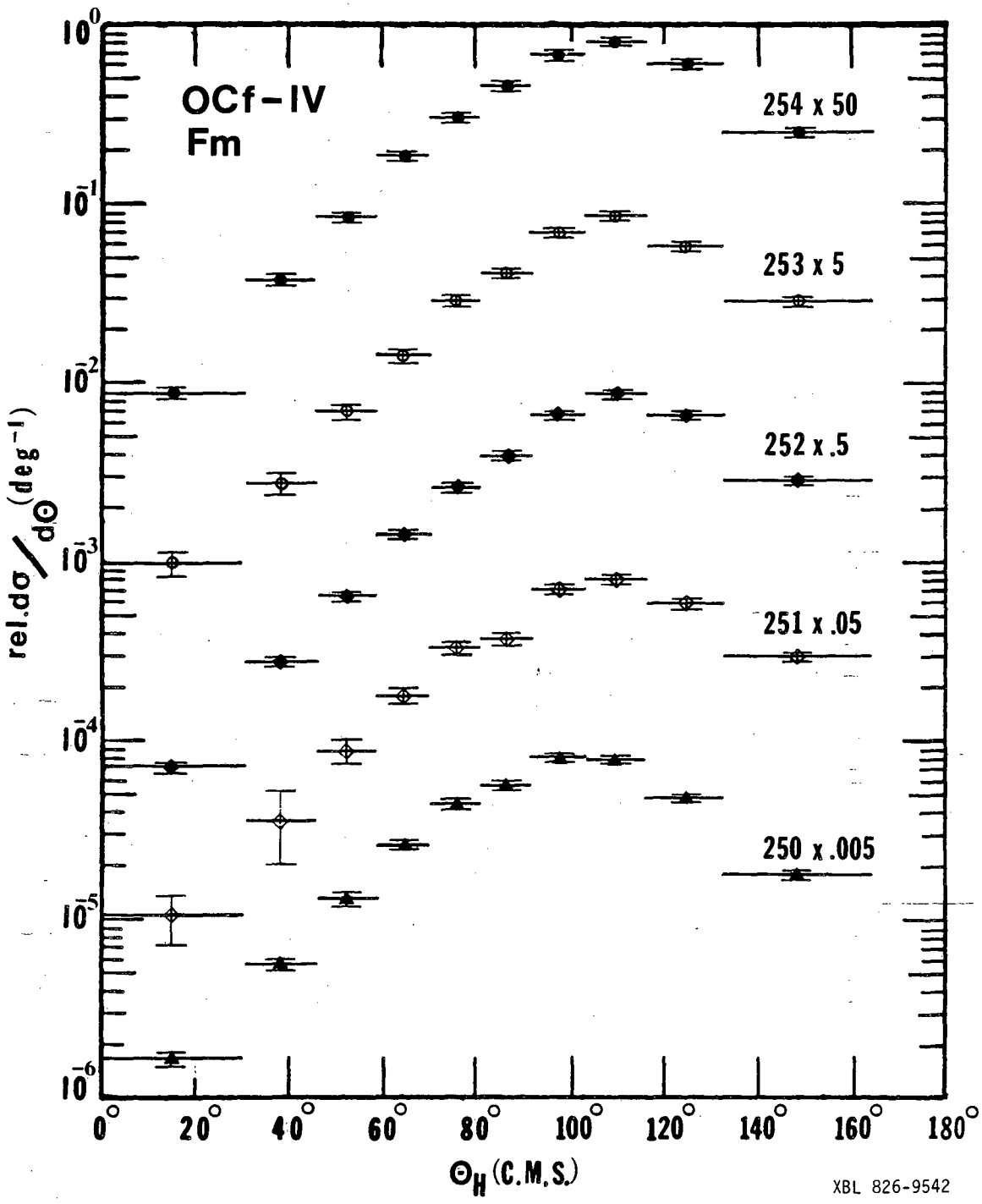
OCf-IV
Fm
254 x 50
253 x 5
252 x .5
251 x .05
250 x .005
rel.dσ/dΩ (deg⁻¹)
10⁰
10⁻¹
10⁻²
10⁻³
10⁻⁴
10⁻⁵
10⁻⁶
0°
20°
40°
60°
80°
100°
120°
140°
160°
180°
Θ_H (C.M.S.)
XBL 826-9542

Fig. 29

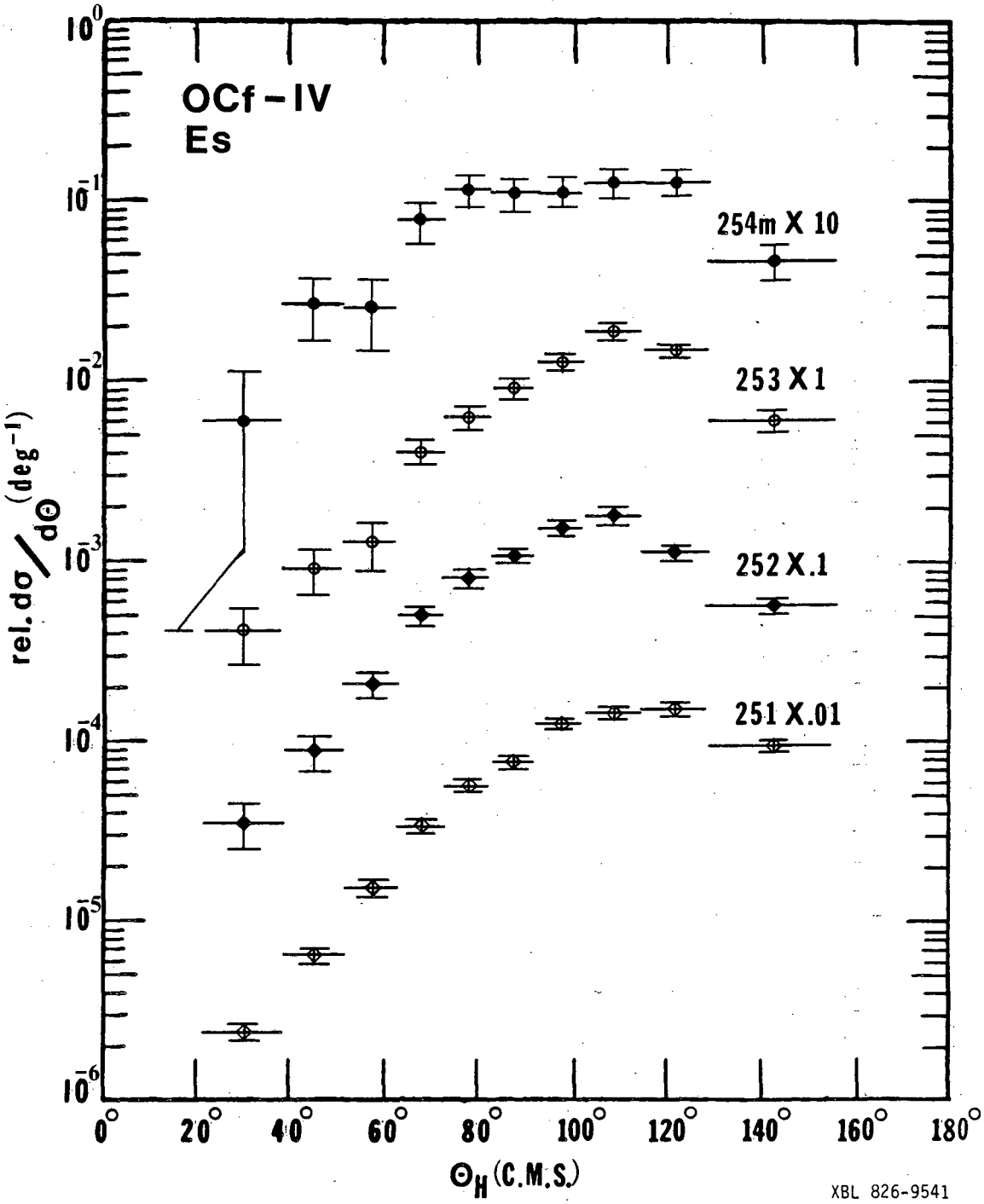
OCf-IV
Es
254m X 10
253 X 1
252 X .1
251 X .01
rel. dσ/dΘ (deg⁻¹)
Θ_H (C.M.S.)
XBL 826-9541

Fig. 30

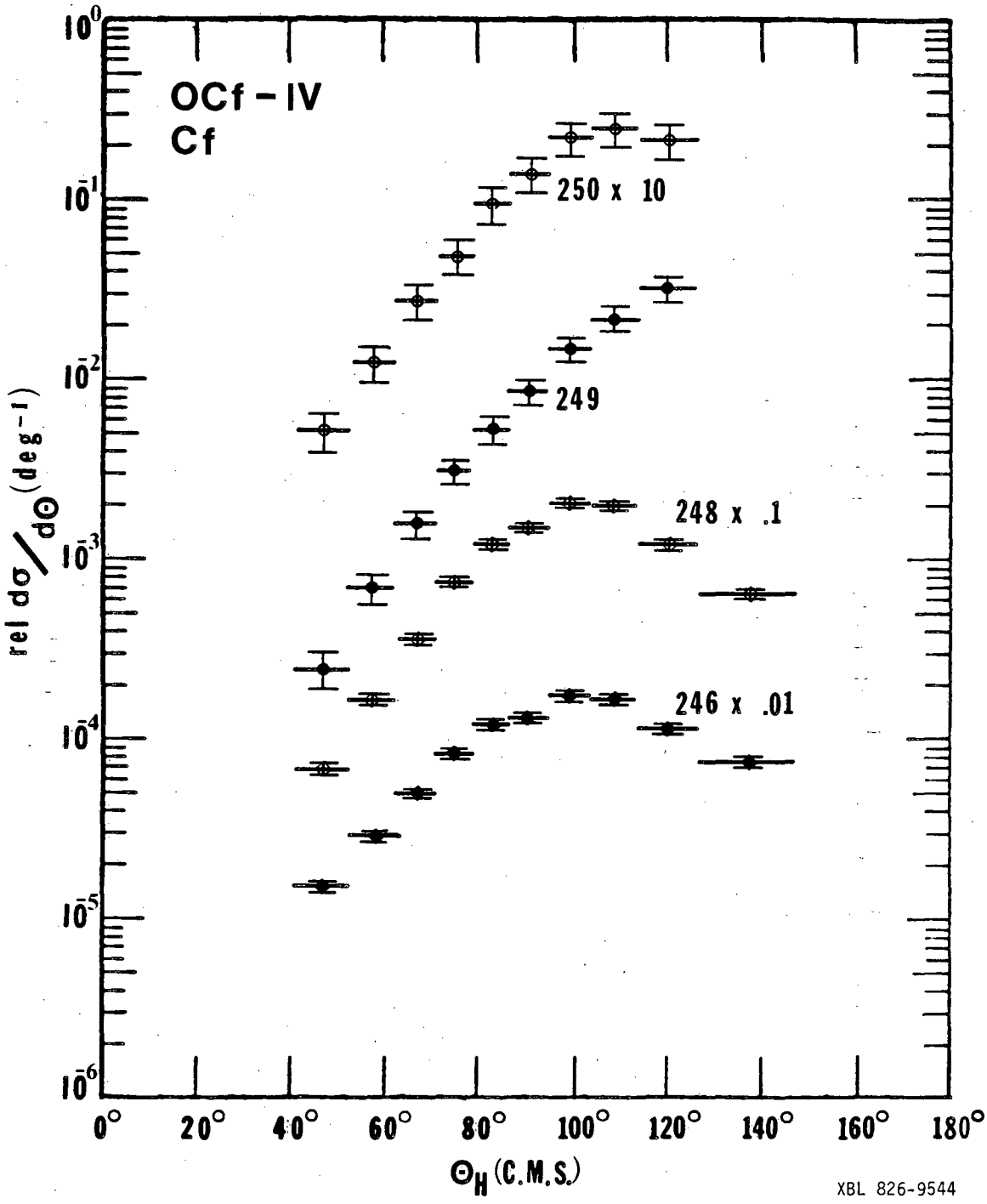
OCf - IV
Cf
250 x 10
249
248 x .1
246 x .01
rel dσ/dΘ (deg⁻¹)
Θ_H (C.M.S.)
XBL 826-9544

Fig. 31

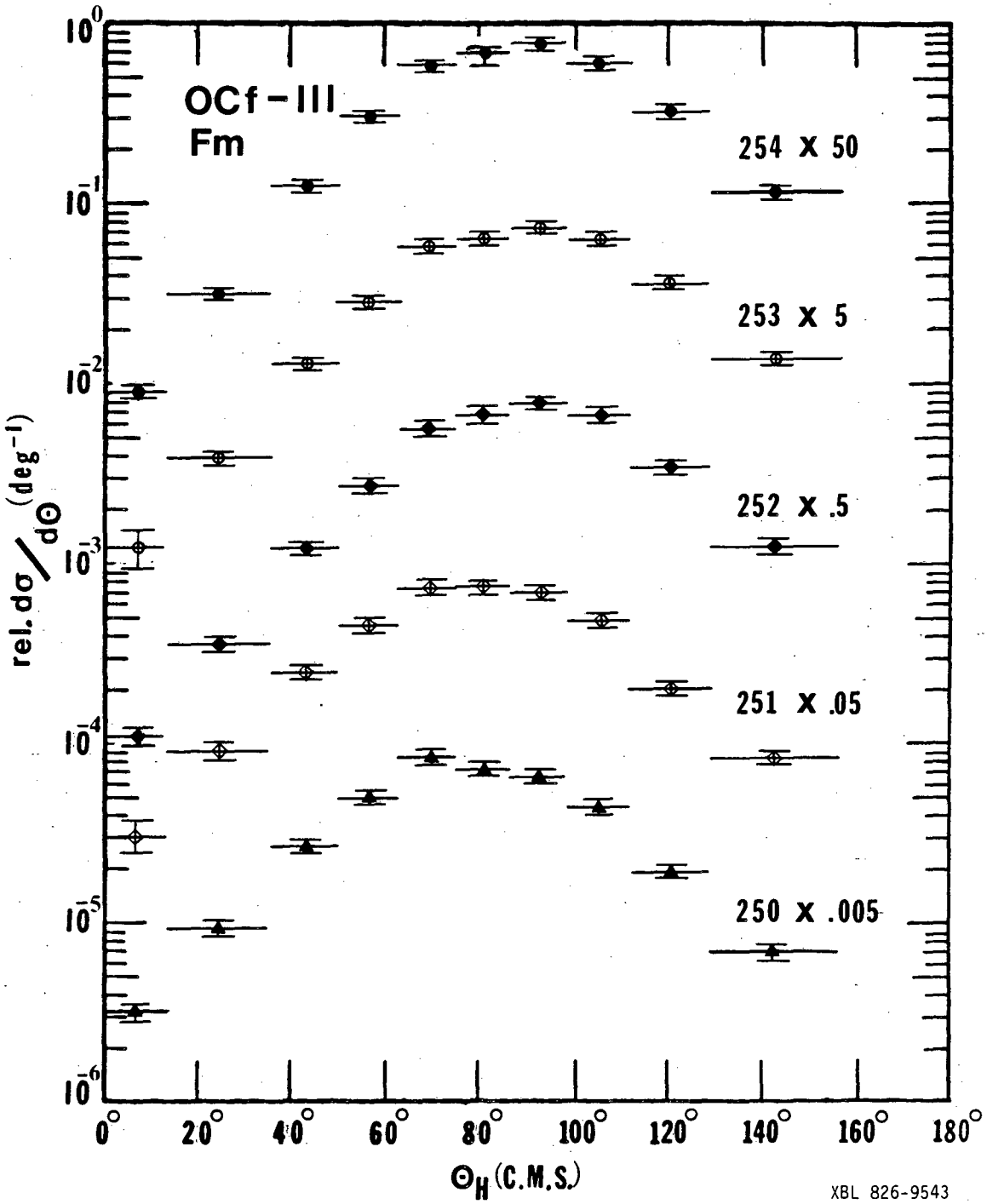
OCf-III
Fm
254 X 50
253 X 5
252 X .5
251 X .05
250 X .005
rel. dσ/dΘ (deg⁻¹)
Θ_H (C.M.S.)
XBL 826-9543

Fig. 32

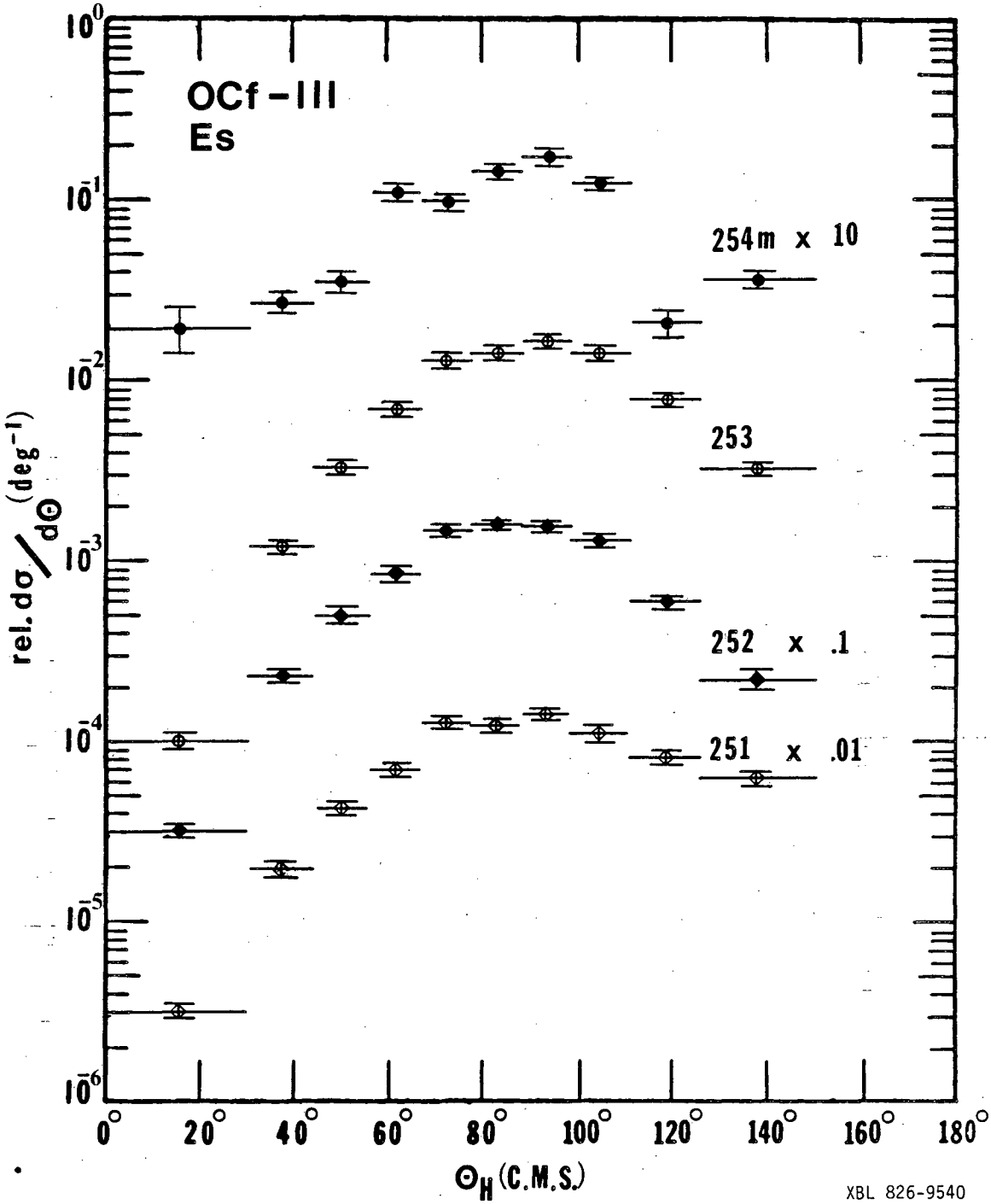
OCf-III
Es
254m x 10
253
252 x .1
251 x .01
rel. dσ/dΘ (deg⁻¹)
Θ_H (C.M.S.)
XBL 826-9540

Fig. 33

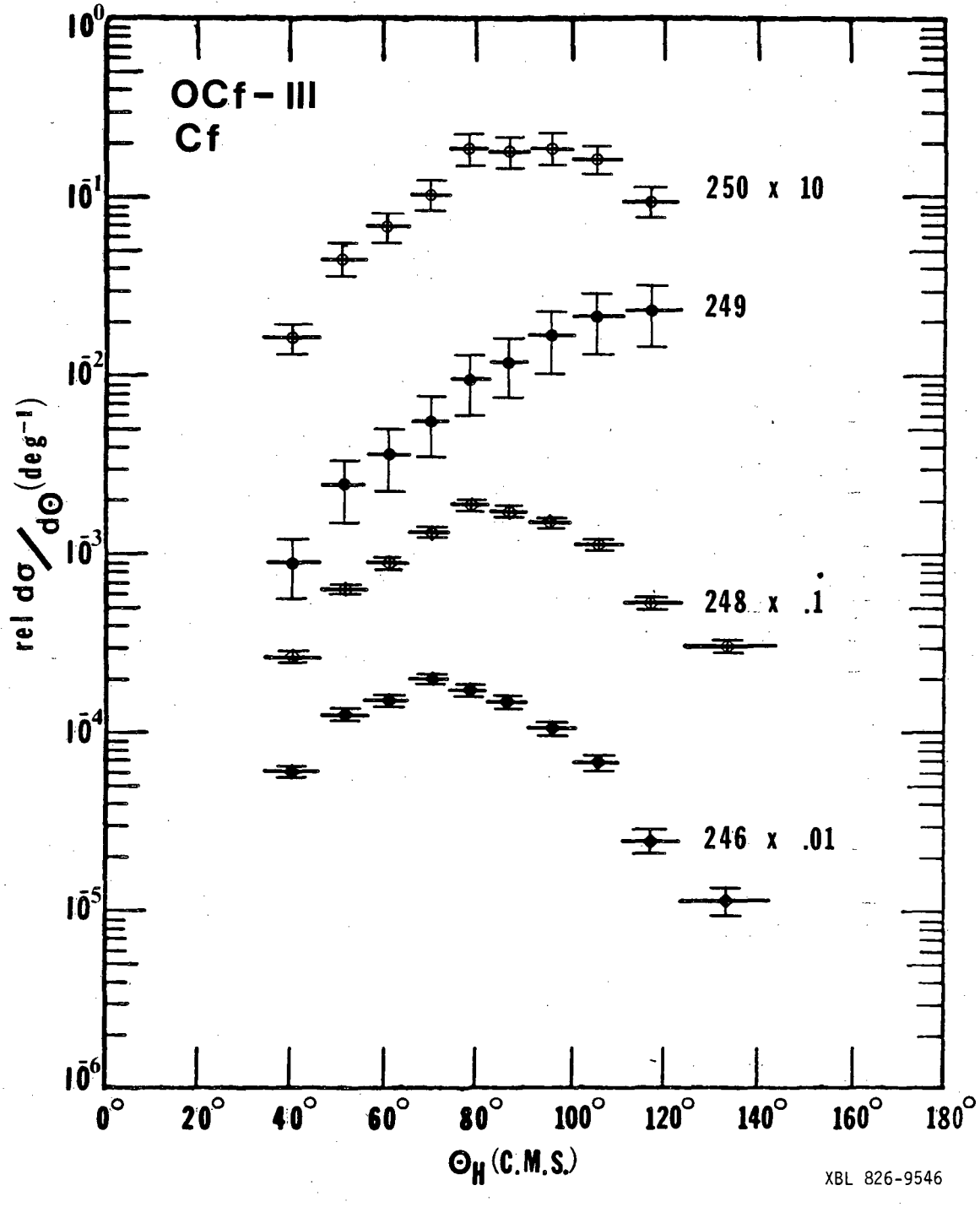
OCf - III
Cf
250 x 10
249
248 x .1
246 x .01
rel dσ/dΘ (deg⁻¹)
Θ_H (C.M.S.)
XBL 826-9546

Fig. 34

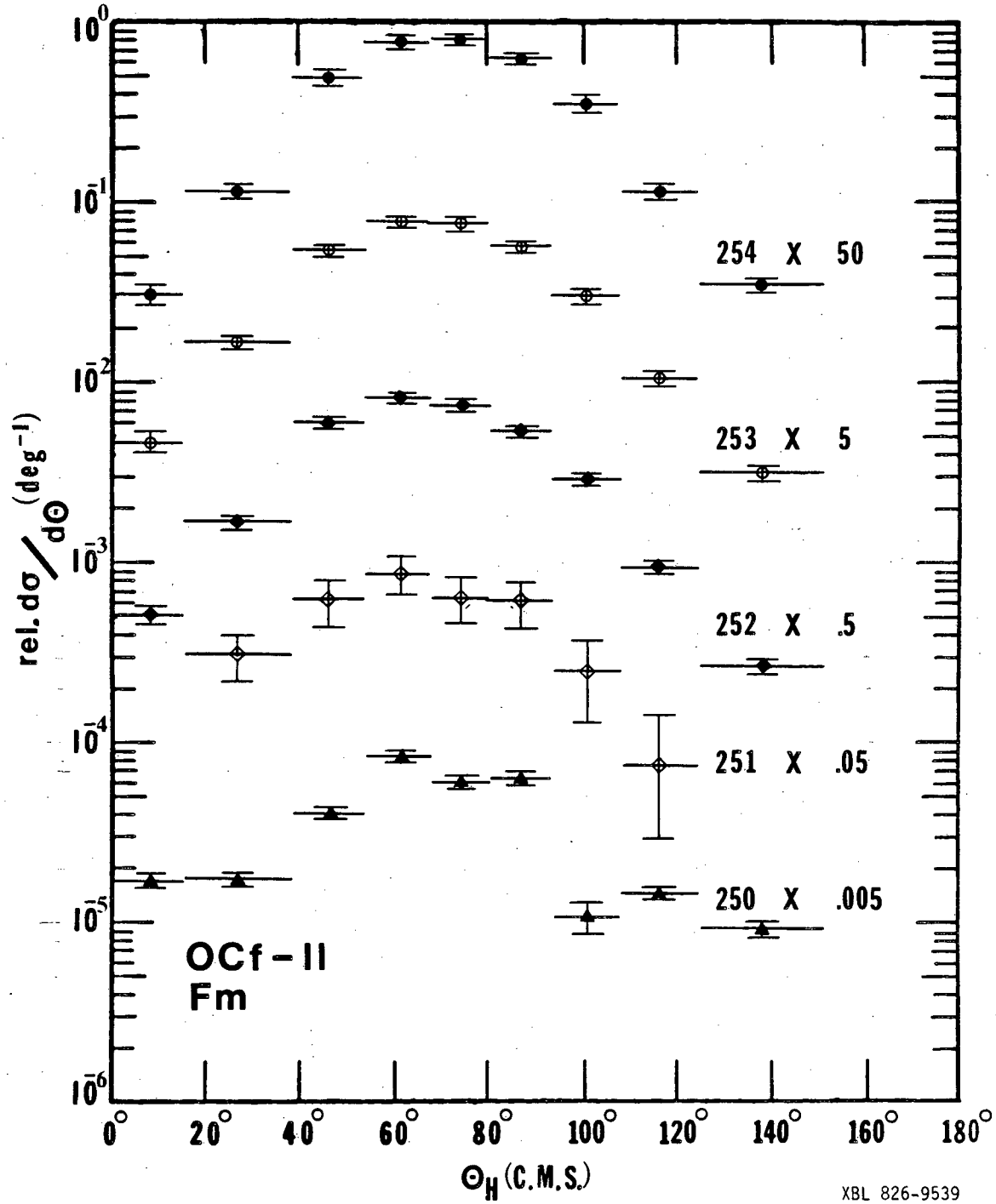
rel. dσ/dΘ (deg⁻¹)
10⁰
10⁻¹
10⁻²
10⁻³
10⁻⁴
10⁻⁵
10⁻⁶
254 X 50
253 X 5
252 X .5
251 X .05
250 X .005
OCf-II
Fm
0°
20°
40°
60°
80°
100°
120°
140°
160°
180°
Θ_H (C.M.S.)
XBL 826-9539

Fig. 35

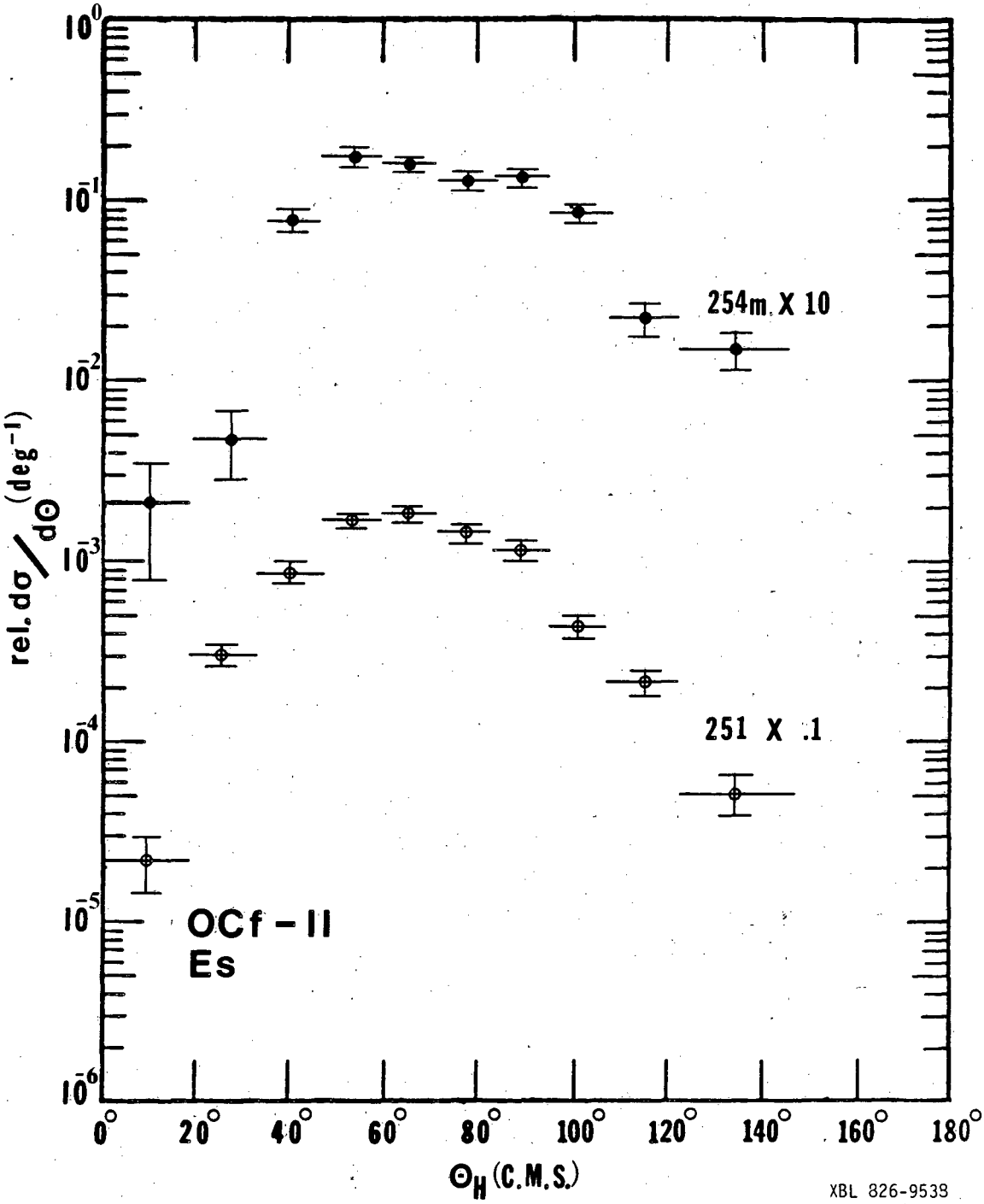
10^0
10^{-1}
10^{-2}
10^{-3}
10^{-4}
10^{-5}
10^{-6}
rel. $d\sigma / d\Theta$ (deg^{-1})
254m. X 10
251 X .1
OCf - II
Es
0°
20°
40°
60°
80°
100°
120°
140°
160°
180°
Θ_H (C.M.S.)
XBL 826-9538

Fig. 36

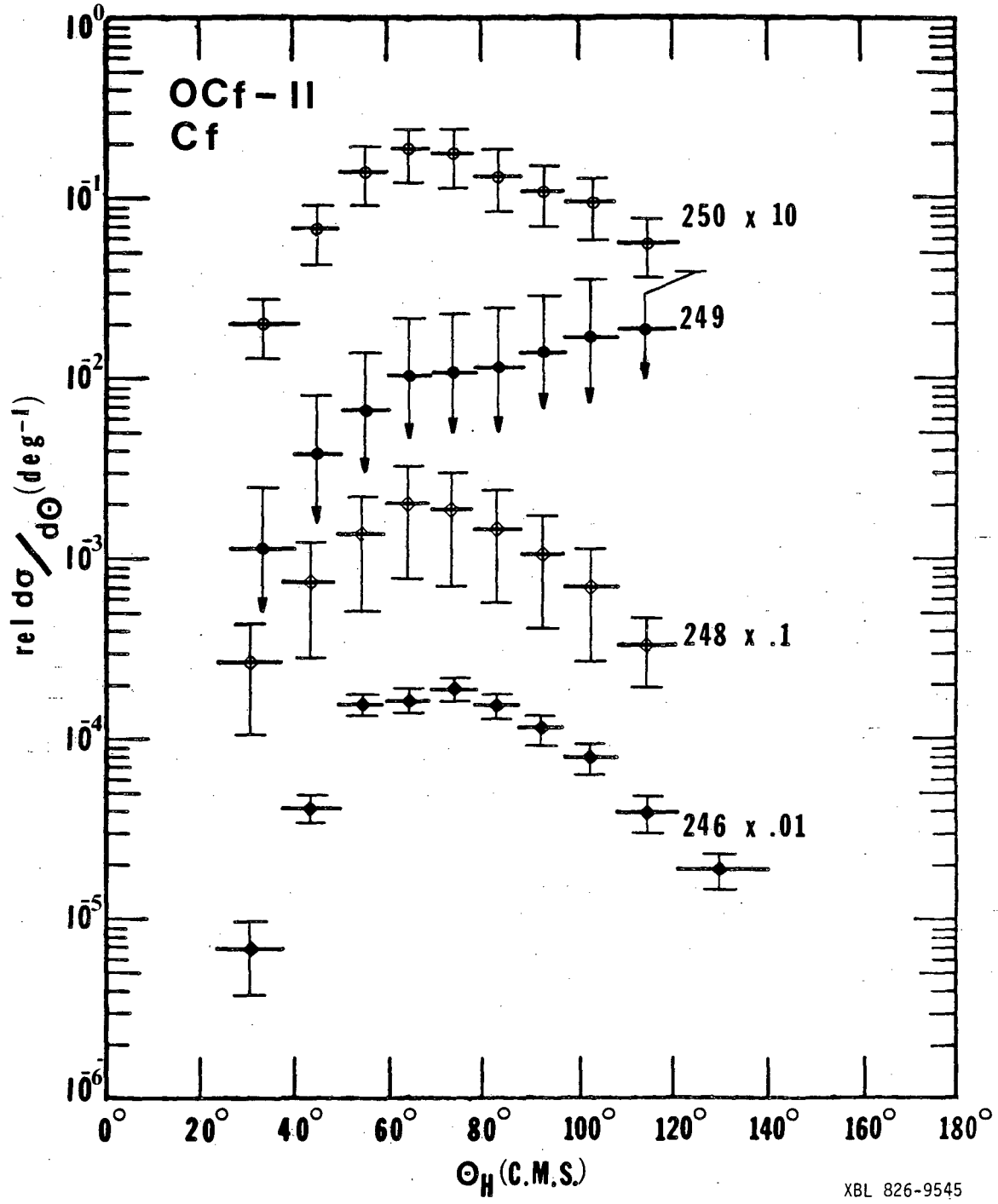
OCf - II
Cf
250 x 10
249
248 x .1
246 x .01
rel dσ/dΘ (deg⁻¹)
Θ_H (C.M.S.)
XBL 826-9545

Fig. 37

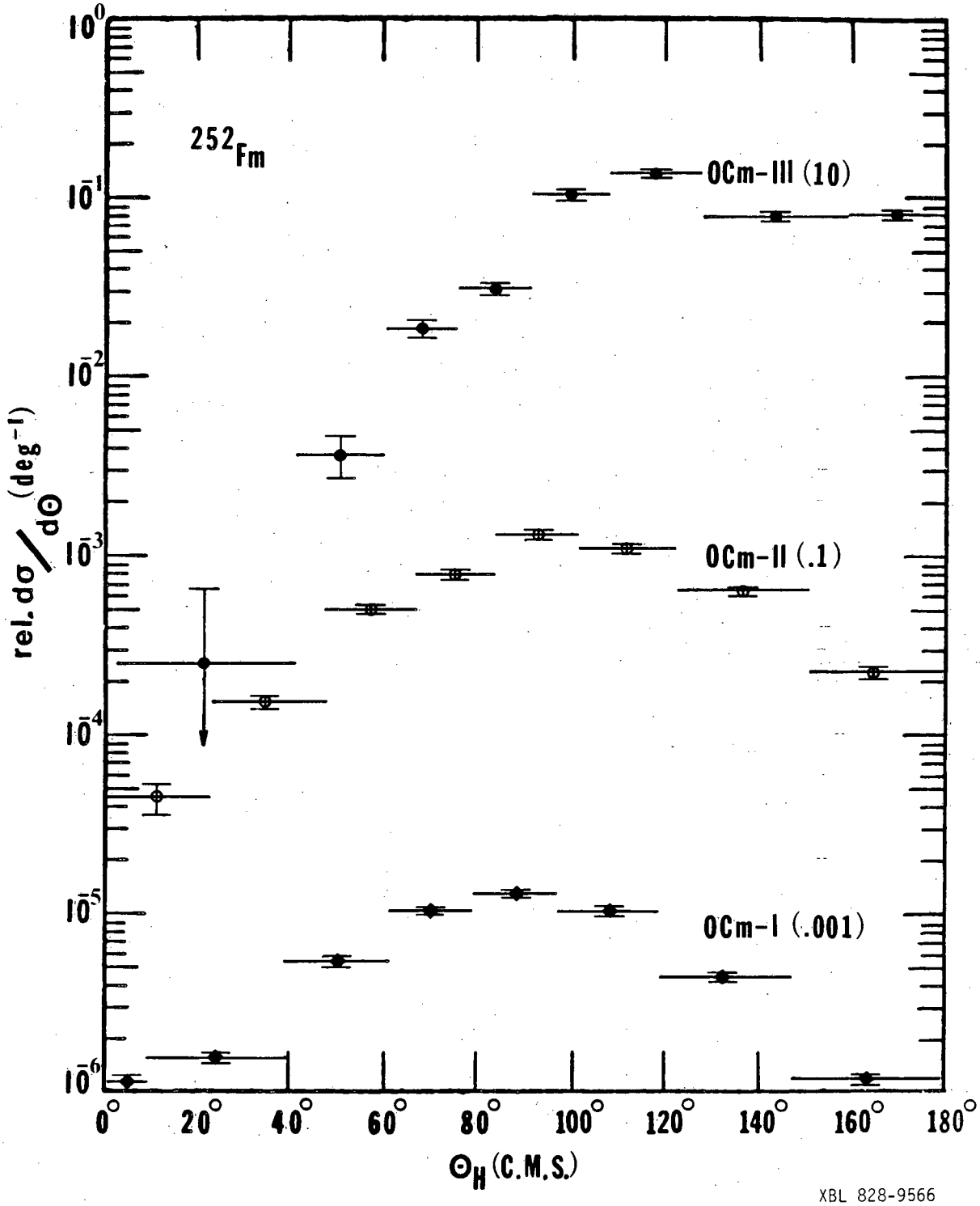
10^0
10^{-1}
10^{-2}
10^{-3}
10^{-4}
10^{-5}
10^{-6}
^{252}Fm
OCm-III (10)
OCm-II (.1)
OCm-I (.001)
rel. $d\sigma/d\Theta$ (deg^{-1})
0° 20° 40° 60° 80° 100° 120° 140° 160° 180°
Θ_H (C.M.S.)
XBL 828-9566

Fig. 38

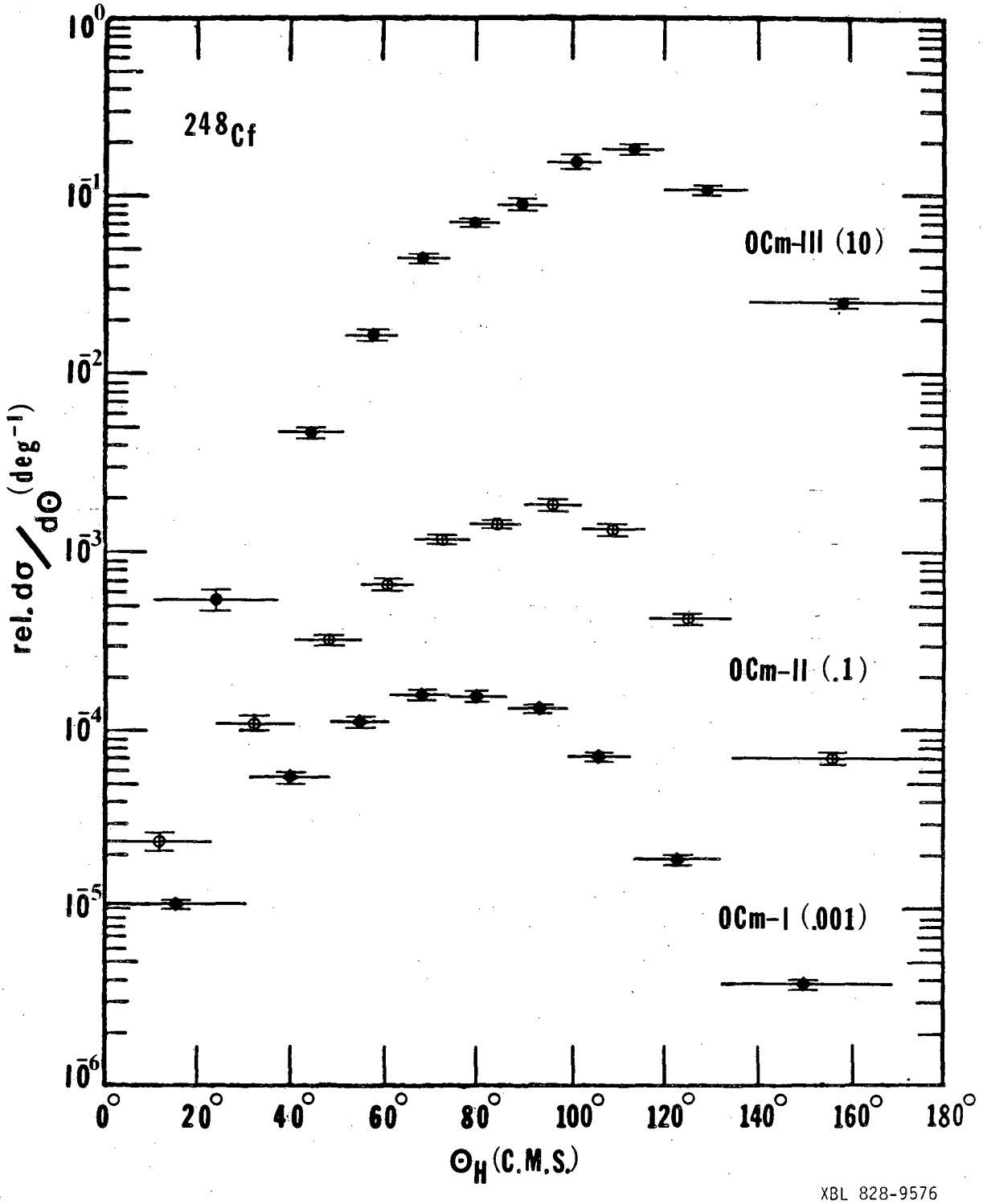
10^0
10^{-1}
10^{-2}
10^{-3}
10^{-4}
10^{-5}
10^{-6}
^{248}Cf
OCm-III (10)
OCm-II (.1)
OCm-I (.001)
rel. $d\sigma/d\Theta$ (deg^{-1})
0° 20° 40° 60° 80° 100° 120° 140° 160° 180°
Θ_H (C.M.S.)
XBL 828-9576

Fig. 39

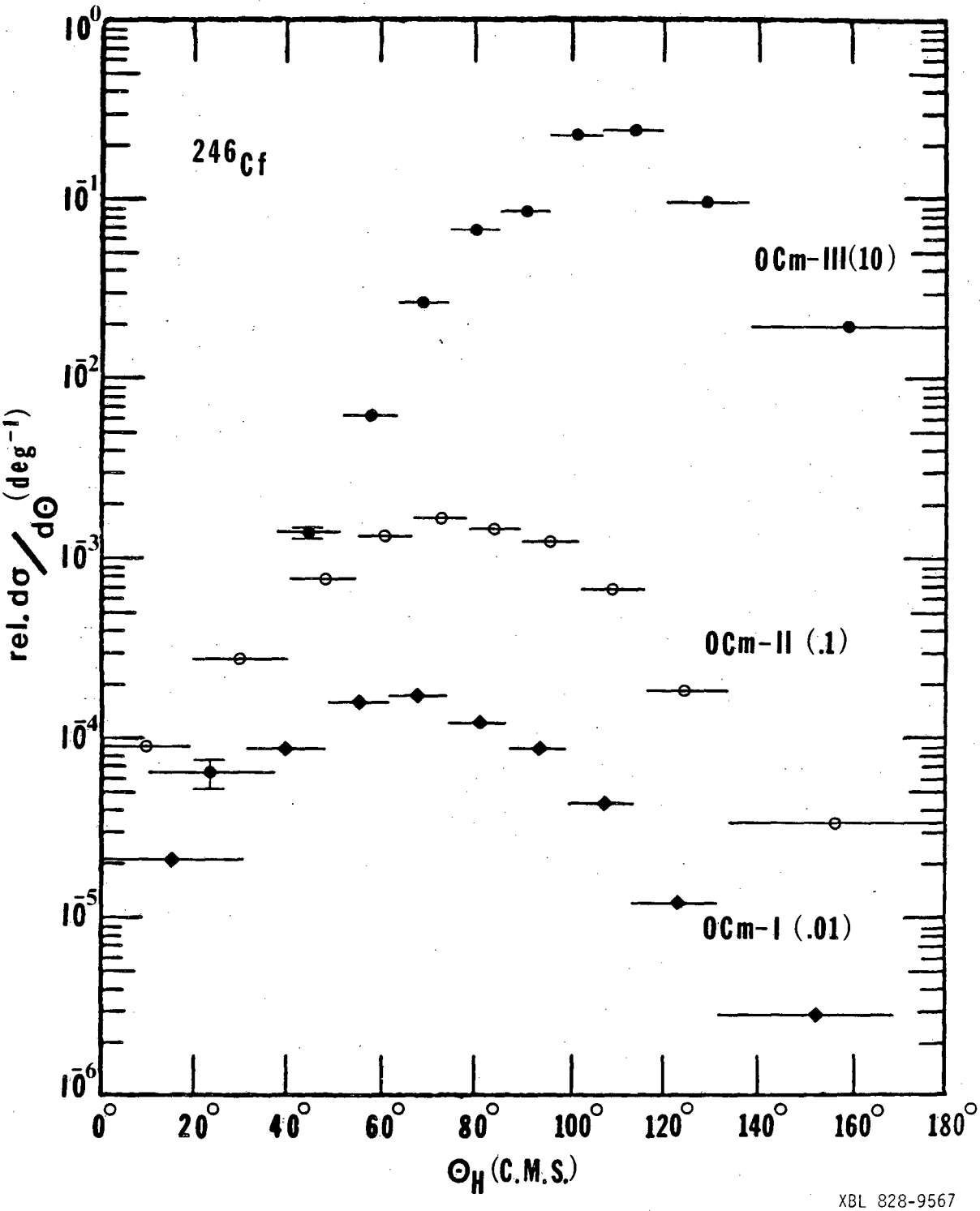
10^0
10^{-1}
10^{-2}
10^{-3}
10^{-4}
10^{-5}
10^{-6}
rel. $d\sigma/d\Theta$ (deg^{-1})
^{246}Cf
OCm-III(10)
OCm-II (.1)
OCm-I (.01)
0°
20°
40°
60°
80°
100°
120°
140°
160°
180°
Θ_H (C.M.S.)
XBL 828-9567

Fig. 40

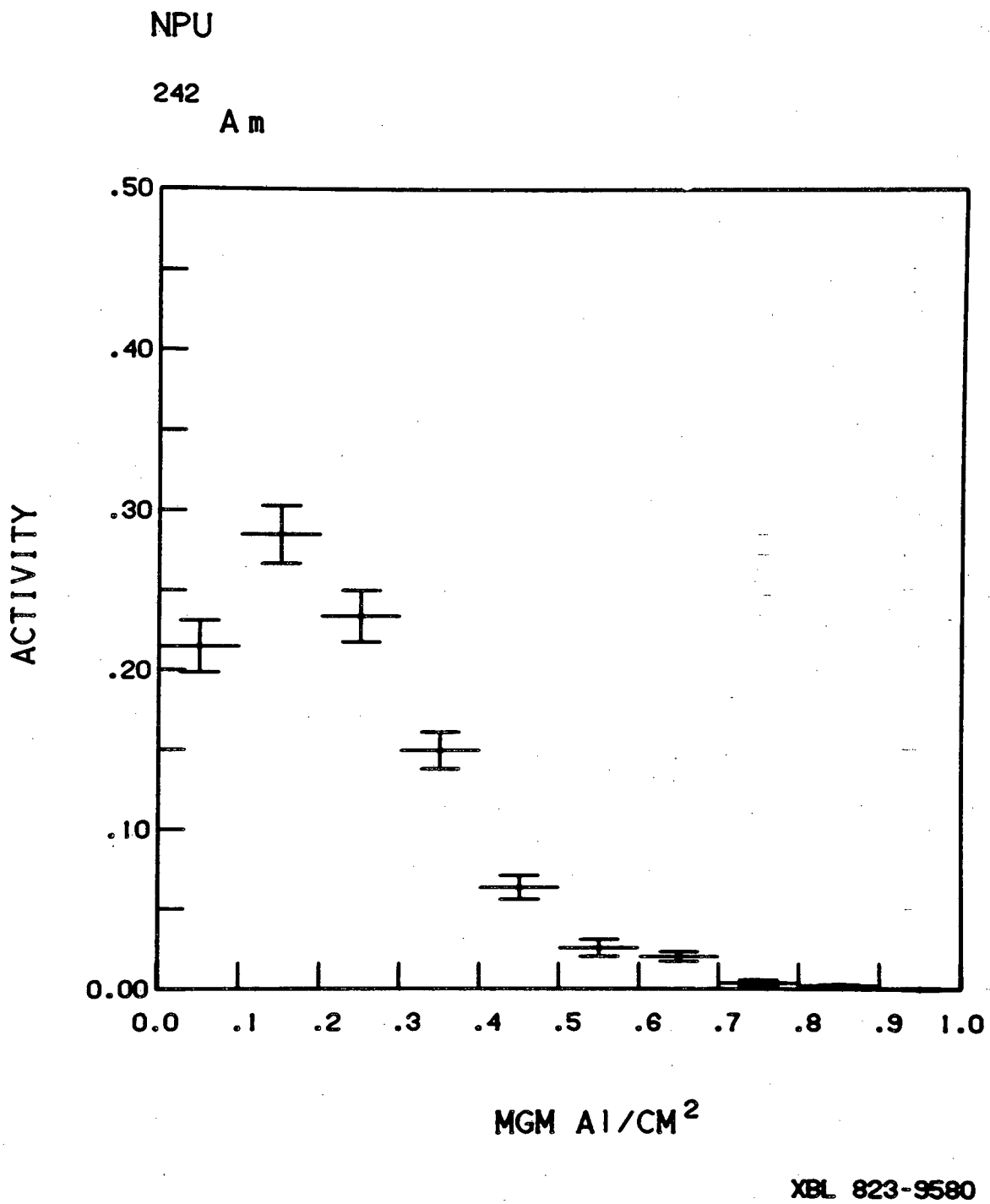
NPU
242
Am
.50
.40
.30
.20
.10
0.00
ACTIVITY
0.0
.1
.2
.3
.4
.5
.6
.7
.8
.9
1.0
MGM Al/CM2
XBL 823-9580

Fig. 41a

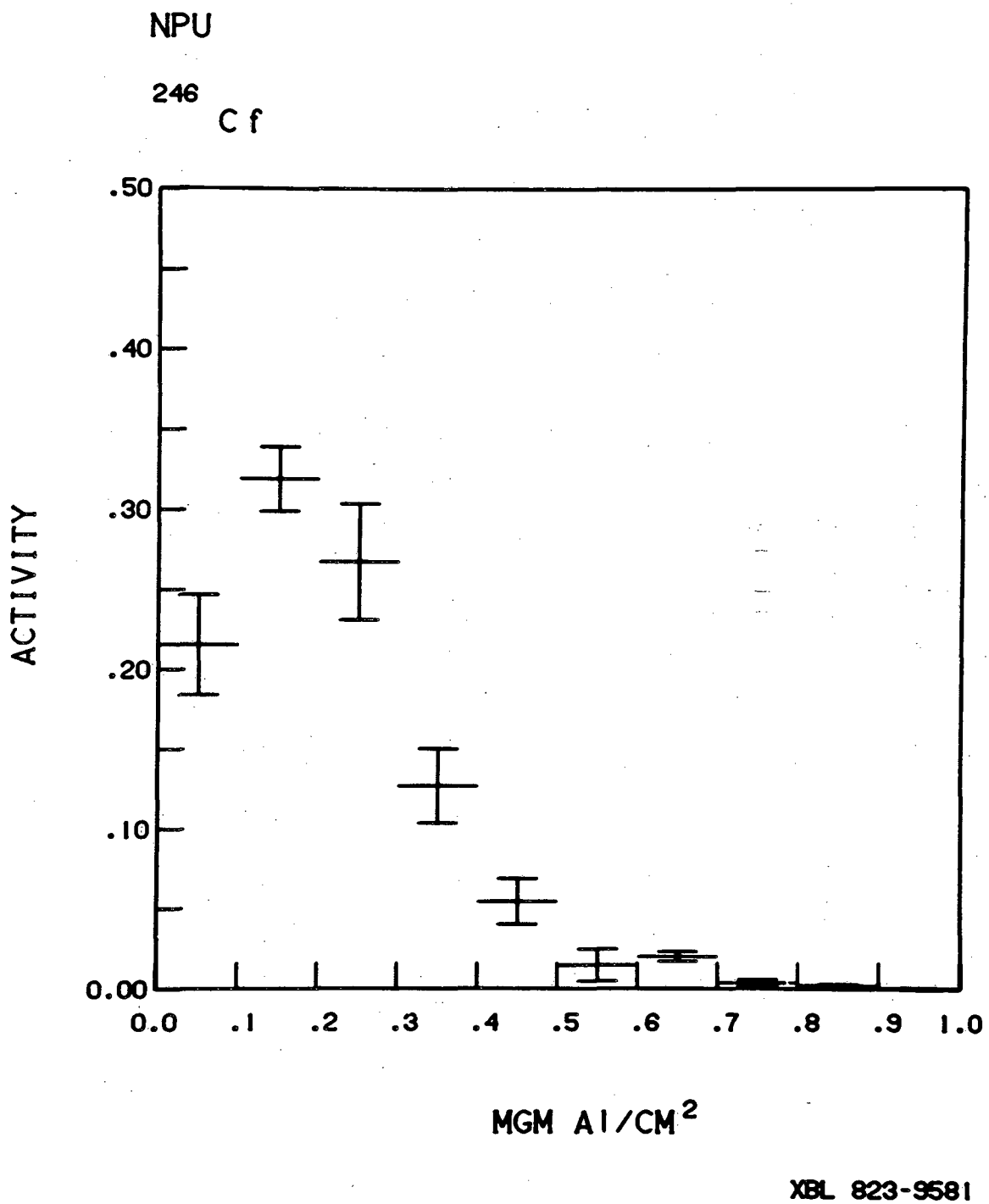
NPU
246 Cf
.50
.40
.30
.20
.10
0.00
ACTIVITY
0.0
.1
.2
.3
.4
.5
.6
.7
.8
.9
1.0
MGM Al/CM2
XBL 823-9581

Fig. 41b

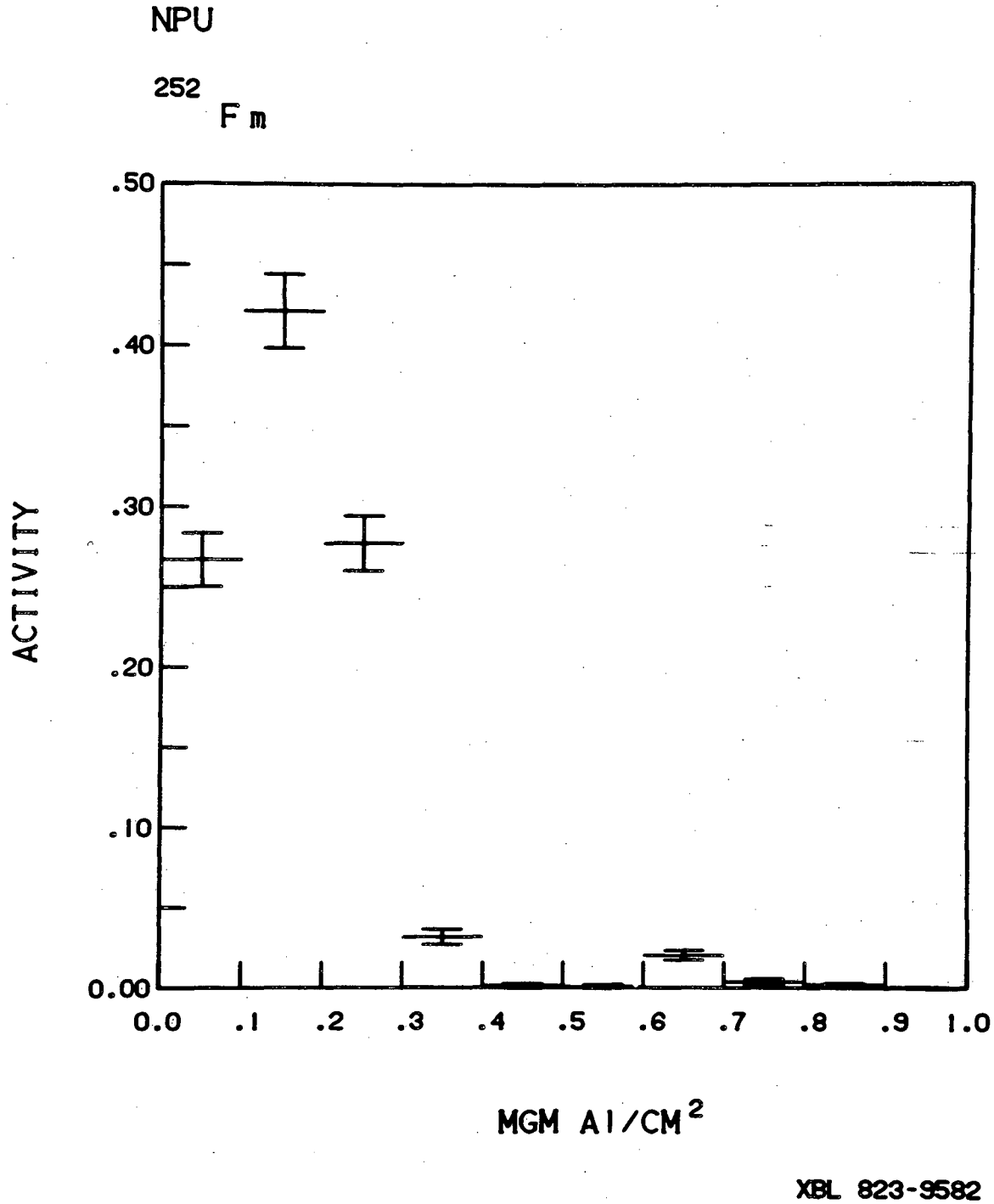
NPU
252
Fm
.50
.40
.30
.20
.10
0.00
ACTIVITY
0.0
.1
.2
.3
.4
.5
.6
.7
.8
.9
1.0
MGM Al/CM 2
XBL 823-9582

Fig. 42a

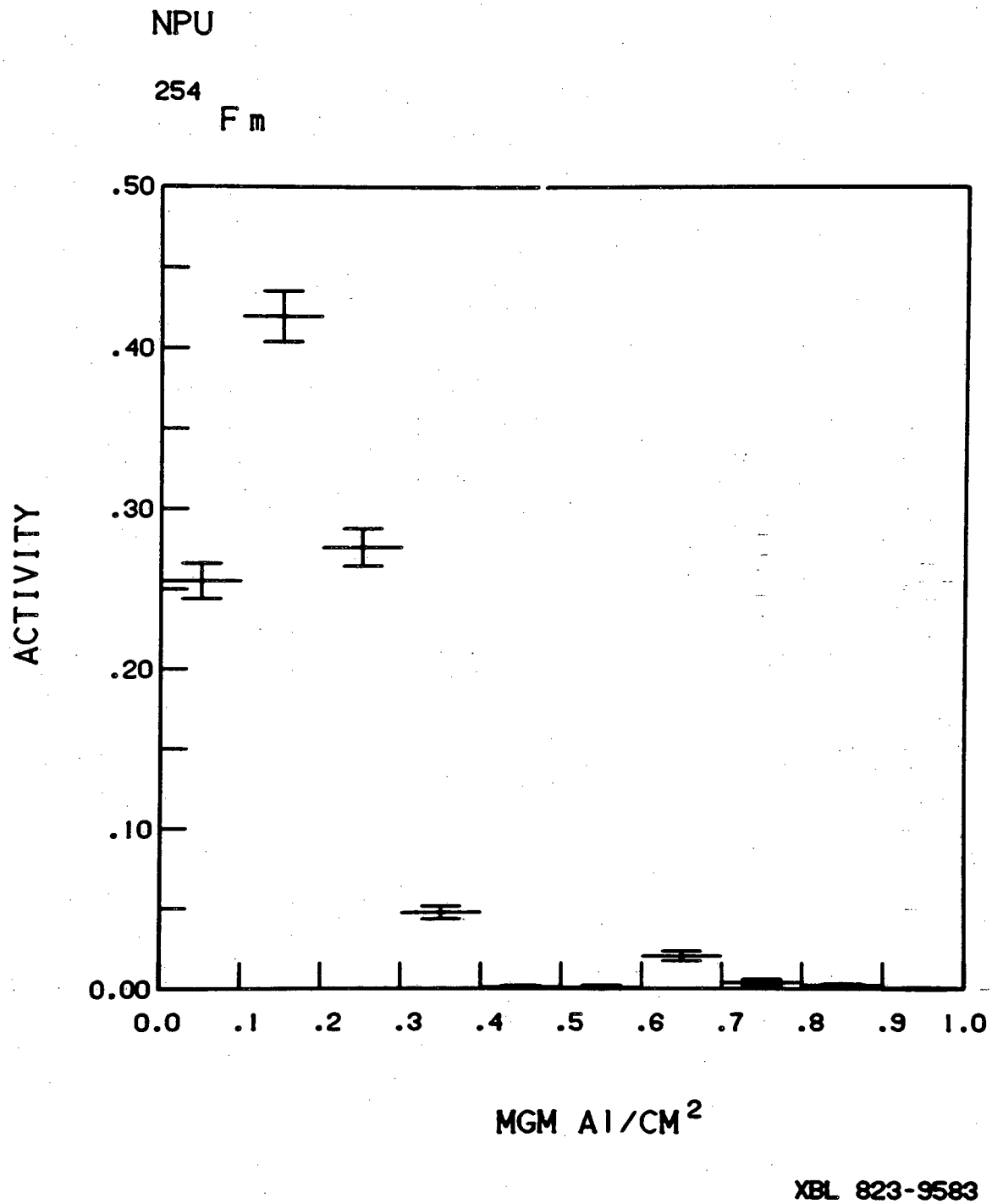
NPU
254
Fm
.50
.40
.30
.20
.10
0.00
ACTIVITY
0.0
.1
.2
.3
.4
.5
.6
.7
.8
.9
1.0
MGM Al/CM2
XBL 823-9583

Fig. 42b

TECHNICAL INFORMATION DEPARTMENT
LAWRENCE BERKELEY LABORATORY
UNIVERSITY OF CALIFORNIA
BERKELEY, CALIFORNIA 94720